ANALYTICAL MODELING OF SQUAT WALLS WITH SHEAR-CONTROLLED RESPONSES

by

Arif Emir Örendil

B.S., Civil Engineering, Istanbul Technical University, 2009

Submitted to the Institute for Graduate Studies in
Science and Engineering in partial fulfillment of
the requirements for the degree of
Master of Science

Graduate Program in Civil Engineering

Boğaziçi University

2014

ANALYTICAL MODELING OF SQUAT WALLS WITH SHEAR-CONTROLLED RESPONSES

APPROVED BY:

Associate Prof. Kutay Orakçal (Thesis Supervisor)	…….....
Prof. Alper İlki	…….....
Associate Prof. Hilmi Luş	…….....

DATE OF APPROVAL: 08.01.2014

To my family,

ACKNOWLEDGEMENTS

I would like to express my sincere appreciation to my thesis advisor Associate Professor Kutay Orakçal for his invaluable help in instructing, guiding and supporting me during the preparation of this thesis. I would also like to acknowledge his remarkable patience and his positive approach throughout the duration of this research.

I would like to express my heartfelt thanks to my fellow friend Muhammet Fethi Güllü for helping me during the implementation of the shear aggregate interlock model and the analysis of the model.

I would also like to thank to my Civil Engineer friends; Tamer İzzet Beyazoğlu and Hasan Yıldırım for all the contribution they have provided by the fruitful discussions.

Also, I would like deliver my gratefulness to my directors and colleagues at the office for their tolerance along this study.

Most of all, eternal thanks to who have contributed the most of my thesis work – my father, my mother, my brother, my whole family. I am indebted to them for their self-sacrifice, patience and love they have given me throughout my whole life.

ABSTRACT

ANALYTICAL MODELING OF SQUAT WALLS WITH SHEAR-CONTROLLED RESPONSES

In this study, a new finite element modeling methodology is implemented for simulating the in-plane hysteretic lateral load behavior of squat walls with aspect ratios not larger than 1.0, the response of which is governed by nonlinear shear deformations. The behavioral characteristics of the constitutive panel elements incorporated in the model formulation are based on a fixed crack angle modeling approach. Improvements are made on the constitutive panel model formulation, for better representation of the shear-aggregate-interlock effects in concrete and dowel action on reinforcing bars, constituting the shear stress transfer mechanisms across the cracks. Sensitivity studies are conducted on the influence of parameters of the constitutive shear-aggregate-interlock and dowel action relationships on the model results. The model is extensively calibrated for eleven squat wall specimens and model predictions are compared with experimentally-measured lateral load vs. displacement responses. Response comparisons reveal that the model provides reasonable predictions of the lateral stiffness, lateral load capacity, and ductility characteristics of the wall specimens investigated. As well, implementation of a new constitutive model formulation for dowel action is shown to provide improved response predictions for lateral load values at large displacements, shape of the unloading/reloading loops, and pinching characteristics of the response. The modeling approach adopted in this study is believed to be a feasible candidate for reliable prediction of shear controlled wall responses of squat walls under reversed-cyclic loading conditions.

ÖZET

BASKIN KESME DAVRANIŞI GÖSTEREN BODUR PERDE DUVARLARIN ANALİTİK MODELLENMESİ

Bu çalışma, önerilen yeni sonlu elemanlar metodolojisi ile doğrusal olmayan kesme deformasyonları etkisindeki, en-boy oranı 1.0 ve daha küçük olan bodur duvarların histeretik yanal yükleme koşulları altında modellenmesini içermektedir. Modelin formülasyonuna dahil edilen davranış karakteristikleri, sabit çatlama açısı modelline dayandırılmaktadır. Betondaki agrega kenetlenme etkisinin ve çatlakların iki kenarı arasında kesme gerilmesi aktarma mekanizmasını teşkil eden donatı üzerindeki dowel etkisinin daha iyi ifade edilmesi için panel modelinin formülasyonunda iyileştirmeler yapılmıştır. Agrega kenetlenme etkisinin ve dowel etkisinin, model sonuçları üzerindeki etkisinin anlaşılabilmesi amacıyla duyarlılık analizleri yapılmıştır. Deneysel çalışmada yer alan on bir adet bodur duvar numunesinin kalibrasyonu yapılmıştır. Bununla birlikte model öngörüleri, deneysel olarak ölçümlenen yanal yük-yer değiştirme tepkileri ile mukayese edilmiştir. Bu mukayeseler göstermiştir ki numunelerin yanal rijitliklerinin, yanal yük kapasitelerinin ve sünek davranışlarının tahmininde makul sonuçlar elde edilmiştir. Ayrıca, dowel etkisini içeren yeni model formülasyonunun yüksek yer değiştirme değerlerindeki yanal yük değerlerinin, yükleme-boşaltma döngülerinin ve dayanımdaki azalmanın modellenmesine olumlu katkı sağlandığı görülmüştür. Bu çalışmada önerilen modelin, tersinir tekrarlanır yükler altında kesme kontrollü kısa duvar davranışının öngörülmesi için uygun olduğuna kanaat getirilmiştir.

TABLE OF CONTENT

ACKNOWLEDGEMENTS iv
ABSTRACT v
ÖZET vi
LIST OF FIGURES ix
LIST OF TABLES xv
LIST OF SYMBOLS xvi
1. INTRODUCTION 1
1.1. General 1
1.2. Literature Review 2
1.3. Objectives and Scope 11
1.4. Thesis Outline 12
2. MODEL DESCRIPTION 13
2.1. Overview 13
2.2. Constitutive Panel Model 14
2.3. Constitutive Material Models 17
2.3.1. Constitutive Model for Reinforcement 17
2.3.2. Constitutive Model for Concrete 17
2.3.3. Compression Softening Effect on Concrete 19
2.3.4. Tension Stiffening Effects on Concrete and Reinforcing Steel 20
2.3.5. Biaxial Damage Effect on Concrete 20
2.3.6. Constitutive Modeling of the Shear Aggregate Interlock Effect in Concrete 21
2.3.7. Constitutive Modeling of Dowel Action on Reinforcing Bars 22
2.4. Finite Element Modeling Methodology 30
2.4.1. 4 Nodes, 8 Degree of Freedom Rectangular Element 30
2.4.2. Finite Element Model Stiffness Assembly 33

2.4.3. Internal Force Vector Assembly 34
2.4.4. Support Conditions and Constraints 36
2.4.5. Nonlinear Analysis Solution Strategy 37
3. EXPERIMENTAL CALIBRATION OF THE MODEL 40
3.1. Description of the Wall Specimens 40
3.2. Test Setup and Instrumentation 48
3.3. Loading Protocol and Observed Failure Modes 52
3.4. Calibration of the Model for the Wall Specimens 55
3.4.1. Calibration of Model Element Dimensions and Reinforcement Ratios 56
3.4.2. Calibration of Constitutive Material Parameters 56
3.4.2.1. Calibration of the Constitutive Model for Reinforcing Steel for Tension Stiffening Effects: 57
3.4.2.2. Calibration of the Constitutive Model for Concrete: 63
4. ANALYSIS RESULTS AND COMPARISONS WITH EXPERIMENTAL DATA 69
4.1. Model Sensitivity to the Constitutive Parameters of the Shear Transfer Mechanisms across Cracks 70
4.2. Comparison of Analysis and Test Results 76
4.2.1. Analysis Results Obtained Using a Linear Elastic Dowel Action Model 77
4.2.2. Analyses Results Obtained Using the Proposed Nonlinear Constitutive Model for Dowel Action 82
5. SUMMARY AND CONCLUSIONS 90
5.1. Overview 90
5.2. Conclusions 90
5.3. Recommendations for Future Studies 91
REFERENCES 93

LIST OF FIGURES

Figure 1.1. Shear spring with shear limit curve (Elwood, 2002). 6

Figure 1.2. MVLEM (Orakcal *et al.*, 2004). 7

Figure 2.1. Uncracked behavior of concrete in the Fixed Strut Angle Model (Orakcal *et al.*, 2012). 14

Figure 2.2. Behavior of concrete after formation of first crack in the Fixed Strut Angle Model (Orakcal *et al.*, 2012). 15

Figure 2.3. Behavior of concrete after formation of second crack in the Fixed Strut Angle Model (Orakcal *et al.*, 2012). 16

Figure 2.4. Hysteretic constitutive model for reinforcing steel (Menegotto and Pinto, 1973). 17

Figure 2.5. Hysteretic constitutive model for concrete (Chang and Mander, 1994). 18

Figure 2.6. Compression softening effects implemented in the panel model (Ulugtekin, 2010). 19

Figure 2.7. Shear-aggregate interlock model (Orakcal *et al.*, 2012). 22

Figure 2.8. The constitutive shear stress vs. strain model adopted to represent dowel action on reinforcing bars. 23

Figure 2.9. Shear stress-strain relationship in the positive strain region. 28

Figure 2.10. Shear stress-strain relationship in the negative strain region. 29

Figure 2.11. Local nodes and DOFs in a rectangular model element. 31

Figure 2.12. Normalized coordinates of a rectangular model element. 31

Figure 2.13. Numbering technique used for the FEM of a rectangular wall. 33

Figure 2.14. Global and local DOFs for a wall model. 34

Figure 2.15. Numbering of internal force terms for a model element (Gullu, 2013). 35

Figure 2.16. Conversion of DOFs after the assignment of body constraint (Gullu, 2013). 36

Figure 2.17. Representation of the nonlinear analysis solution strategy for a single degree of freedom system (Clarke and Hancock, 1990). 38

Figure 2.18. Iterative strategy and residual displacements (Clarke and Hancock, 1990)... 39

Figure 3.1. Naming of the wall specimens. 40

Figure 3.2. Hook type. 41

Figure 3.3. Geometry and reinforcement of specimen T1–S1 (Terzioglu, 2011). 43

Figure 3.4. Cross section of a specimen: Definition of boundary and web regions. 43

Figure 3.5. Stress-Strain curves of steel, for specimen set 1 (Terzioglu, 2011). 45

Figure 3.6. Stress-Strain curves of steel, for specimen set 2 and set 3 (Terzioglu, 2011). 45

Figure 3.7. Stress-Strain curves of steel, for specimen set 2 and set 3 (Terzioglu, 2011). 46

Figure 3.8. Formwork and reinforcement of a wall specimen (Terzioglu, 2011).....48

Figure 3.9. Test setup (Terzioglu, 2011). 49

Figure 3.10. Strain gauge positions (Terzioglu, 2011). 50

Figure 3.11. Vertical and horizontal LVDTs (Terzioglu, 2011).....51

Figure 3.12. LVDT locations – 0.5 Aspect ratio walls (Terzioglu, 2011).....52

Figure 3.13. LVDT spring – loaded and mounting assembly (Terzioglu, 2011). 52

Figure 3.14. Stress-strain behavior of bare rebar and rebar embedded in concrete.....57

Figure 3.15. Stress-Strain relationship by Belarbi and Hsu (1994) for bar in concrete.....58

Figure 3.16. Compression and tension envelope curves of the Model by Chang and Mander. 63

Figure 3.17. Stress-strain diagrams for concrete in compression for specimen SW-T2-S1-1. 65

Figure 3.18. Stress-strain relationship by Belarbi and Hsu (1994) for concrete in tension. 67

Figure 3.19. Stress-strain diagrams for concrete in tension for specimen SW-T2-S1-1.....68

Figure 4.1. Test results obtained for specimen SW-T3-S1-5. 70

Figure 4.2. Results of the first three sensitivity analyses.....72

Figure 4.3. The influence of the exponential degradation coefficient on the constitutive shear stress vs. strain model for dowel action on reinforcement. 73

Figure 4.4. Sensitivity of the response to the exponential degradation coefficient for reinforcing steel. 74

Figure 4.5. Sensitivity of the response to the shear stress capacity coefficient and the exponential degradation coefficient for reinforcing steel. 75

Figure 4.6. Analysis results obtained for optimal values for the shear stress transfer coefficients. 76

Figure 4.7. Comparison of analysis result with linear elastic dowel action vs. test result for specimen SW-T2-S1-1. 77

Figure 4.8. Comparison of analysis result with linear elastic dowel action vs. test result for specimen SW-T1-S1-2. 78

Figure 4.9. Comparison of analysis result with linear elastic dowel action vs. test result for specimen SW-T2-S2-3. 78

Figure 4.10. Comparison of analysis result with linear elastic dowel action vs. test result for specimen SW-T2-S3-4. 79

Figure 4.11. Comparison of analysis result with linear elastic dowel action vs. test result for specimen SW-T3-S1-5. 79

Figure 4.12. Comparison of analysis result with linear elastic dowel action vs. test result for specimen SW-T4-S1-6. 80

Figure 4.13. Comparison of analysis result with linear elastic dowel action vs. test result for specimen SW-T5-S1-7. 80

Figure 4.14. Comparison of analysis result with linear elastic dowel action vs. test result for specimen SW-T6-S1-8. 81

Figure 4.15. Comparison of analysis result with linear elastic dowel action vs. test result for specimen SW-T1-S2-9. 81

Figure 4.16. Comparison of analysis result with linear elastic dowel action vs. test result for specimen SW-T1-N5-S1-10. 82

Figure 4.17. Comparison of analysis result with linear elastic dowel action vs. test result for specimen SW-T1-N10-S1-11. 82

Figure 4.18. Comparison of analysis result with nonlinear dowel action vs. test result for specimen SW-T2-S1-1. 83

Figure 4.19. Comparison of analysis result with nonlinear dowel action vs. test result for specimen SW-T1-S1-2. 84

Figure 4.20. Comparison of analysis result with nonlinear dowel action vs. test result for specimen SW-T2-S2-3. 84

Figure 4.21. Comparison of analysis result with nonlinear dowel action vs. test result for specimen SW-T2-S3-4. 85

Figure 4.22. Comparison of analysis result with nonlinear dowel action vs. test result for specimen SW-T3-S1-5. 86

Figure 4.23. Comparison of analysis result with nonlinear dowel action vs. test result for specimen SW-T4-S1-6. 87

Figure 4.24. Comparison of analysis result with nonlinear dowel action vs. test result for specimen SW-T5-S1-7. 87

Figure 4.25. Comparison of analysis result with nonlinear dowel action vs. test result for specimen SW-T6-S1-8. 88

Figure 4.26. Comparison of analysis result with nonlinear dowel action vs. test result for specimen SW-T1-S2-9. 88

Figure 4.27. Comparison of analysis result with nonlinear dowel action vs. test result for specimen SW-T1-N5-S1-10. 89

Figure 4.28. Comparison of analysis result with nonlinear dowel action vs. test result for specimen SW-T1-N10-S1-11. 89

LIST OF TABLES

Table 3.1. Reinforcement ratios. 42

Table 3.2. Dimensions of the wall specimens. 44

Table 3.3. Material properties of reinforcing steel. 46

Table 3.4. Concrete compressive strength. 47

Table 3.5. Observed failure modes of the specimens. 55

Table 3.6. Model element number and element size used for modeling of the specimens. 56

Table 3.7. Calibrated values of the constitutive parameters of reinforcing steel bars for specimens SW-T2-S1-1, SW-T1-S1-2, and SW-T2-S2-3. 60

Table 3.8. Calibrated values of the constitutive parameters of reinforcing steel bars for specimens SW-T2-S3-4, SW-T3-S1-5, SW-T4-S1-6, and SW-T5-S1-7. 61

Table 3.9. Calibrated values of the constitutive parameters of reinforcing steel bars for specimens SW-T6-S1-8, SW-T1-S2-9, SW-T1-N5-S1-10, and SW-T1-N10-S1-11 62

Table 3.10. Calibrated values of the constitutive parameters for concrete in compression. 65

Table 3.11. Calibrated values of the constitutive parameters for concrete in tension. 68

Table 4.1. Varying parameters associated with shear transfer across cracks. 71

LIST OF SYMBOLS

A_g	Gross concrete cross-section area
B	Tension stiffening parameter for reinforcing steel
b	Strain hardening ratio for compression
b'	Strain hardening ratio for tension
d_i	Local nodal displacement
D_i	Global nodal displacement
{D}	Global displacement vector
E_c	Elastic modulus for concrete
E_p	Plastic (strain hardening) modulus for bare steel bars
E_p^*	Plastic (strain hardening) modulus for steel bars embedded in concrete
E_s	Elastic modulus for steel
[E]	Elasticity matrix
f'_{cr}	Compressive strength of concrete
f_{cr}	Tensile cracking stress of concrete
f_y	Yield stress of web reinforcement
f_{ult}	Ultimate stress of web reinforcement
{f}	Local internal force vector of one mesh
{F}	Global internal force vector
$\{F_{unb}\}$	Unbalanced force vector
[G]	Strain matrix

$[G]^T$	Transpose of strain matrix
h_w	Height of the wall
[k]	Local stiffness matrix of one mesh
[K]	Global stiffness matrix
l_w	Length of the wall
h	Height of mesh
m	Mesh number in horizontal direction
n	Mesh number in vertical direction
r	Shape parameter of the compression envelop
t	thickness of the wall
[T]	Transformation matrix for body constraint
$[T]^T$	Transpose of transformation matrix for body constraint
x_{crn}	Critical strain parameter of concrete in compression by Saatcioglu and Razvi Model
x_{crp}	Critical strain parameter of concrete in tension by Belarbi and Hsu Model
w	Width of mesh
ε_y	Yield strain of web reinforcement
ε_{ult}	Ultimate strain of web reinforcement
ε_c'	Strain of concrete at peak stress
ε_t	Critical strain in shear aggregate interlock model
ε_{un}	Unloading strain in shear aggregate interlock model

ε_p	Plastic strain in shear aggregate interlock model
ε_{re}	Reloading strain in shear aggregate interlock model
ε_{unre}	Unloading strain at reloading stage in shear aggregate interlock model
σ_n^*	Normal stress at tension stiffening
σ_t	Critical stress in shear aggregate interlock model
σ_y	Yield stress of reinforcing steel
ρ_b	Boundary reinforcement ratio
ρ_l	Longitudinal reinforcement ratio
ρ_t	Transverse reinforcement ratio
α	Angle between shear friction reinforcement and shear plane
ξ	Normalized local coordinates of a mesh in x direction
η	Normalized local coordinates of a mesh in y direction
$\Delta\lambda$	Initial load increment
$\Delta\delta_n$	Initial displacement increment
$\Delta\delta$	Displacement increment
$\Delta\delta_R$	Residual displacement increment

1. INTRODUCTION

1.1. General

Reinforced concrete (RC) structural walls are used to improve the seismic performance of reinforced concrete structural systems. Presence of structural walls has significant contribution in resisting lateral effects imposed on building structures, especially due to earthquake actions and wind loads. Properly designed and detailed structural walls possess the necessary strength, stiffness, deformation capacity to resist lateral actions. Typically, for a well-designed and detailed slender wall, shear failure does not occur and the wall experiences a ductile flexural response under seismic excitation. Since the existence of structural walls improves the performance of buildings, it is important to understand and characterize the hysteretic behavior of walls under seismic actions. Therefore, various analytical and experimental studies were conducted to investigate the lateral load behavior of RC structural walls.

There are numerous modeling methods and computer programs for analyzing structural system under load effects and seismic actions. However, most of commonly-applied analysis methods do not represent the nonlinear hysteretic behavior of RC structural walls. Moreover, representation of the hysteretic behavior becomes more complicated when the structural wall is relatively squat (low-rise) wall (when aspect ratio is smaller than approximately 1.5 or 1.0), since flexural yielding before shear failure is not a design requirement for squat walls or wall segments in a perforated system wall, and the lateral load behavior of such walls are typically governed by nonlinear shear deformations, or coupling of nonlinear flexural and shear responses. Although various experimental and analytical studies were also conducted on experimental response evaluation and modeling of the response of squat walls, there is still a need for a robust modeling approach to simulate the nonlinear hysteretic behavior of such walls.

In this study, a new finite element modeling methodology was implemented for simulating the in-plane hysteretic lateral load behavior of squat walls, with aspect rations

smaller than 1.0, the response of which are governed by nonlinear shear deformations. The modeling approach considers the influence of nonlinear flexural and shear responses on wall response, as well as their interaction throughout the cyclic loading history. The behavior of the constitutive panel (membrane) elements in the finite element model are described by a previously-developed constitutive panel model (the so-called Fixed-Strut-Angle Model developed by Ulugtekin, 2010), although improvements were made on the shear-aggregate-interlock and dowel mechanisms for transfer of shear stresses across cracks. Sensitivity studies were conducted on the influence of the parameters associated with the constitutive shear-aggregate-interlock and dowel relationships on the model results. The model was calibrated for the squat wall specimens tested by Terzioglu (2011), and model predictions were compared with the experimentally-observed hysteretic lateral load vs. displacement responses.

1.2. Literature Review

There are various experimental and analytical studies in the literature that focus on the lateral load behavior of slender structural walls, the response of which is controlled by nonlinear flexural deformations. On the other hand, studies that concentrate on the nonlinear shear behavior of walls and coupling of shear and flexural responses in walls, are relatively limited.

There are two main analytical modeling approaches for predicting the lateral load vs. deformation response of reinforced concrete walls, macro-modeling approaches and micro-modeling approaches. Macro-models offer the advantage of capturing important response features with reduced computational effort; however, use of these models is typically limited to pre-defined behavior and failure modes (Vulcano *et al.*, 1988). Micro-models, such as detailed nonlinear, three-dimensional, finite element models are usually more versatile; however, complications arise in formulation and especially calibration of such models, interpretation of results, and computational stability. Micro-models also require substantial computational effort, which may be a disadvantage in modeling of complex wall systems.

The Multiple-Vertical-Line-Element (MVLE) model (Vulcano and Bertero, 1987) is one of the earliest macro-models, which was shown to provide efficient and reasonably accurate hysteretic response predictions for slender walls, the responses of which are controlled by nonlinear flexural deformations. Although the model formulation considers shear deformations, shear and flexural components of the response are uncoupled. The shear response of a wall is modeled independently from flexural deformations, using a predefined shear force vs. deformation relationship, the parameters of which need to be calibrated in an ad-hoc manner. More recent studies have incorporated interaction between flexure and shear responses. The MVLE model was modified by providing an alternative approach to incorporate shear behavior by Colotti (1993). The interaction between axial and shear responses was attained by supplying a constitutive membrane (panel) model over a one-story model element. Uniaxial material models were used for modeling the flexural and axial components of the response. Although the relative contributions of shear and flexural deformations computed using the model showed some discrepancies with experimental data, the results obtained by using this model were more accurate compared with prior macro-models. However, although axial and shear responses are coupled in the model formulation, the model is incapable of incorporating interaction between shear and flexural responses. Therefore, the shear behavior is invariant with, for example, wall height, which has been shown to be unrealistic (Massone and Wallace, 2004).

Various constitutive modeling approaches were proposed for simulating the coupling of axial and shear responses in reinforced concrete panel elements (membranes subjected to uniform in-plane stresses). In 1996, Pang and Hsu proposed a new theory called the Fixed Angle Softened Truss Model (FA-STM) (1996). In this theory, the direction of the cracks was assumed to coincide with the fixed angle following the principal directions of the applied stresses. Sliding shear stresses along cracks surfaces, which develop as a result of this assumption, were calculated using a newly-developed shear modulus.

After the development of FA-STM, researchers at the University of Houston commenced a new experimental program to develop a set of reversed cyclic material models. In the scope of this experimental program, 12 cyclic panel tests were conducted, where three specimens were oriented at 90° angle relative to the testing equipment (the angle represents the orientation of reinforcing bars relative to panel edges), five specimens

oriented at 45°, three at 68.2° and one at 79.8°. Proportionally-applied reversed cyclic load tests on three 45° panels were used as reference test specimens during the calibration of the model proposed in this study. As a result of this research program, a new model, which was a cyclic extension of the FA-STM, was proposed, together with new cyclic constitutive material relationships both for steel and concrete. (Mansour *et al.* 2002)

Results of the same experimental program were also used to calibrate the Cyclic Softened Membrane Model, which was an extension of the original SMM with cyclic constitutive material relationships implemented for both steel and concrete. However, in addition to the cyclic material models, a damage coefficient, which defines the effect of the compressive strain history in the perpendicular direction to a compressive strut, was also implemented into the model. This damage coefficient was similar to that derived by Stevens with minor differences in formulation (Mansour and Hsu 2005, Hsu and Mansour 2002).

In 2000, Vecchio proposed a new theory called the Disturbed Stress Field Model (DSFM). In this theory, it was assumed that principal stress and strain directions deviate from each other and the crack directions coincide with the principal stress direction. On the other hand, principal stress directions rotate relative to (deviate from) principal strain directions with a fixed "lag". Shear strains developing along cracks as result of this "lag" are taken into account as partially slip deformations along cracks.

In 2002, Hsu and Zhu proposed a new model called Softened Membrane Model (SMM) (Hsu and Zhu, 2002). The only difference of this model with the FA-STM was that it considered the Poisson's effect. It was also concurred that the influence of the "kinking effect" on the response, which had been identified in development of the FA-STM, was not as important as stated previously. In 2005 a cyclic version of the SMM was proposed by Mansour and Hsu (Mansour and Hsu, 2005). In this study, 12 panel specimens were tested under reversed cyclic loading for development of the formulation of the proposed model, as well as for assessment its prediction capabilities.

Another well-known approach for constitutive modeling of RC panels is implementation of the "microplane" approach developed by Bazant et al. (1996), which

accounts for the interaction between axial, transverse, and shear strain fields at the concrete and steel material levels based on basic uniaxial stress-strain relationships for steel and concrete. The structural response was then determined by monitoring uniaxial stress-strain relationships on the microplanes. A typical discretization with eight microplanes was assumed in which all microplanes in a concrete fiber have the same uniaxial stress-strain relationships (assuming isotropy). Longitudinal reinforcing bars were modeled using steel fibers in the directions of the reinforcement, while transverse reinforcement at each cross-section was represented as a tributary reinforcement within the concrete fiber formulation. The stress-strain relationship for steel was idealized as a multilinear curve with a "gradual-softening" to take into account for the Bauschinger effect. In modeling of reinforcing steel, only the axial stresses and strains were considered (dowel action on the reinforcement was neglected).

For coupling of nonlinear flexural and shear responses in RC walls, a recommended approach by Takayanagi *et al.* (1979) involves modeling of the the shear force–displacement envelope relationship with the same yielding point (yielding force) as required to reach flexural yielding. An indirect approach to combine flexure and shear behavior is to use a limit state model proposed by Elwood (2002). It is based on results of experimental studies of columns exhibiting shear and flexure critical failure. Two limit states were considered in this study, one for the shear force and one for the axial load, and both related to the total lateral displacement. The total response is limited by the shear curve (Figure 1.1), reducing the shear force at larger displacements in the shear force limit case.

Orakcal and Wallace (2006) conducted an analytical study to experimentally validate the Multiple-Vertical-Line-Element Model (MVLEM) (Orakcal *et al.,* 2004) for relatively slender structural walls. The model formulation included material characteristics and behavioral response features, for example, neutral axis migration, tension-stiffening, progressive gap closure and nonlinear shear behavior. The test results obtained for two approximately quarter-scale wall specimens tested by Thomsen and Wallace (1995) were used for experimental validation of the model. One of those specimens had a rectangular cross section and the other specimen had a T-shaped cross section. Test measurements were processed to allow a direct comparison of the predicted and measured flexural

responses. The responses were compared at various locations on the walls by proper instruments. Results showed that rectangular walls had some variation for local compression strains and for T-shaped walls the model was not able to capture the variation of the longitudinal strains along the flange.

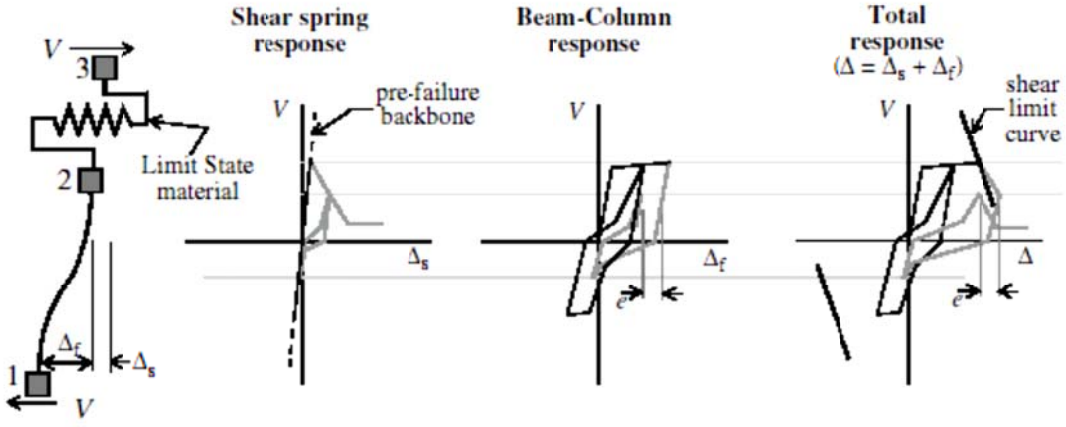

Figure 1.1. Shear spring with shear limit curve (Elwood, 2002).

In the MVLEM, the relative rotation between top and bottom faces of the wall element (curvatures) are concentrated at the center of rotation defined for each element at the height assuming a constant value (uniform distribution) of wall curvature over the height of each wall element, as oppose to the displacement-based fiber model in which linear variation of curvature is used between the element nodes. The MVLEM was improved by implementing refined hysteretic uniaxial stress-strain material models instead of simplified force-deformation rules (Fischinger *et al.*, 1990) to predict the inelastic response of slender RC walls. The stress-strain model for reinforcing steel was the hysteretic model of Menegotto and Pinto (1973), as extended by Filippou *et al.* (1983) to include isotropic strain hardening effects. Uniaxial behavior of concrete was described by the constitutive model proposed by Chang and Mander (1994), which has the capabilities of addressing important features of concrete hysteretic behavior such as the progressive degradation of stiffness of the unloading and reloading curves for increasing values of strain, the effects of confinement, tension stiffening and gradual crack closure. The cyclic properties of flexural load-deformation response, including stiffness degradation, hysteretic shape, plastic (residual) displacements, and pinching behavior are accurately predicted by

the MVLEM. However, similarly to the original MVLEM, this model fails to incorporate coupling of flexural and shear responses, and is intended to simulate the response of slender walls, for which shear deformation levels are relatively low.

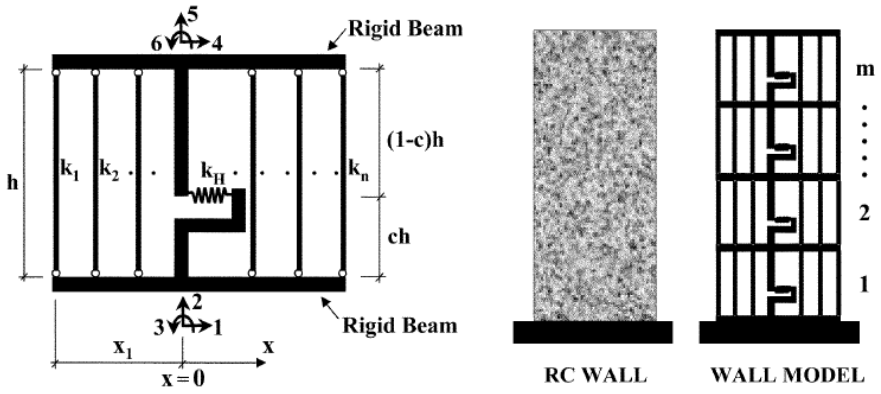

Figure 1.2. MVLEM (Orakcal *et al.*, 2004).

For experimental evaluation of the coupling of nonlinear flexural and shear responses in slender walls, the two experimental programs conducted by Thomsen and Wallace (2004) and Sayre (2003) were investigated in detail by Massone (2006). Two, approximately quarter-scale, slender cantilever RC wall specimens were used to assess the relative deformations associated with shear and flexure: RW2 tested by Thomsen and Wallace (2004), and SRCW1 tested by Sayre (2003). Wall specimens were proportioned and detailed using a capacity design approach for shear and a displacement-based design approach for wall boundary element detailing. Specimen RW2 was 3.66 m tall and 102 mm thick, with a web length of 1.22 m, while specimen SRCW1 was 4.88 m tall, 152 mm thick, and 1.22 m long. Specimens were tested in the upright position under reversed cyclic loading conditions and a constant axial load of approximately $0.10A_g f_c'$. Cyclic lateral displacements were applied to the walls by a hydraulic actuator at 3.81 m above the base of specimen RW2, and at 4.88 m above the base of specimen SRCW1; therefore, shear-span-to-depth ratio, or aspect ratio (h_w / l_w), of wall specimens RW2 and SRCW1 were 3.0 and 4.0, respectively. Both wall specimens were heavily instrumented to measure displacements, loads, and strains at critical locations. Wire potentiometers (WPs) were mounted to a rigid steel reference frame to measure lateral displacements over the wall height. Displacements measured with the WPs were corrected using the measurements

from linear potentiometers (LPs) mounted horizontally and vertically on the wall foundation, which measured any horizontal slip of the foundation block (pedestal) along the strong floor as well as rotations caused by uplift of the pedestal from the strong floor.

Shear deformations within the first two levels of specimen RW2 and first three levels of specimen SRCW1 were determined using measurements from WPs placed on the walls diagonally in an "X" configuration. Vertically oriented linear variable differential transducers (LVDTs) over the wall length just above the wall-pedestal interface were used to obtain average axial strains and to enable calculation of section curvatures. Strains in the reinforcing steel were measured using strain gauges mounted near the wall base and at other locations. Further details of experimental programs are provided in papers by Thomsen and Wallace (2004) and Sayre (2003), and an evaluation of the test results, in terms of coupling of the flexural and shear responses, is presented in the Ph.D. Thesis by Massone (2006).

For experimental evaluation of shear-controlled responses and coupling of flexural and shear deformations in squat walls, an test program was conducted at the University of California Los Angles (UCLA) Structural/Earthquake Engineering Research Laboratory (SEERL) on the performance of low-rise lightly-reinforced RC walls and spandrels in existing buildings that had been constructed between the 1950s and 1970s (Orakcal *et al.,* 2009). As a result of this study, the most important factors in the nominal shear strength of such walls were found to be the amount of boundary reinforcement provided, presence of axial load and the location of a weakened plane joint on the wall. The test results were compared with predictions of a monotonic shear-flexure interaction model by Massone *et al.* (2009). Eleven squat wall specimens having different aspect ratios and different reinforcement configurations were also tested by Terzioğlu (2011), as part of an experimental program conducted at Bogazici University Structural Engineering Laboratory to investigate the shear-dominated lateral load behavior of squat structural walls. The test results identified different failure modes that can be experienced by squat walls, based on their geometry and reinforcement characteristics. The behavior modes identified in this study included diagonal tension failure, diagonal compression failure, sliding shear at wall base, and shear-flexure coupling behavior.

A relatively new cyclic shear-flexure interaction modeling approach was developed by Kolozvari *et al.* (2012). The model was validated by comparing the model predictions with experimental results obtained by Tran and Wallace (2012). The experimental study included five one-third scale cantilever RC wall specimens subjected to combination of constant axial load and reversed cyclic lateral loading applied at the top of the walls. Specimens were heavily instrumented to obtain detailed response information. The primary objectives of the test program were to investigate the impact of level of axial stress and average shear stress on the wall failure modes and lateral deformation capacity, as well as to assess the distribution and magnitude of lateral deformations associated with shear and flexure. The primary test variables included wall aspect ratio (1.5 and 2.0), axial load level ($0.025\,A_g\,f_c^{'}$ and $0.10\,A_g\,f_c^{'}$). The five RC wall specimens were 15 cm thick and 1.22 m long, with lateral load applied at either 1.83 m or 2.44 m above the wall-foundation block interface, i.e. aspect ratio of walls was 1.5 and 2.0, respectively. The ratios of horizontal and vertical web reinforcement are the same and higher than the minimum requirement of 0.25%. The minimum and maximum ratios of vertical boundary reinforcement ρ_b for the five specimens were 3.23% and 7.11%. Specimens were designed to yield in flexure before reaching the ACI 318-11 nominal shear strength. Test results indicated that substantial loss of lateral load capacity was observed at approximately 3.0% drift for all test specimens, with significant strength loss was impacted by wall aspect ratio, axial load level, and shear stress level. Reasonably accurate response predictions were obtained with the shear-flexure-interaction model proposed by Kolozvari *et al.* (2012) for the wall specimens with moderate aspect ratios. The response of the wall specimens tested by Tran and Wallace (2012) were mostly flexural in nature (with yielding of longitudinal boundary reinforcement), although significant levels of shear deformation were recorded during the tests.

Zhang and Xu (2010, 2012) developed a modeling methodology based on the concentrated plastic hinge approach that captures the interaction between axial, flexural and shear responses in RC columns. Inelastic response is modeled by the use of flexural and shear springs located in the column plastic hinge regions, whose behavior is governed by the flexural and shear backbone curves and a set of leading/unloading rules to describe the hysteretic characteristics of the response (e.g., pinching behavior, loading/re-loading

stiffness, softening and strength degradation); hysteretic model for shear by Ozcebe and Saatcioglu (1989) and hysteretic model for flexure by Takeda *et al.* (1970) were used as a basis to develop two improved hysteretic models for flexure and shear responses, respectively. Flexural and shear backbone curves are obtained by separating flexural and shear deformations from the total monotonic force-displacement relationship (backbone curve) of a column that accounts for shear-flexure interaction, which can be obtained either experimentally or analytically. In the modeling approach proposed by Zhang and Xu, the moment curvature and the shear force-shear strain relationships are obtained for each section of a RC column by the use of Modified Compression Field Theory (MCFT, Vecchio and Collins 1986) based on the column geometry, reinforcement configuration, material properties, and applied external loads. Subsequently, the flexural deformation and shear deformation are obtained by integrating the curvature and shear strain in each section along the column length, which yield the bending moment-to-rotation angle and shear force-to-shear displacement relationships used to define the envelopes of force-deformation behaviors of flexural and shear springs. Thus, the analytical model captures shear-flexure interaction at both section level, when theoretically generating the backbone curves, and at element level, through global and local equilibrium.

The proposed analytical model was used to simulate the behavior of two aspect ratio 2.0 RC walls tested by Lefas and Kotsovos (1990), specimen SW31 tested under monotonic loading and specimen SW33 tested under cyclic loading, as well as the behavior of RC columns that experienced shear-dominated behavior. The comparisons between the experimental and analytical results revealed that the model captures reasonably well the overall load-deformation response of considered wall specimens under monotonic and cyclic loading, as well as the vertical strains at the wall boundary. In addition, Mullapudi *et al.* (2009) investigated the sensitivity of analytical model results under monotonic loading to changes in wall slenderness ratio, transverse reinforcement ratio, and axial force using specimen SW 31 as the baseline model. Analytical results showed that the model captured systematic changes in local wall responses (e.g., normalized shear stress, distribution of normalized principal strains, and longitudinal boundary strains) with changes in mentioned wall parameters, whereas the sensitivity of global responses (e.g., lateral-load-versus-total-displacement) were not provided. Although the analytical model provided reasonably accurate predictions of behavior of moderate aspect ratio RC walls, the model validation

studies were presented for a limited number of RC walls specimens (one monotonic and one cyclic test) as well as limited range of wall responses, i.e., lateral-load-versus-top-wall-displacement response and vertical boundary strain only, which are not overly sensitive to shear-flexure interaction.

A new macroscopic finite element modeling approach was proposed by Gullu (2013) for simulating the inelastic response of RC walls under generalized reversed-cyclic loading conditions. The proposed model incorporated the fixed crack angle constitutive modeling approach developed by Ulugtekin (2010). The main purpose of this study was to provide reasonable predictions of the unexpected shear yielding and nonlinear shear deformations in slender walls. The analytical model was shown to capture, with reasonable accuracy, overall behavioral attributes of RC structural walls, including cyclic lateral load versus shear distortion, lateral stiffness, strength and ductility. Nonlinear force-deformation responses predicted by the analytical model also reflected important cyclic response characteristics; including stiffness degradation, plastic displacements, and pinching behavior. For checking the sensitivity of the analytical model results to modeling parameters, parametric sensitivity studies were also conducted. However, accuracy of the proposed model was not evaluated for squat walls, which exhibit more complicated responses governed by nonlinear shear deformations.

1.3. Objectives and Scope

Although the lateral load behavior of structural walls has been widely investigated both experimentally and analytically, and there are numerous modeling approaches available in the literature for simulating their seismic response, most of the available modeling approaches focus on characterization of the nonlinear flexural response of walls, or coupling of nonlinear flexural deformations with moderate levels of shear deformation. Existing approaches to model coupled shear and flexural responses typically incorporate ad-hoc modeling assumptions, some of which have not been experimentally validated against experimental data obtained for squat walls with shear-controlled responses. There is still a need for a robust modeling approach to simulate the nonlinear hysteretic behavior of such walls.

Accordingly, the objective of this study is to implement and experimentally-validate a new finite element modeling methodology for simulating the in-plane hysteretic lateral load behavior of squat walls, with aspect ratios smaller or equal to 1.0, the response of which are governed by nonlinear shear deformations. The behavior of the constitutive panel (membrane) elements in the finite element model is described by a previously-developed constitutive panel model (the Fixed-Strut-Angle Model by Ulugtekin, 2010). Improvements were made on the constitutive panel model formulation, for better representation of the shear-aggregate-interlock effects in concrete and dowel action in reinforcing bars, constituting transfer of shear stresses across the cracks of the constitutive panel elements. Sensitivity studies were conducted on the influence of the parameters associated with the constitutive shear-aggregate-interlock and dowel relationships on the model results. The model was extensively calibrated for the squat wall specimens tested by Terzioglu (2011), and model predictions were compared with the experimentally-observed lateral load vs. displacement responses.

1.4. Thesis Outline

This thesis presents information on the modeling approach used, constitutive relationships incorporated in the model formulation, calibration of the model parameters, and comparison of model predictions with test results on squat walls. In Chapter 1, an introduction and a literature review, as well as the objectives and scope of this study were provided. Descriptions of constitutive panel model, the finite element modeling approach, and shear transfer mechanisms across cracks are presented in Chapter 2. Chapter 3 presents information on the test program used for experimental validation of the model and calibration of the model parameters. Analysis results, sensitivity studies, and comparison of the model results with test data are presented in Chapter 4. Finally, concluding remarks and recommendations for future studies are presented in Chapter 5.

2. MODEL DESCRIPTION

2.1. Overview

This Chapter provides a summary of the constitutive panel model formulation, the constitutive material relationships implemented in the model, the adopted macroscopic finite element modeling methodology, and the constitutive relationships implemented to represent transfer of shear stresses across cracks. Finite element modeling of RC structural walls involves assembling of constitutive panel elements for obtaining the model of a RC structural wall. Hysteretic nonlinear material behavior along crack directions of the constitutive panel, as well as behavioral response characteristics including compression softening, tension stiffening, hysteretic biaxial damage, and shear transfer across cracks, constitute the behavior of the wall model.

The Fixed Strut Angle Model (FSAM) proposed by Ulugtekin (2010) was selected as the constitutive panel model to be for implemented in the finite element model assembly, since its simple formulation and adequate accuracy makes it a feasible candidate for implementation. Formulation of the FSAM is based on interpretation and simplification of previously-developed RC panel models, and the results of RC panel tests available in the literature. A summary of the FSAM formulation is provided in the next section, whereas detailed information on the FSAM is available in the thesis by Ulugtekin (2010).

In the present study, the formulation of the original FSAM was modified. In the original version of FSAM proposed by Ulugtekin (2010), the effects of shear aggregate interlock and dowel action across cracks were neglected. Due to the resulting assumption of zero shear stress developing along crack surfaces, significant overestimation of sliding shear strains may occur along crack directions. Therefore, to simulate shear aggregate interlock effects in concrete, a simple friction-based constitutive model was implemented into the panel model formulation by Orakcal *et al.* (2012), and adopted by Gullu (2013). In this study, in addition to shear aggregate interlock effects, a new nonlinear hysteretic constitutive relationship was adopted to represent the contribution of reinforcing bars

(dowel action) to shear stresses developing along crack surfaces. Constitutive modeling of shear aggregate interlock behavior in concrete and dowel effects on reinforcement in the present model formulation are presented in subsequent sections.

2.2. Constitutive Panel Model

The original constitutive panel model formulation (FSAM, Ulugtekin, 2010) incorporates the perfect bond assumption between concrete and reinforcing steel, and neglects shear aggregate interlock effects and dowel action along crack surfaces. The strain field acting on concrete and reinforcing steel components of an RC panel are assumed to be equal to each other as the result of perfect bond assumption. While uniaxial directions along the rebar directions were used for the hysteretic constitutive modeling of reinforcing steel bars, biaxial relations along the fixed strut (crack) directions were incorporated for constitutive modeling of concrete stress-strain behavior.

For simulation of the biaxial stress-strain behavior of uncracked concrete, a rotating strut approach, similar to the Modified Compression Field Theory (Vecchio and Collins, 1986) and the Rotating Angle Strut and Tie Model (Pang and Hsu, 1995) was used. The hysteretic behavior of concrete was assumed to be monotonic for small strains prior to cracking, for the uncracked loading stages. The principal strains directions acquired from the applied strain field were assumed to coincide with principal stress directions in concrete. Therefore, the constitutive material model for concrete is determined along the principal strain directions (Figure 2.1).

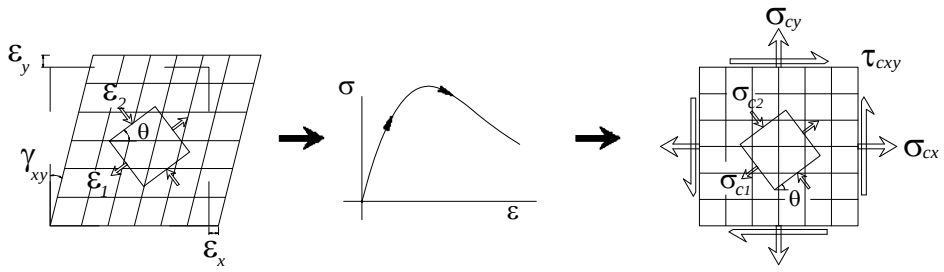

Figure 2.1. Uncracked behavior of concrete in the Fixed Strut Angle Model (Orakcal *et al.*, 2012).

The first crack in the RC panel forms in a perpendicular direction to the principal tensile strain, as the principal tensile strain exceeds the monotonic cracking strain value of concrete. This implies that for subsequent loading, the first "Fixed Strut" direction is already assigned, and it is parallel to the first crack. For subsequent loading stages, principle strain directions continue to rotate with the applied strain field whereas principal stress directions in concrete coincide with the first crack direction (parallel and perpendicular). Since principal stress and crack directions coincide, zero shear stress develops along the crack directions, implying zero shear aggregate interlock and zero dowel action, which is the underlying assumption in the original FSAM formulation.

The hysteretic stress-strain relationship for concrete is used in parallel and perpendicular directions to the fixed strut after formation of the first crack. It is only possible to calculate the principal stresses in concrete with the transformation of the strain field into directions parallel and perpendicular to the fixed strut. Using the uniaxial constitutive model adopted for concrete, concrete stress values are determined after the calculation of the strains that are parallel and perpendicular to the fixed strut direction. These calculated stresses are reduced by biaxial compression softening and biaxial damage parameters, which are described in the following section. The stresses in reinforcing steel are calculated by the implementation of the hysteric uniaxial constitutive material model for reinforcing steel is applied along the orthogonal rebar directions. The average stresses on the panel element are provided by superposition of stresses developing in concrete and reinforcing steel. Behavior of concrete in the FSAM after formation of the first crack is illustrated in Figure 2.2.

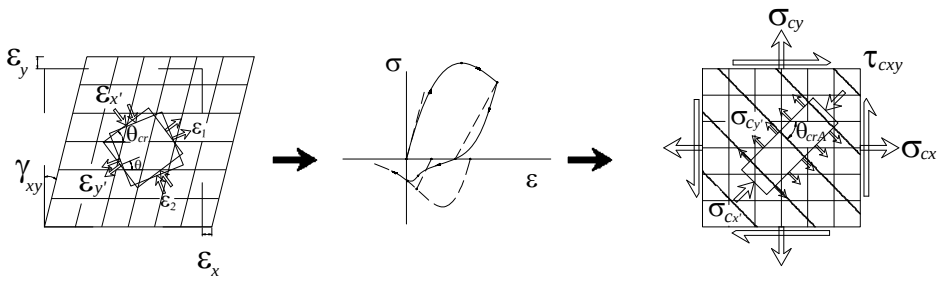

Figure 2.2. Behavior of concrete after formation of first crack in the Fixed Strut Angle Model (Orakcal *et al.*, 2012).

As the tensile strain exceeds the cyclic cracking strain of concrete, the second crack is formed perpendicular to the first crack because of the zero shear stress assumption along the crack directions. Until that stage, the constitutive behavior proceeds in the form of a single fixed strut mechanism. The first and second cracks being perpendicular is an example of the so-called "orthogonal crack" modeling approach, which has also been adopted in other constitutive panel model formulations. The second crack, being perpendicular to the first fixed strut, implies the formation of the second "fixed strut" direction. These fixed struts work under tension or compression, depending on the loading direction. For subsequent loading stages, principle stress directions are fixed along the fixed strut directions while principal strain values are able to rotate freely. The applied strain field is transformed into strain components in the fixed strut directions instead of principal strain directions in order to determine the principle stresses in concrete. To obtain the principle stresses in concrete, calculated strain values are used in the uniaxial constitutive model for concrete. The concrete stresses are reduced by compression softening and biaxial damage parameters. The constitutive material model for reinforcing steel is applied along the orthogonal rebar directions and superposition of stresses developing in concrete and reinforcing steel gives the resultant average stresses on the panel element. Behavior of concrete in the FSAM after formation of the second crack is illustrated in Figure 2.3.

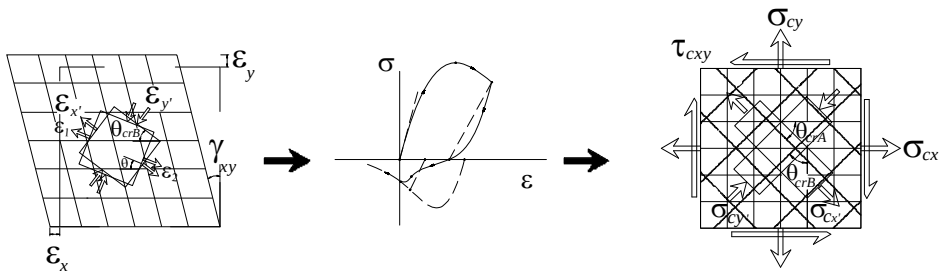

Figure 2.3. Behavior of concrete after formation of second crack in the Fixed Strut Angle Model (Orakcal *et al.*, 2012).

2.3. Constitutive Material Models

2.3.1. Constitutive Model for Reinforcement

In the constitutive panel model (FSAM), the behavior of reinforcing steel is represented by the well-known nonlinear hysteretic relationship of Menegotto and Pinto (1973), as extended by Filippou *et al.* (1983) to incorporate isotropic strain hardening effects. The constitutive model also represents the so-called Bauschinger's effect, by incorporating cyclic degradation of tangent stiffness in the unloading and reloading curves. A description of the constitutive model is shown in Figure 2.4.

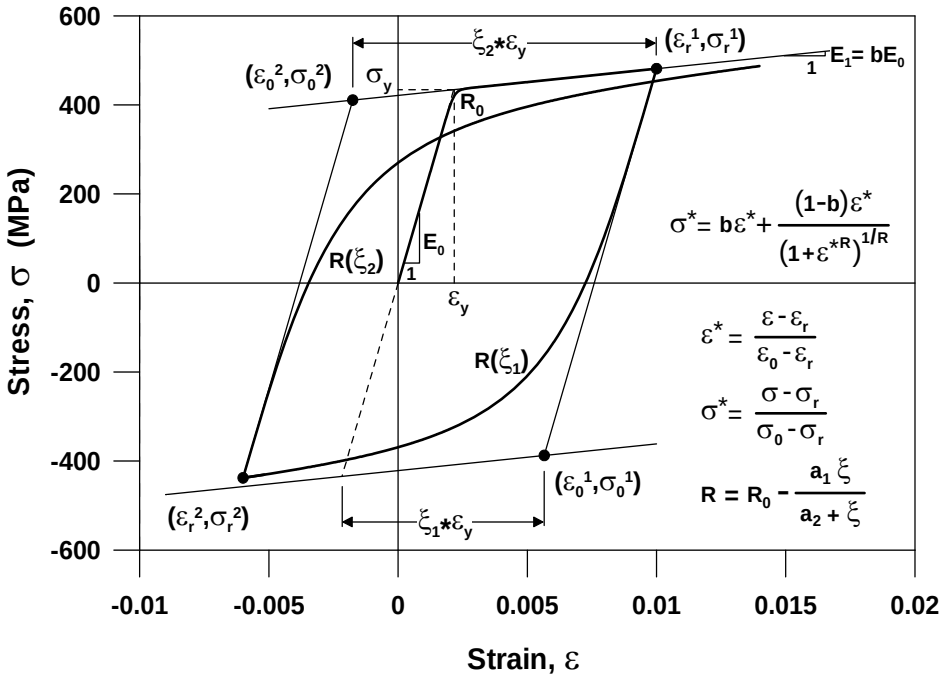

Figure 2.4. Hysteretic constitutive model for reinforcing steel (Menegotto and Pinto, 1973).

2.3.2. Constitutive Model for Concrete

The uniaxial hysteretic constitutive model proposed by Chang and Mander (1994) was adopted in the FSAM to represent the uniaxial hysteretic stress–strain behavior of concrete along fixed strut directions. The advantage of the Chang and Mander (1994)

Model is that it is a rule-based, generalized, and non-dimensional model that can simulate the hysteretic behavior of both confined and unconfined concrete, under continuous compression and tension loading. The Chang and Mander (1994) Model has been shown to provide accurate representations of experimental results presented by various researchers. For unconfined concrete in cyclic compression, a reasonable assumption based on experimental results was presented by Karsan and Jirsa (1969), and modeled by Mander *et al.* (1988a). Mander *et al.* (1988b) performed tests for confined concrete and confirmed the model accuracy. The experiments conducted by Gopalaratnman and Shah (1985) and Yankelevsky and Reinhardt (1987) showed that the behavior of concrete in tension is similar to the behavior of concrete in compression. Therefore, the model by Chang and Mander (1994) recommends similar envelopes for tension and compression (Figure 2.5), with different stress magnitudes.

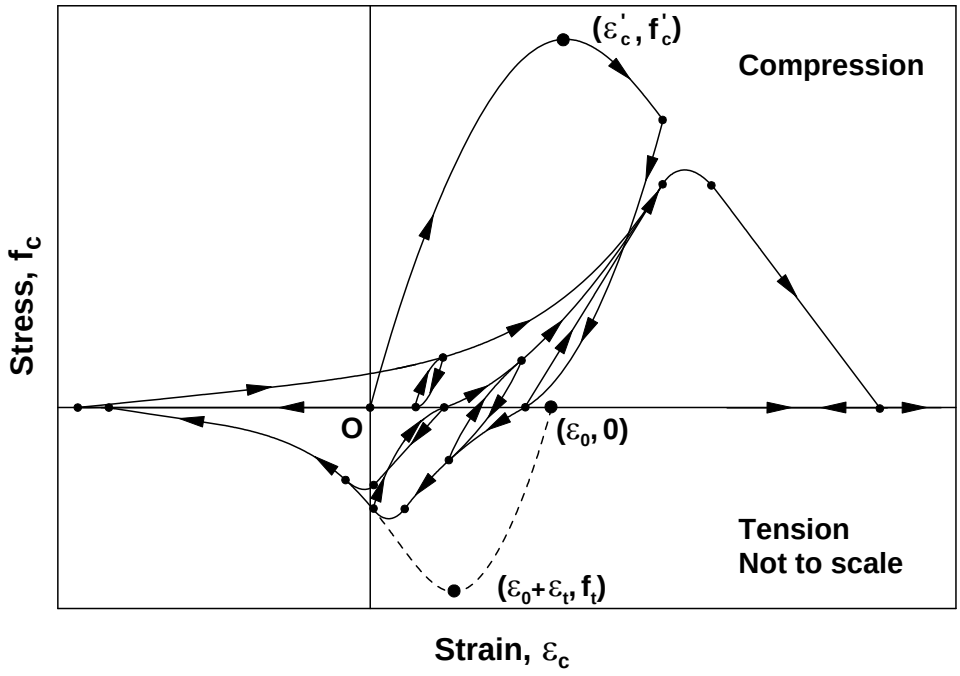

Figure 2.5. Hysteretic constitutive model for concrete (Chang and Mander, 1994).

In the FSAM, the formulation of the Chang and Mander (1994) model was modified by incorporating paramaters to represent compression softening (defined by Vechio and Collins, 1993), hysteretic biaxial damage (defined by Mansour *et al.*, 2002), and tension stiffening effects (defined by Belarbi and Hsu, 1994) into its formulation. These

modifications, which are described in the following sections, aim to simulate the behavioral features of concrete subjected to biaxial loading along the perpendicular strut directions.

2.3.3. Compression Softening Effect on Concrete

Compression softening effect is an important consideration in modeling the behavior of RC panel elements. Although the behavior of concrete under biaxial stress state was first determined by Kupfer, Hilsdorf and Rüsch in 1964, the softening effect has been experimentally observed by many other researchers, (e.g., Vecchio and Collins, 1986) and representative constitutive relationships were proposed. Compression softening is the reduction in the compressive stresses in concrete along the principal compression direction of RC panels, stemming from the tensile strains perpendicular to crack directions (Figure 2.6).

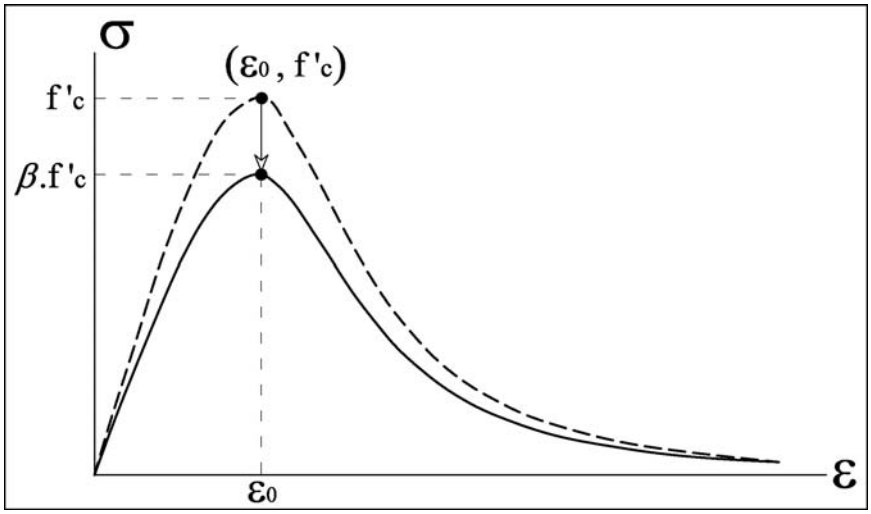

Figure 2.6. Compression softening effects implemented in the panel model (Ulugtekin, 2010).

The compression softening relationship proposed by Vecchio and Collins (1993) was implemented into the formulation of the Fixed Strut Angle Model. More complicated models representing compression softening effects are available in the literature; however,

this relationship was found to provide reasonably accurate predictions of experimentally-observed stress vs. strain behavior, despite its relatively simple formulation.

2.3.4. Tension Stiffening Effects on Concrete and Reinforcing Steel

Tension stiffening is defined as the contribution of cracked concrete to the tensile resistance of RC members. The post-cracking stiffness, yield capacity and shear behavior of the RC members have been shown to be influenced by the tension stiffening effect. The effect of tension stiffening has been studied by many researchers (e.g. Vecchio and Collins, 1988; Stevens , 1987; Collins and Mitchell, 1991; Belarbi and Hsu, 1994; Pang and Hsu, 1995; Hsu and Zhang, 1996; Mansour *et al.*, 2002; Hsu and Zhu, 2002).

The tension stiffening relationship that was proposed by Belarbi and Hsu (1994) was implemented in the formulation of the constitutive panel model. The tension stiffening phenomenon considers two significant effects simultaneously. The first one is the consideration of an average (smeared) tensile stress-strain curve for cracked concrete; and the second one, replacement of the uniaxial stress-strain relationship of bare reinforcing bar with an average stress-strain curve of defined for bars stiffened by concrete between cracks.

2.3.5. Biaxial Damage Effect on Concrete

Another significant consideration in modeling the behavior of an RC panel element is the cyclic damage effects on concrete subjected to biaxial loading. This damage on concrete is represented with a damage coefficient. The damage coefficient is a cyclic-strain-history-dependent parameter unlike compression softening and tension stiffening parameters. The biaxial damage effect physically reflects as softening in the compressive stress-strain behavior of concrete along one direction, depending on the maximum value of the previously-applied compressive strain in the perpendicular direction. The biaxial damage behavior is therefore loading-history-dependent and is not observed under monotonic loading. In terms of constitutive modeling, the damage coefficient, similar to the compression softening coefficient, is typically applied as a reducing multiplier to compressive stresses in concrete. The damage coefficient, similar to the compression

softening coefficient, is typically applied as a reducing multiplier to compressive stresses in concrete.

There are two models for the damage coefficient in the literature; Stevens (1987), Mansour and Hsu (2002). The biaxial damage formulation proposed by Mansour and Hsu (2002) was implemented into the formulation of constitutive Fixed Strut Angle Panel Model.

2.3.6. Constitutive Modeling of the Shear Aggregate Interlock Effect in Concrete

The shear aggregate interlock effect along crack surfaces in concrete were neglected in the original formulation of the Fixed Strut Angle constitutive panel model developed by Ulugtekin (2010). A simple friction-based elasto-plastic shear aggregate interlock model was implemented into the panel model formulation by Orakcal *et al.* (2012). The cyclic shear aggregate interlock model proposed by Orakcal *et al.* (2012) starts with linear loading/unloading behavior, relating the sliding shear strain along a crack to the shear stress, via a simple linear elastic relationship between the sliding shear strain and the resultant shear stress along the crack surface. The shear stress is restrained to zero value when the concrete normal stress perpendicular to the crack is tensile (crack open); and is bounded via the product of a friction coefficient and the concrete normal stress perpendicular to the crack, when the concrete normal stress is compressive (crack closed). The linear unloading/reloading slope of the shear stress vs. sliding strain relationship was taken as a fraction of the concrete elastic modulus (a value $0.4E_c$ was adopted, representing the elastic shear modulus of concrete), and a value of 1.0 was assumed for the friction coefficient, which needs to be multiplied by the compressive stress in concrete in perpendicular direction to the crack, in order to obtain the shear stress capacity along the crack surface (Figure 2.7). Under constant compressive stress in concrete perpendicular to the crack, this model yields an elasto–plastic aggregate interlock behaviour under cyclic loading, similar to the cyclic stress–strain behaviour of reinforcing steel.

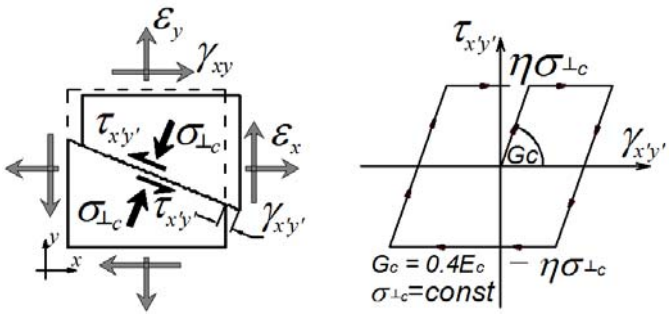

Figure 2.7. Shear-aggregate interlock model (Orakcal *et al.*, 2012).

2.3.7. Constitutive Modeling of Dowel Action on Reinforcing Bars

In this study, in addition to shear aggregate interlock effects described in the previous section, a new nonlinear hysteretic constitutive relationship was adopted to represent the contribution of reinforcing bars (dowel action) to shear stresses developing along crack surfaces. The overall characteristics of the constitutive shear stress vs. shear (sliding) strain model, representing the dowel contribution of reinforcing bars on the shear stresses developing along crack surfaces is illustrated in Figure 2.8.

The overall shape of the constitutive dowel action model was selected to represent the lateral load vs. displacement behavior of squat wall specimens experiencing sliding shear failure at the base, as discussed in Chapter 4 of this Thesis. Therefore, the constitutive dowel action model proposed in this study is more behavioral than mechanical, similarly to the shear aggregate interlock model adopted for concrete. Description of the constitutive dowel action model, including the monotonic parameters and hysteretic unloading/reloading rules, is presented in this section. Hysteretic formulation of the dowel action model is based on three different loading intervals: loading, unloading and reloading. These loading conditions consist of a total of 14 rules, which characterize the overall hysteretic shear stress vs. relationship, for predefined loading intervals. These intervals depend on the incrementation of shear strains within each load step (loading or unloading), as well as material properties and reinforcement characteristics.

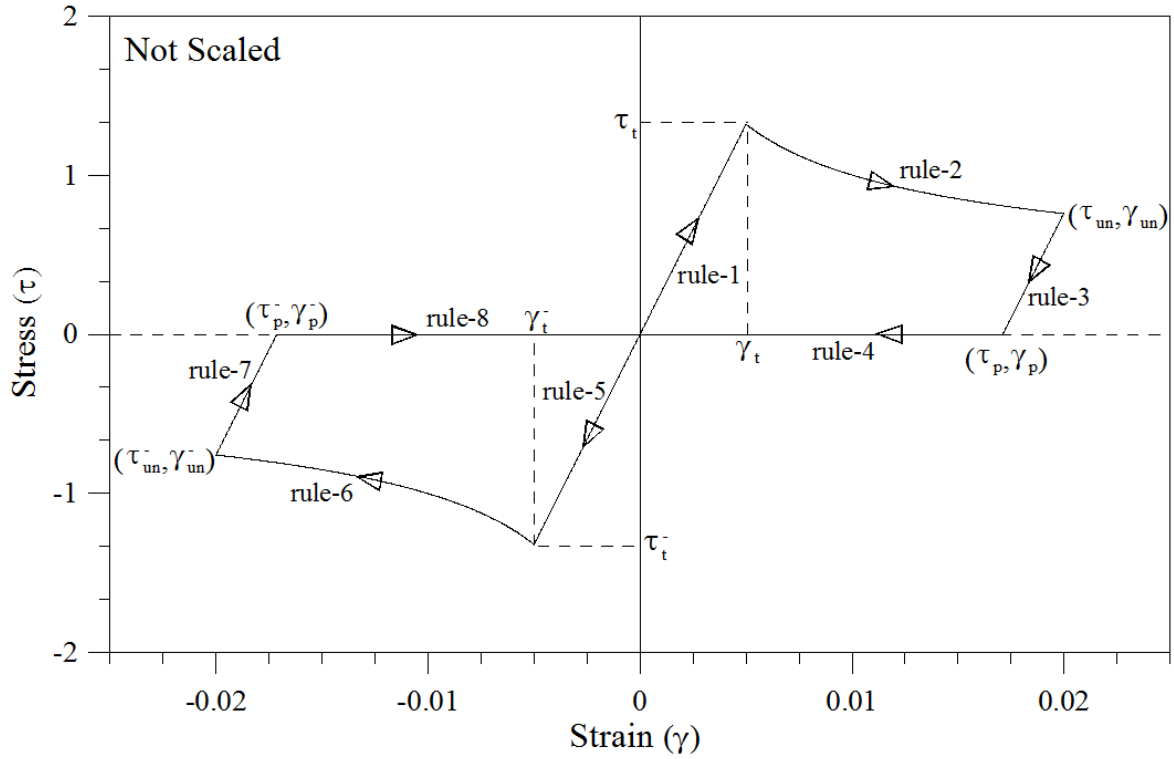

Figure 2.8. The constitutive shear stress vs. strain model adopted to represent dowel action on reinforcing bars.

The monotonic envelope curves of the constitutive shear stress vs. strain model for dowel action are characterized by a linear ascending region, and an exponential descending region, both in positive and negative loading directions. The shear stress capacity (τ_t) is determined as the product of the yield strength of reinforcing steel and the reinforcement ratio (ρ) in perpendicular direction to the crack, further multiplied by a dowel coefficient, which needs to be defined in an ad-hoc manner, based on comparison of the model predictions with experimental results obtained for wall specimens. The slope of the linear ascending region is defined as $0.4 E_s \rho$, where E_s is the elastic modulus of reinforcing steel and the 0.4 coefficient is intended to represent the shear modulus. The reason the shear stress capacity (τ_t) and the linear slope ($0.4 E_s \rho$) incorporate the reinforcement ratio (ρ) is that the shear stresses are later converted into equivalent concrete stresses (smeared along the crack surfaces) in the constitutive panel model formulation. Once the shear stress capacity and linear slope values are assigned, the critical strain (γ_t) value, for which the

descending region of the relationship commences, can be determined by dividing one by the other. The envelope parameters of the constitutive model are thus defined.

In terms of hysteretic behavior, the first interval (named as rule 1), which is the initial linear part of the stress-strain diagram in the positive direction has a linear slope (0.4 $E_s\rho$). The limits of strain are zero strain and critical strain (γ_t) for this interval. The critical strain can be defined as the point where the maximum value of shear stress (τ_t) develops. There is a linear correlation between strain and stress in this interval. The equations, which are valid for both loading and unloading situations in this interval, are expressed as:

$$\tau = (0.4\rho E_s)\gamma \tag{2.1}$$

$$E = 0.4\rho E_s \tag{2.2}$$

where E is the tangent modulus (slope) of the stress-strain relationship. If, at any point during rule-1, unloading is started, the stress-strain diagram moves towards point of origin in compliance with rule-1. In case unloading is continued so that the strain reaches negative values, the relationship continues in the negative direction in a linear elastic manner.

The second interval (named as rule-2) corresponds to the descending region of the stress-strain envelope. The limits of strain for this interval are critical strain and the strain value at which the loading direction for rule-2 is changed. The critical strain is the intersection point of the first and the second intervals. Rule-2 is valid until the next strain value is less than the previous strain value, implying unloading. Since the loading direction is positive throughout rule-2, the corresponding equations are given as:

$$\tau = \tau_t \left(\frac{\gamma_t}{\gamma} \right)^s \tag{2.3}$$

$$E = -s\tau_t \left(\frac{\gamma_t}{\gamma} \right)^{s+1} \tag{2.4}$$

where *s* is a coefficient to be calibrated upon comparison of the model results with test results. The point where unloading is commenced is denoted with γ_{un} (unloading strain at second interval). At this point, rule-2 terminates and rule-3 begins. As long as loading is continued, such a point (γ_{un}) is not assigned and the descending relationship (rule-2) continues. With commencement of unloading, the stress-strain relationship becomes linear, until zero shear stress is reached. At this stage, the slope of the unloading relationship is equal to the slope of the first interval.

As the shear stress reaches zero, that is, the stress-strain relationship intersects the horizontal axis, rule-3 terminates. This intersection point is named as plastic strain, γ_p. If at any point during rule-3, reloading occurs, the diagram follows the same path back towards the unloading strain, γ_{un}. In case when loading still continues after the point γ_{un} is reached, the relationship follows the descending region of the envelope as (rule-2) if unloading was not started. The stress-strain equations for rule-3 are as given below:

$$\tau = \tau_{un} - (0.4\rho E_s)(\gamma_{un} - \gamma) \tag{2.5}$$

$$E = 0.4\rho E_s \tag{2.6}$$

The point where the strain-stress diagram intersects the horizontal axis was denoted by γ_p as mentioned previously. At this point, the fourth stage starts and continues until the strain value approaches the zero strain value towards the origin point of diagram, the stress remaining to be zero. This interval from point γ_p to the point of origin is represented by rule-4, with the following equations:

$$\tau=0; \qquad E=0 \tag{2.7}$$

If at any point during rule-4 (along horizontal axis) reloading is started, the reloading point γ_{re} is defined and the relationship follows the linear path from point γ_{re} on the horizontal axis to unloading point γ_{un} defined previously on the descending envelope curve. This new interval defined in the relationship is represented by rule-101. If loading continues, the relationship extends along the descending envelope (rule-2), beyond the unloading point, γ_{un} .

$$\tau=\frac{\tau_{un}}{\gamma_{un}-\gamma_{re}}(\gamma-\gamma_{re}) \tag{2.8}$$

$$E=\frac{\tau_{un}}{\gamma_{un}-\gamma_{re}} \tag{2.9}$$

If a reloading strain value (γ_{re}) on rule-4 was previously defined, rule-101 is established. If in the subsequent cycles reloading starts at any point during rule-4, where the strain value γ is less than the latest-formed reloading strain γ_{re}, the strain-stress relationship continues along the horizontal axis in the opposite direction, within the original rule-4 interval, until the latest γ_{re} value is reached. The path from the starting point of reloading until the γ_{re} point is defined as rule-41, which is similar to rule-4. Along this interval, the γ_{re} value remains unchanged.

$$\tau=0; \qquad E=0 \tag{2.10}$$

Under continued loading, the relationship moves forth from the γ_{re} point to the latest-formed γ_{un} value. This path from the latest γ_{re} point to the latest γ_{un} point on the descending envelope curve (rule-2) was defined as rule-101 in the relationship. In case loading still continues after γ_{un} is reached, the diagram follows the descending envelope curve.

If reloading is started at a strain value γ that is larger than the latest-formed γ_{re} value, the relationship continues from this strain value on the horizontal axis until a new reloading point γ_{re} is defined and follows the linear path from that point to the latest-formed unloading strain γ_{un} defined on the descending envelope curve (rule-2). This path updates the formerly-defined rule-101. With the definition of the new γ_{re} value, the new value becomes effective for the subsequent loading-unloading cycles. If loading continues, the relationship extends to the descending envelope curve beyond the existing point γ_{un}, causing γ_{un} to be renewed upon subsequent unloading. The updated γ_{un} value causes the formerly–defined γ_{un} value to become invalid.

If unloading commences at any point within rule 101, this results in the formation of a new reversal point nominated as γ_{unre}. The strain-stress relationship progresses linearly from that point towards the horizontal axis, parallel to rule-3, until it intersects the horizontal axis. The intersection point is named γ_{unret}. The corresponding line from γ_{unre} to γ_{unret} is identified as rule-111 in the relationship. If reloading continues, the relationship follows the path from γ_{unret} along the horizontal towards the origin, i.e. along the existing path of rule-4.

$$\tau = \tau_{unre} - (0.4\rho E_s)(\gamma_{unre} - \gamma) \tag{2.11}$$

$$E = 0.4\rho E_s \tag{2.12}$$

It was noted that rule-4 is terminated at the origin . As the strain continues to increase in the negative direction, a point-symmetrical relationship with respect to the origin is obtained for negative strains, which starts with a linear relationship with the same slope in the negative loading direction, from the origin until the point of critical strain, defined as rule-5. Rule-5 is valid in the case that the strain reaches negative values for the first time. The hysteretic behavior in the positive strain region is illustrated in Figure 2.9.

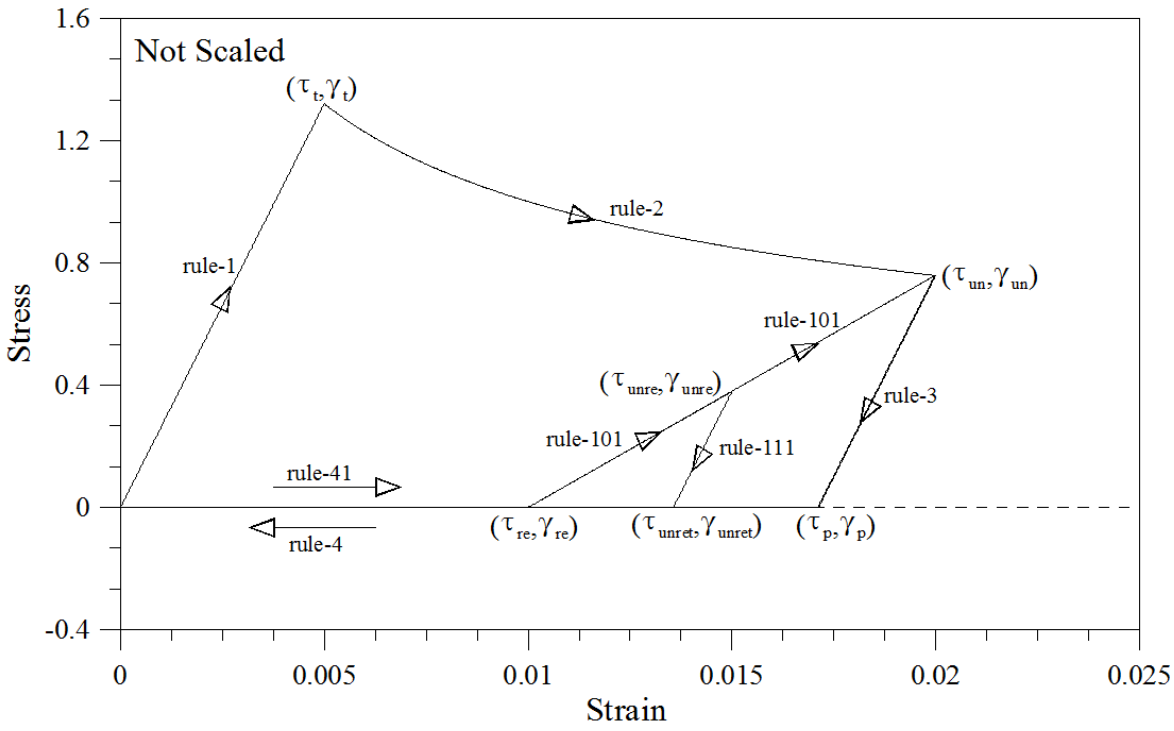

Figure 2.9. Shear stress-strain relationship in the positive strain region.

The strain-stress relationships in the negative strain region are identical to the relationships defined for positive strains, defined by rules 1, 2, 3 and 4. Continued loading in the negative direction is defined by the descending envelope curve in the negative direction, defined as rule-6. Unloading from the negative envelope is defined by rule-7 and rule-8, where the relationship approaches back to the origin. Continued loading in the positive direction starts a new cycle in the positive strain region.

During the new loading cycle in the positive direction, the relationship does not follow rule-1 and rule-2, as it did during the first loading cycle. The strain-stress relationship follows a new linear path from the point of origin to point γ_{un}, provided that γ_{un} was established during the first or former loading cycle, but the reloading strain value γ_{re} was not yet established. This new linear path from the point of origin to the point γ_{un} is nominated by rule-101. On the contrary, in case that γ_{re} point was also established during a previous cycle, the strain-stress relationship follows the path from the origin to the existing point γ_{re}, along namely rule-41, and from that point to the unloading point γ_{un}

along the formerly-established linear path 101. If unloading starts at the point γ_{un}, the diagram follows the path of rule-3 to the originally-formed point γ_p, otherwise it follows the continuation of the descending envelope curve (rule-2) beyond the point γ_{un}. Thus, continued reloading causes formation of a new γ_{un} value further in the positive loading direction, where unloading is recommenced. This results in the formation of the new path for rule-3, parallel to the former path, and definition of a new point γ_p at the intersection of the updated rule-3 and the horizontal axis.

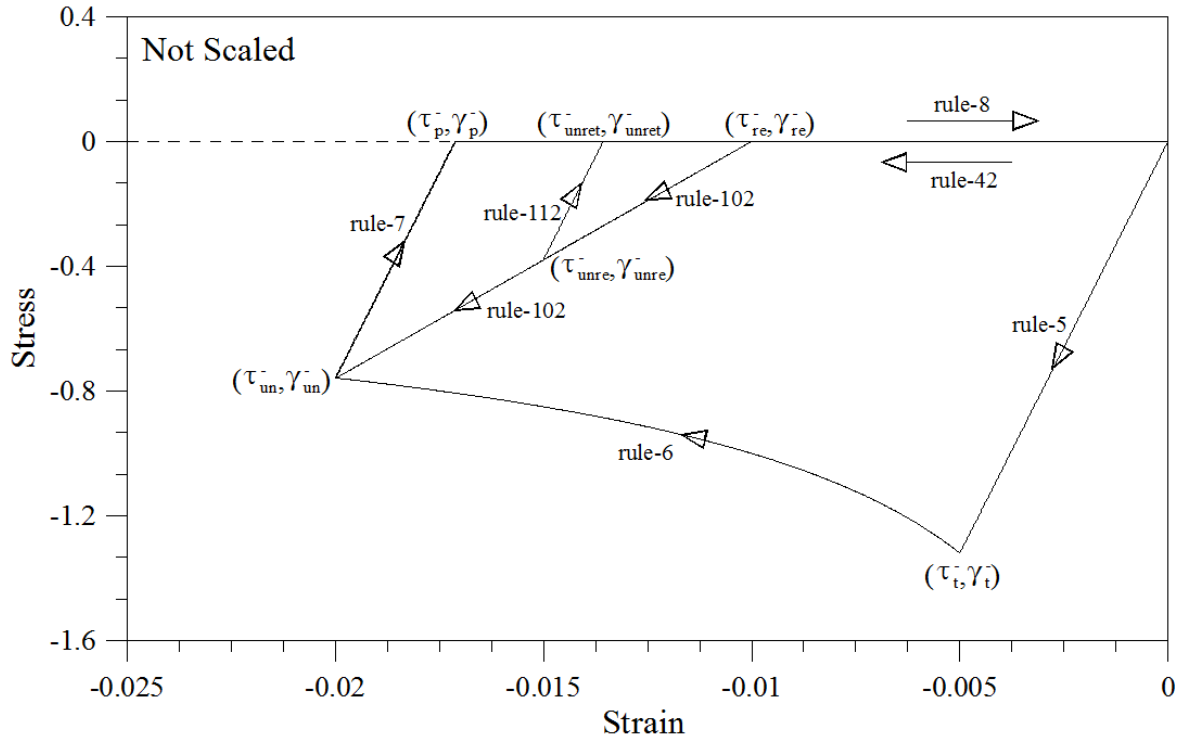

Figure 2.10. Shear stress-strain relationship in the negative strain region.

Similarly, once the point γ_{un}^{-} (unloading strain in the negative region) is established during the first loading cycle in the negative direction on the path of rule-6, the relationship follows, during the subsequent loading cycles, the path from the origin to the existing γ_{un}^{-} value, following the linear path defined by rule-102. In case the point γ_{re}^{-} (reloading case in the negative region) was defined during a previous loading cycle, the strain-stress relationship follows a path in negative direction on horizontal x-axis from the point of

origin to the existing point γ_{re}^{-} (defined as rule-42), and from this point to the latest defined point γ_{un}^{-}, along the formerly-established linear path, rule-102. The hysteretic behavior in the negative strain region is illustrated in Figure 2.10.

2.4. Finite Element Modeling Methodology

This section presents a description of the two-dimensional finite element modeling methodology that was used for assembling the constitutive panel elements described in the previous sections into a wall model, similarly to the methodology adopted by Gullu (2013) for modeling of slender walls. Assembly of the local stiffness matrixes as well as the internal force vector of these local elements (mesh elements) are described in the following subsections. Implementation of support conditions and constraints for modeling of walls are also described and the adopted nonlinear analysis solution strategy is summarized. Further details on the finite element model assembly are available in the M.Sc. Thesis by Gullu (2013).

2.4.1. 4 Nodes, 8 Degree of Freedom Rectangular Element

In this study, a rectangular two-dimensional finite element modeling approach was adopted. Four node, eight degree of freedom finite elements were used for modeling of a constitutive element. At each node, the model elements has two degrees of freedom (DOFs), one in vertical and one in horizontal direction. Model elements do not incorporate rotational DOFs. Since the constitutive elements are membrane (panel) elements, only in-plane loading conditions are considered in the formulation of the model. As such, the model does not possess any,out-of-plane stiffness, and only in-plane loads are considered in the analysis.

Each local DOF of the rectangular model element is numbered as shown in Figure 2.11. Average in-plane strains in each model element are calculated using simple linear shape functions, based on the displacement values along the nodal DOFs. (Figure 2.12)

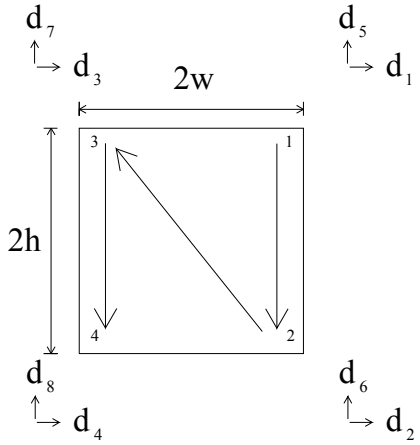

Figure 2.11. Local nodes and DOFs in a rectangular model element.

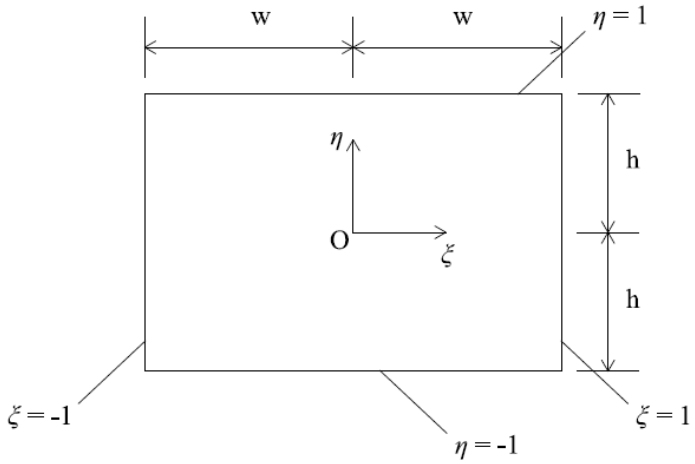

Figure 2.12. Normalized coordinates of a rectangular model element.

Displacement values along horizontal and vertical directions at any point of a rectangular element are obtainable by using the known displacements along the DOFs which are obtained by solving equilibrium equations at the four nodes of the rectangular element, and the shape functions determined in connection with Figure 2.12. Strain and stress values are however only calculated at the center of each rectangular element, corresponding to $\xi = \eta = 0$, for simplicity.

Initial displacements at each node of a structural wall model (eight displacement values for each model element) were calculated at the beginning of analysis for a load step. Following this, deformations of each element are calculated by using the strain transformation matrix. Then, local strain values in each element were calculated by using deformation matrices for each model element. Then, tangent stiffness (elasticity) matrices for each model element were calculated as output values, where strain values were used as input values for the Fixed Strut Angle constitutive model (Ulugtekin, 2010).

The aim is to generate the global tangent stiffness matrix by assembling the local stiffness matrices for the model elements together. Each local stiffness matrix is to be obtained using the tangent stiffness matrix and the geometric properties of each element, performed by integration of the product of transpose of strain matrix $[G]^T$, elasticity matrix [E], and strain matrix [G]. During the volume integration given in Equation 2.01, normalized coordinates $\xi = \frac{x}{w}, \eta = \frac{y}{h}$ are to be considered dependent on x and y, respectively.

$$[k] = \int_V [G]^T [E][G] dV = \int_V [G]^T [E][G] dxdydz \tag{2.13}$$

The integral Equation 2.01 is used to calculate the 8×8 local stiffness matrix [k] for each model element. Using the equations above, the 8×8 local stiffness matrix for each element can be calculated as the matrix defined in Equation 2.02.

$$[k] = \begin{bmatrix} k_{11} & k_{21} & k_{31} & k_{41} & k_{51} & k_{61} & k_{71} & k_{81} \\ k_{21} & k_{11} & k_{41} & k_{31} & k_{71} & k_{81} & k_{51} & k_{61} \\ k_{31} & k_{41} & k_{11} & k_{21} & k_{61} & k_{51} & k_{81} & k_{71} \\ k_{41} & k_{31} & k_{21} & k_{11} & k_{81} & k_{71} & k_{61} & k_{51} \\ k_{51} & k_{71} & k_{61} & k_{81} & k_{55} & k_{65} & k_{75} & k_{85} \\ k_{61} & k_{81} & k_{51} & k_{71} & k_{65} & k_{55} & k_{85} & k_{65} \\ k_{71} & k_{51} & k_{81} & k_{61} & k_{75} & k_{85} & k_{55} & k_{65} \\ k_{81} & k_{61} & k_{71} & k_{51} & k_{85} & k_{75} & k_{65} & k_{55} \end{bmatrix} \tag{2.14}$$

The local stiffness matrix [k] of each model element is axially symmetrical. The next step is the assembly of these local stiffness matrices to generate the global stiffness matrix for the wall model.

2.4.2. Finite Element Model Stiffness Assembly

As indicated in Figure 2.13, the rectangular wall model is divided into model elements that are numbered for the assembly operation at first.

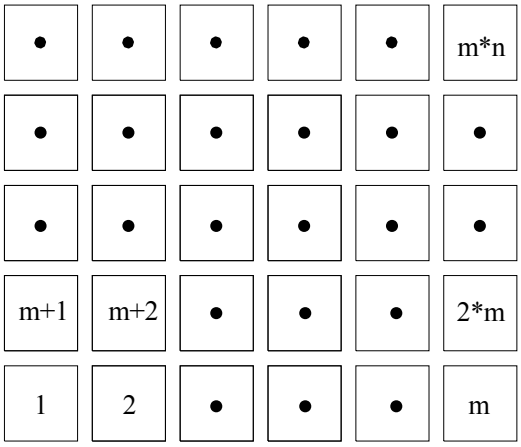

Figure 2.13. Numbering technique used for the FEM of a rectangular wall.

Then, the overlapping terms of the 8×8 local stiffness matrices are superimposed with each other for generating the global stiffness matrix. In the illustrated wall model with four elements, the global DOFs of the wall model are first numbered (Figure 2.14). These define the order of the terms in the global displacement vector and global stiffness matrix.

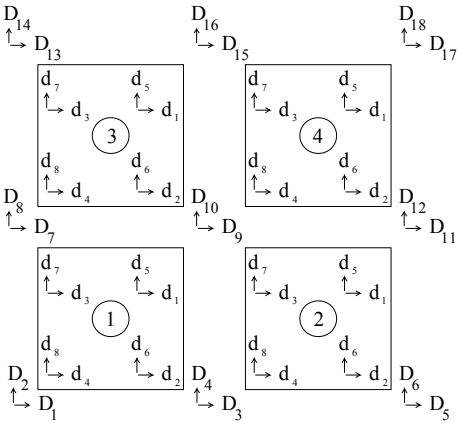

Figure 2.14. Global and local DOFs for a wall model.

Local DOF numbers are displayed inside the model elements whereas global DOF numbers outside the elements. Global stiffness matrix of this sample model is calculated by superimposing the local stiffness terms at overlapping locations within the global stiffness matrix.

Each term in the global stiffness matrix of the wall model is calculated by the same procedure. As this sample includes 18 global DOFs, the resulting global stiffness matrix will be an 18×18 matrix.

2.4.3. Internal Force Vector Assembly

This section further explains the assembly procedure for the local internal force vectors, in order to obtain the global internal force vector. With the average strain values known, the average stresses in each element are calculated with the constitutive Fixed Strut Angle Panel Model, and these stress values multiplied with thickness and half of vertical or horizontal width and superimposed are used to obtain the internal force vector for each element.

The numbering of the internal force vector components as illustrated in Figure 2.15 and the obtained stress values are used in combination to calculate the terms of the internal force vector for each model element.

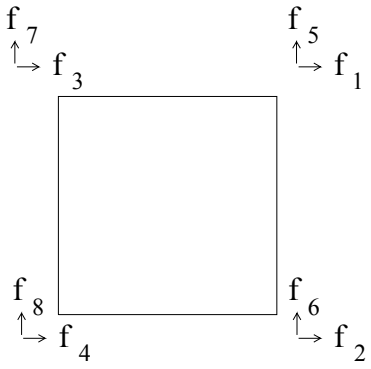

Figure 2.15. Numbering of internal force terms for a model element (Gullu, 2013).

At the next step, the local internal force vectors are superimposed and therefore the global internal force vector for the wall model is obtained.

For the assembly operation, the global internal force vector of the wall model subdivided into four model elements calculated by superimposing the local internal force vector terms at overlapping locations within the global force vector.

After numeration of each mesh as per the example in Figure 2.15, the intersection of 8 x 1 local internal force vectors with each other is superimposed for generating the global internal force vector.

The global DOFs of the wall model define the order of the terms in the global force vector for the wall model. Local and global DOF numbers are displayed inside and outside the model elements respectively. Equation 2.15 is an example for calculation of one of the terms in the global internal force vector where superscripts indicate the model element numbers while subscripts the local internal force vector index for each model element.

$$\{F\}_{91} = \{f\}^{1}_{11} + \{f\}^{2}_{31} + \{f\}^{3}_{21} + \{f\}^{4}_{41} \tag{2.15}$$

Each term in the global internal force vector is calculated by the same procedure. As 18 global DOFs exist for this sample, the global internal force vector will be an 18×1 vector.

2.4.4. Support Conditions and Constraints

At the supports of a wall, displacement values are assumed to be zero. This implies zero displacement along the DOFs of the model at the supports. The reaction forces at the supports are calculated from the equilibrium equation, using the known (zero) displacement values along the DOFs at the supports.

In addition, enforcement of constraint conditions along selected DOFs would be necessary in order to simulate the test conditions for which the wall model was experimentally validated. In this study, the wall specimens used for experimental validation of the model were cast monolithically with stiff RC load-transfer-beams, which behaved like rigid bodies during testing. Therefore, a body constraint was defined along the top DOFs of the FEM of the wall (Figure 2.16).

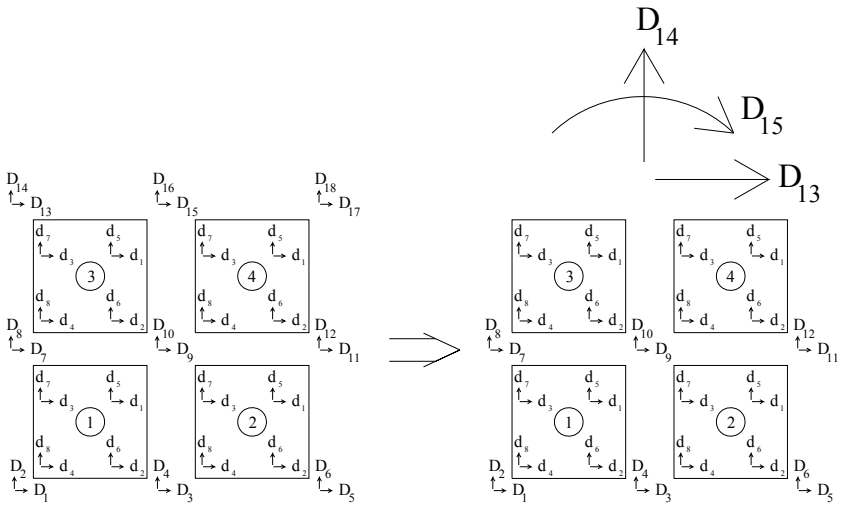

Figure 2.16. Conversion of DOFs after the assignment of body constraint (Gullu, 2013).

The aim of implementing the body constraint in the model is representation of rigid load-transfer-beams located at the top of RC wall specimens. Body constraint is implemented in the model formulation using a displacement transformation matrix [T]. The body constraint condition enforces equal horizontal displacement in the horizontal direction while relating vertical displacements to a global rotational displacement at the top of the wall through the plane-sections-remain-plane condition. The transformation matrix

is a matrix that transforms a 18x18 stiffness matrix to a 15x15 stiffness matrix. Derivation of the global stiffness matrix, the global internal force vector, and the displacement vector of the sample wall after assignment of the body constraint are illustrated in Equations 2.16 to 2.18. Equation 2.19 gives the result of the production of the transpose of the transformation matrix [T] with both sides of Equation 2.16. It should be noticed that more model elements are usually required for a reliable model assembly.

$$[K]_{18x18} \times \{D\}_{18x1} = \{F_{unb}\}_{18x1} \tag{2.16}$$

$$[K]_{18x18} \times [T]_{18x15} \times \{D\}_{15x1} = \{F_{unb}\}_{18x1} \tag{2.17}$$

$$[T]^{T}_{18x15} \times [K]_{18x18} \times [T]_{18x15} \times \{D\}_{15x1} = [T]^{T}_{18x15} \times \{F_{unb}\}_{18x1} \tag{2.18}$$

$$\begin{array}{llll} [T]^{T}_{18x15} \times [K]_{18x18} \times [T]_{18x15} \times \{D\}_{15x1} & = & [T]^{T}_{18x15} \times \{F_{unb}\}_{18x1} \\ \Downarrow & & \Downarrow \\ [K]_{15x15} \qquad\qquad \times \{D\}_{15x1} & = & \{F_{unb}\}_{15x1} \end{array} \tag{2.19}$$

2.4.5. Nonlinear Analysis Solution Strategy

The global stiffness matrix and the internal force vector for the wall model were derived as described in the previous sections, by integration and stiffness assembly of the model elements. In addition to this, support conditions and constraints were implemented in the model formulation. Then, a displacement-controlled nonlinear analysis solution strategy (Clarke and Hancock, 1990; Simons and Powell, 1982) was adopted for conducting displacement-controlled hysteretic lateral load analysis of RC walls so that model results could be correlated with results of drift-controlled lateral load tests conducted on wall specimens.

The applied strategy consists of two main stages; load incrementation and equilibrium stages. During the increment stage (denoted by "*i*"), the target displacements imposed on the model are incremented, whereas during the equilibrium stage (denoted by

"*j*"), iterations are performed on the model displacements, in order to reach equilibrium. During the load incrementation stage, the target displacements imposed on the model are incremented, whereas during the equilibrium stage, iterations are performed on the model displacements, in order to reach equilibrium between the internal and external forces, within a specified tolerance. The adopted nonlinear analysis solution strategy, details of which are presented by Gullu (2013), is graphically illustrated in Figure 2.17 and Figure 2.18.

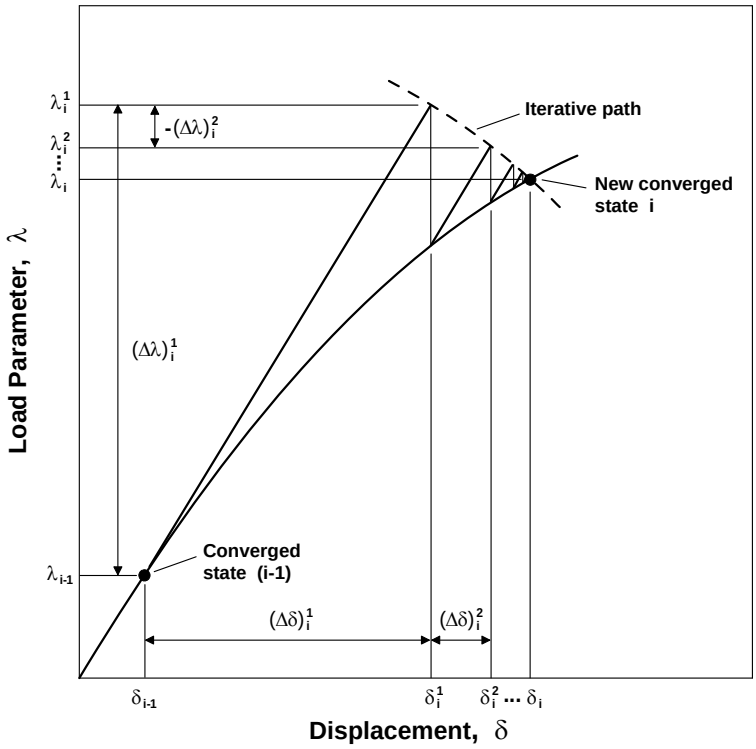

Figure 2.17. Representation of the nonlinear analysis solution strategy for a single degree of freedom system (Clarke and Hancock, 1990).

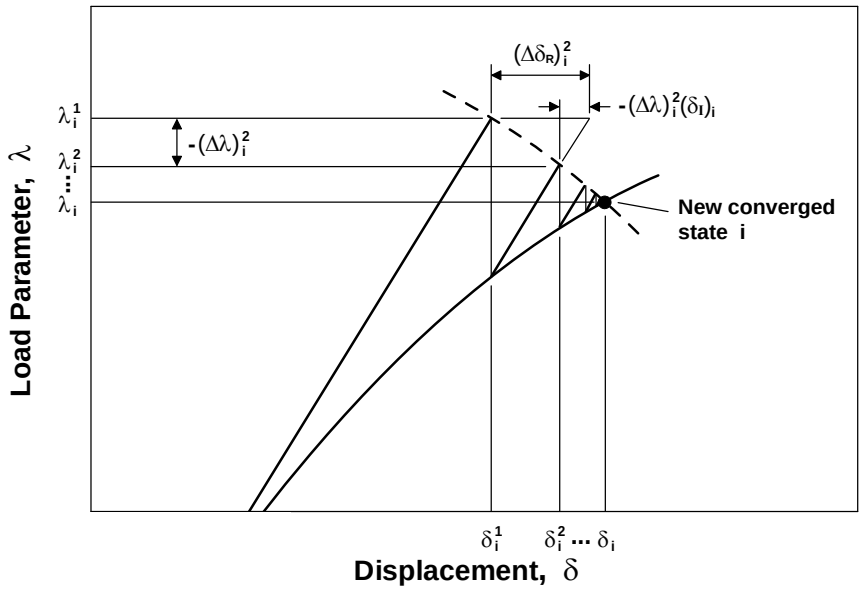

Figure 2.18. Iterative strategy and residual displacements (Clarke and Hancock, 1990).

3. EXPERIMENTAL CALIBRATION OF THE MODEL

The finite element model formulation, together with the constitutive material and behavioral models described in the previous Chapter, were implemented in Matlab for conducting nonlinear analysis and simulating the hysteretic lateral load behavior of squat wall specimens tested by Terzioglu (2011) at Bogazici University Structural Engineering Laboratory. This chapter provides a description of the experimental program and presents information on experimental calibration of the wall model to represent the characteristics of the wall specimens and the loading conditions.

3.1. Description of the Wall Specimens

For the experimental study, three sets of specimens with a total number of eleven squat wall specimens were tested. All of the specimens were expected to experience shear-controlled responses, due to their relatively low aspect ratio. Specimens were differentiated from each other by reinforcement ratio, aspect ratio, amount of boundary reinforcement, material properties of steel and compressive strength of concrete. The specimens having the same aspect ratio, same horizontal and vertical web reinforcement ratios and same boundary reinforcement ratio were considered as being of the same type. If any of these three properties would change, the type of the specimen would change. The naming scheme used for the wall specimens is shown in Figure 3.1.

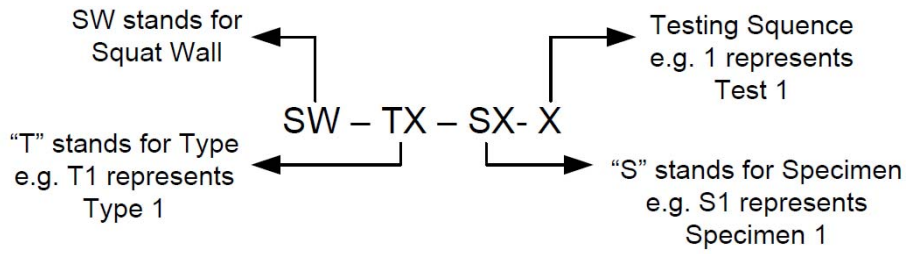

Figure 3.1. Naming of the wall specimens.

The dimensions and reinforcement ratios of the specimens are provided in Table 3.1. The steel reinforcement ratios were calculated as the total steel area divided by the tributary area of concrete. For the boundary reinforcement, the tributary area was defined as the thickness of the wall multiplied by the length of the boundary region. The only diversity of the specimens SW-T2-S1-1 and SW-T2-S2-3 was the horizontal reinforcement anchorage conditions. Specimen SW-T2-S1-1 had U-cap hooks at the ends of the horizontal reinforcement bars, whereas SW-T2-S2-3 had 180° hook on the horizontal bars. All other specimens also had 180° hooks on the horizontal bars. The details of the hooks that are used in specimens are shown in Figure 3.2. Specimen Type1-S1 had no confinement, whereas Type1-S2 was confined with ties in order to observe the difference in the response in terms of shear strength and ductility.

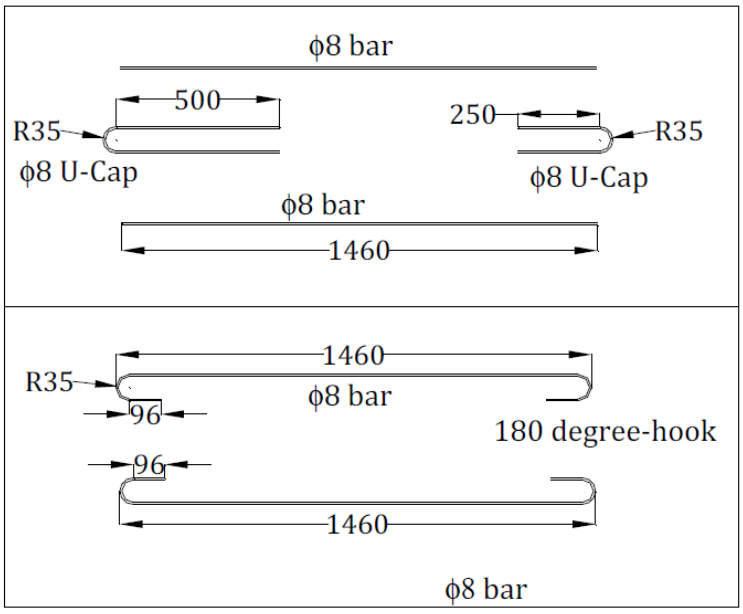

Figure 3.2. Hook type.

Table 3.1. Reinforcement ratios.

Specimen	I_w (cm)	h_w (cm)	Horizontal		Vertical		Boundary	
			Reinf. Bars	ρ_t (%)	Reinf. Bars	ρ_l (%)	Reinf. Bars	ρ_b (%)
SW-T2-S1-1	150	75	ϕ8@125 mm	0.68	ϕ8@125 mm	0.68	4ϕ16	5.15
SW-T1-S1-2	150	75	ϕ8@125 mm	0.34	ϕ8@250 mm	0.34	4ϕ16	5.15
SW-T2-S2-3	150	75	ϕ8@125 mm	0.68	ϕ8@125 mm	0.68	4ϕ16	5.15
SW-T2-S3-4	150	75	ϕ8@125 mm	0.68	ϕ8@125 mm	0.68	4ϕ16	5.15
SW-T3-S1-5	150	75	ϕ8@125 mm	0.68	ϕ8@125 mm	0.68	2ϕ8	0.65
SW-T4-S1-6	150	50	ϕ8@125 mm	0.68	ϕ8@125 mm	0.68	4ϕ14	3.95
SW-T5-S1-7	150	150	ϕ8@125 mm	0.68	ϕ8@250 mm	0.34	4ϕ22	9.75
SW-T6-S1-8	150	150	ϕ8@250 mm	0.34	ϕ8@250 mm	0.68	4ϕ22	9.75
SW-T1-S2-9	150	75	ϕ8@250 mm	0.34	ϕ8@250 mm	0.34	4ϕ16	5.15
SW-T1-N5-S1-10	150	75	ϕ8@250 mm	0.34	ϕ8@250 mm	0.34	4ϕ16	5.15
SW-T1-N10-S1-11	150	75	ϕ8@250 mm	0.34	ϕ8@250 mm	0.34	4ϕ16	5.15

Note: l_w: length of the wall, h_w: height of the wall, ρ_t: transverse reinforcement ratio, ρ_l: longitudinal reinforcement ratio, ρ_b: boundary reinforcement ratio, thickness of the wall is 12 cm for all specimens.

Specimen SW-T2-S3-4 was constructed identically same with SW-T2-S2-3 because defects were observed in the placement of the concrete during casting of Specimen SW-T2-S2-3. The specimens SW-T1-N5-S1-10 and SW-T1-N10-S1-11 were tested under different load levels. The abbreviations N5 and N10 represent the axial load level that was applied to the specimen. Representative geometric characteristics and reinforcement details are shown in Figure 3.3 for specimen T1-S1.

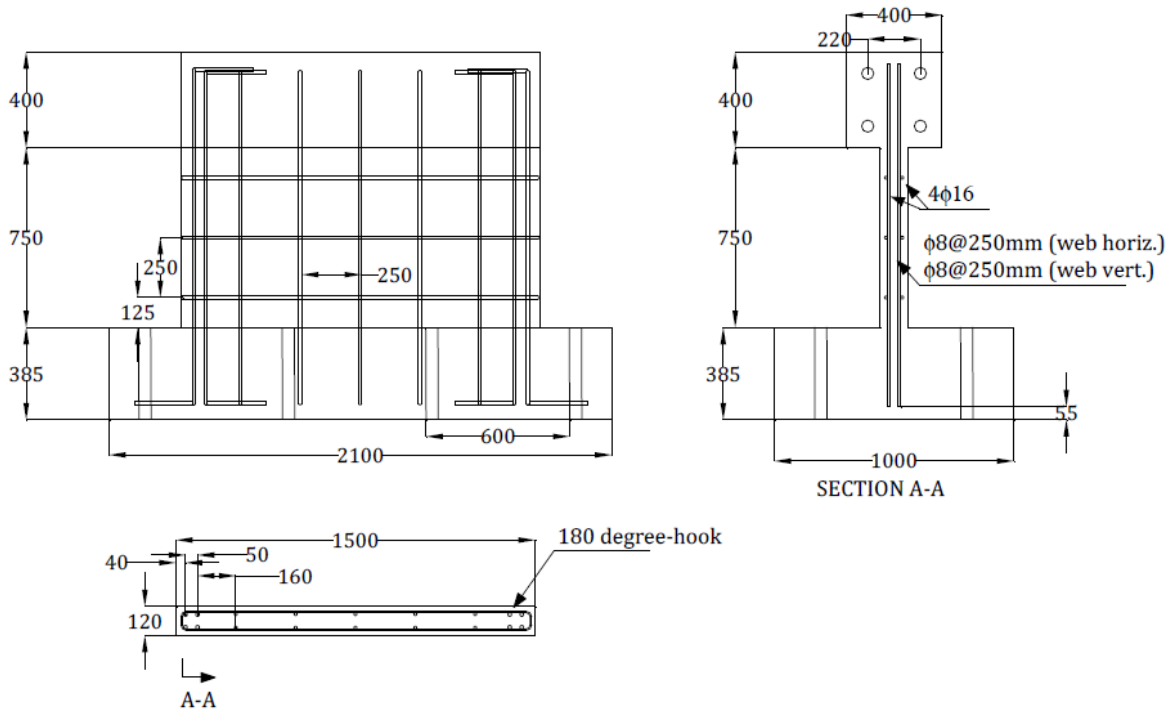

Figure 3.3. Geometry and reinforcement of specimen T1–S1 (Terzioglu, 2011).

The boundary region length presented in the table corresponds to the length of one boundary only, and it is defined as the summation of the center-to-center distances between the boundary reinforcing bars, and twice the concrete cover to bar center. Differentiation between boundary and web regions, which is important for geometric calibration of the model, is demonstrated in Figure 3.4.

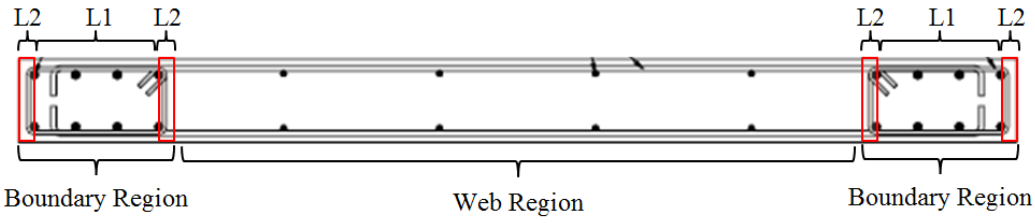

L1: The Length between Boundary Reinforcing Bars

L2: The Length of Clear Cover

Figure 3.4. Cross section of a specimen: Definition of boundary and web regions.

The length (width) of all wall specimens was 150 cm. Due to different amounts of boundary reinforcement, lenght of the boundary region differed among some of the specimens. The length of the boundary region and the remaining web length for the specimens are listed in Table 3.2.

Table 3.2. Dimensions of the wall specimens.

Specimen	Boundary Length (cm)	Total Web Length (cm)	Total Specimen Length (cm)
SW-T2-S1-1	13.0	124.0	150.0
SW-T1-S1-2	13.0	124.0	150.0
SW-T2-S2-3	13.0	124.0	150.0
SW-T2-S3-4	13.0	124.0	150.0
SW-T3-S1-5	22.8	104.4	150.0
SW-T4-S1-6	13.0	124.0	150.0
SW-T5-S1-7	13.0	124.0	150.0
SW-T6-S1-8	13.0	124.0	150.0
SW-T1-S2-9	29.0	92.0	150.0
SW-T1-N5-S1-10	13.0	124.0	150.0
SW-T1-N10-S1-11	13.0	124.0	150.0

The material properties were chosen to represent general material quality for new construction in Turkey and Chile. The concrete was chosen to have 25 MPa compressive strength, whereas the reinforcing bars were chosen to have 420 MPa characteristic yield stress. The materials were were tested in the laboratory in order to determine their actual mechanical properties. 600 mm length steel coupon samples were tested in order to determine their actual yield and tensile strength. In the first set of experiments, specimens were constructed with bars that had two different diameters, ϕ8 and ϕ16. The tensile stress-stress relationships that were obtained from the results of the reinforcing bar tension tests for the first set of specimens are illustrated in Figure 3.5.

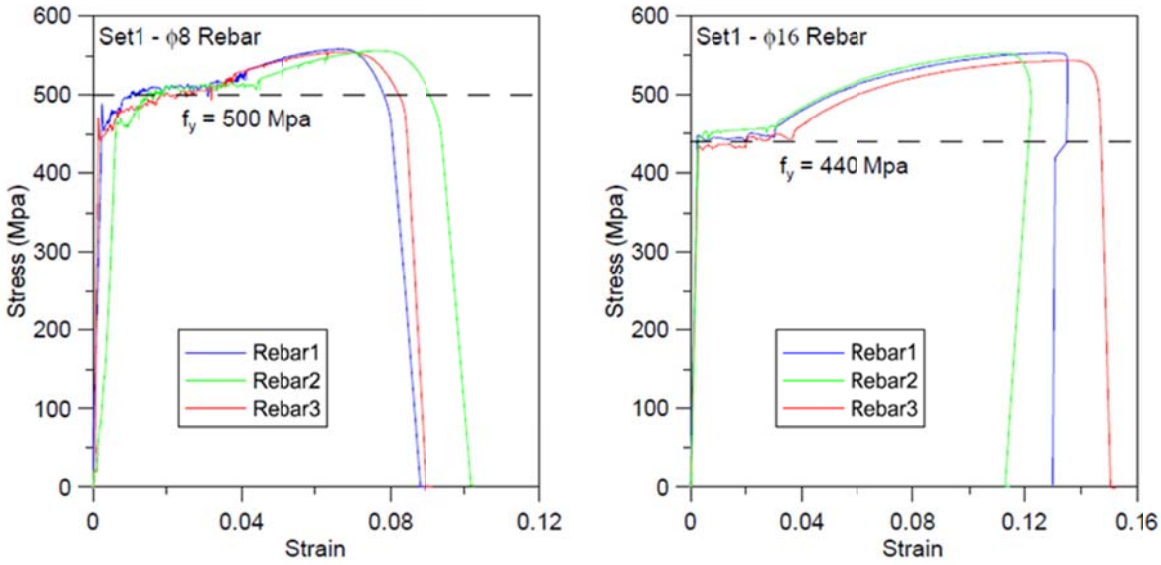

Figure 3.5. Stress-Strain curves of steel, for specimen set 1 (Terzioglu, 2011).

For the second and the third set of specimens, four different diameters of reinforcing steel bars were used: ϕ8, ϕ14, ϕ16 and ϕ22. The tension test results obtained for the second and the third sets of specimens are provided in Figure 3.6 and Figure 3.7, respectively.

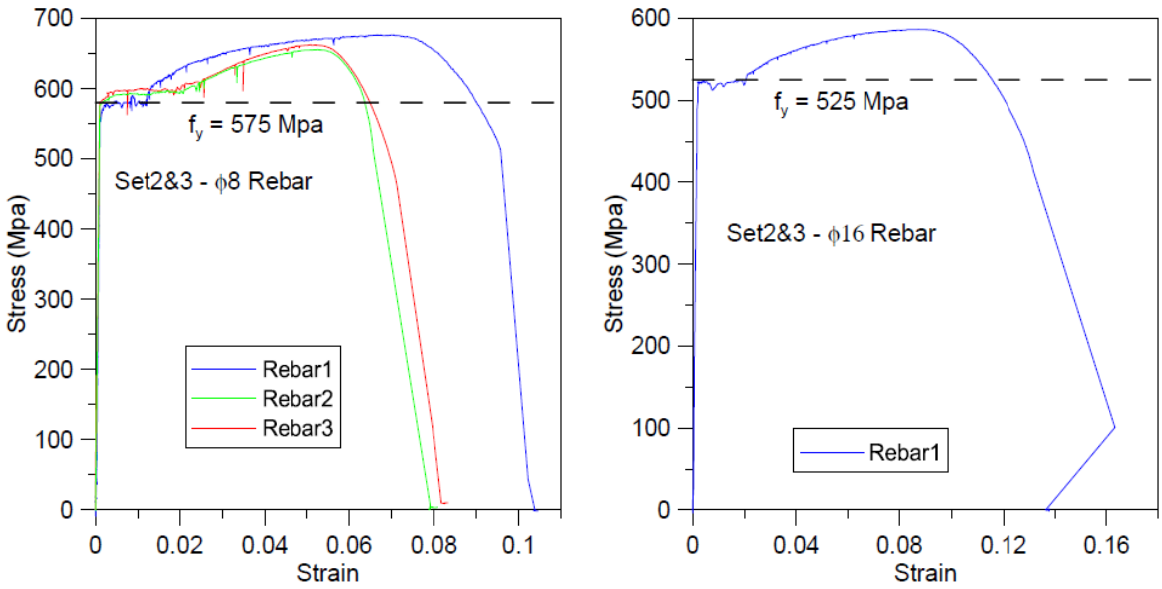

Figure 3.6. Stress-Strain curves of steel, for specimen set 2 and set 3 (Terzioglu, 2011).

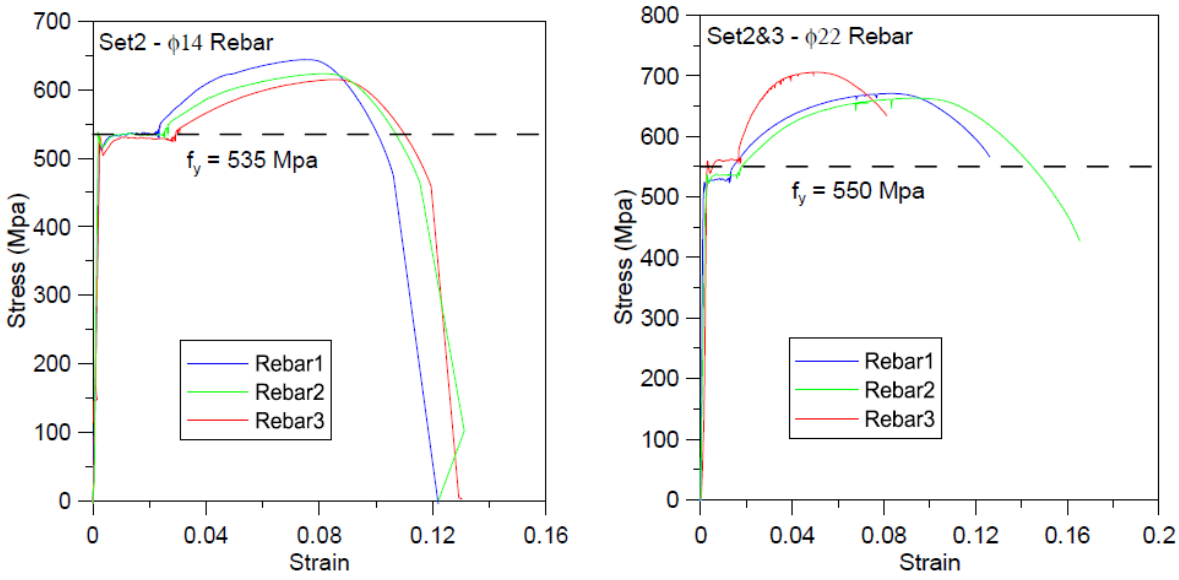

Figure 3.7. Stress-Strain curves of steel, for specimen set 2 and set 3 (Terzioglu, 2011).

The real values of yield strength of the bars were obrained from these test results.. On the other hand, the ultimate strength and ultimate strain values were used to derive approximate strain hardening ratios, which are necessary for calibration of the wall models. Based on the stress and strain diagrams obtained, the average strain hardening (*b*) values listed in Table 3.3 were obtained for bare reinforcing bars.

Table 3.3. Material properties of reinforcing steel.

Set / Rebar	**f_y (MPa)**	**f_{ult} (MPa)**	**ε_y**	**ε_{ult}**	**b**
Set 1 - ϕ8 Rebar	500	550	0.00250	0.080	0.003226
Set 1 - ϕ16 Rebar	440	550	0.00220	0.130	0.004304
Set 2&3 - ϕ8 Rebar	575	660	0.00288	0.055	0.008153
Set 2&3 - ϕ14 Rebar	535	600	0.00268	0.085	0.003948
Set 2&3 - ϕ16 Rebar	525	580	0.00263	0.100	0.002824
Set 2&3 - ϕ22 Rebar	550	650	0.00275	0.080	0.006472

The target compressive strength of concrete was 25 MPa for all specimens. The actual values, obtained from testing of standart cylinders on wall test dates, were

determined as ranging between 20 MPa – 35 MPa. One reason why concrete had different test-date cylinder compressive strengths was different dates of testing. Since the specimens were heavily reinforced, the maximum size of the aggregate was chosen to be 10 mm. Plasticizers were added to the concrete mix in order to improve workability. For each wall specimen, 3 standard cylinders in the size 150 x 300 mm were tested at the test date. The average compressive strengths of the specimens are shown in the Table 3.4.

Table 3.4. Concrete compressive strength.

Specimen	**f_c' (Mpa)**
SW-T2-S1-1	19.3
SW-T1-S1-2	23.7
SW-T2-S2-3	25.8
SW-T2-S3-4	29.0
SW-T3-S1-5	32.1
SW-T4-S1-6	34.8
SW-T5-S1-7	35.0
SW-T6-S1-8	22.6
SW-T1-S2-9	24.0
SW-T1-N5-S1-10	26.3
SW-T1-N10-S1-11	27.0

During the experimental program, three sets of specimens were constructed. The first set consisted of three specimens constructed in June 2009. SW-T1-S1-2 and SW-T2-S1-1 and SW-T2-S2-3 were specimens in the first set. The second set included four specimens constructed in June 2010, SW-T2-S3-4, SW-T3-S1-5, SW-T4-S1-6 and SW-T5-S1-7. For specimen SW-T2-S2-3 (first set), there were some defects during the placement of the concrete. Because of this, specimen SW-T2-S3-4 is constructed identically same with SW-T2-S2-3. The third set consisting of four specimens was constructed in May 2011. SW-T6-S1-8 differed from SW-T5-S1-7 in its vertical reinforcement ratio. The other three specimens in the third set were identical to Type 1, two of which were tested under axial load. All concrete casting was done with the wall specimens standing in an upright

position. All specimens incorporated a RC pedestal at the bottom for connection of the specimen to the laboratory strong floor, and a RC load transfer beam at the top for connection of the specimen to the loading actuator. All specimens in the first two sets of tests were cast at one time to avoid cold joints between bottom pedestal and wall. However, due to construction and concrete placement difficulties, concrete was casted in two steps for the third set of specimens. Representative pictures of a wall specimen with an aspect ratio of 0.5 is illustrated in Figure 3.8.



Figure 3.8. Formwork and reinforcement of a wall specimen (Terzioglu, 2011).

3.2. Test Setup and Instrumentation

The specimens were placed onto 2-cm thick plaster because of the rough surfaces of the floor and the pedestal. This precaution prevented a possible cracking and sliding of the pedestal during the test. Lateral loading on the specimens was applied by a 1000 kN capacity actuator, one end of it fixed to a steel reaction wall. A sketch of the test setup is shown in Figure 3.9. Two specimens were tested at $5\%A_g f_c'$ and $10\%A_g f_c'$ axial load levels, in which four pre-stressed steel cables with 250 kN axial tension capacities were connected to the bottom of pedestals by special steel hinges and to a loading assembly located at the top of the load transfer beam, incorporating a hydraulic cylinder used for applying the axial load.

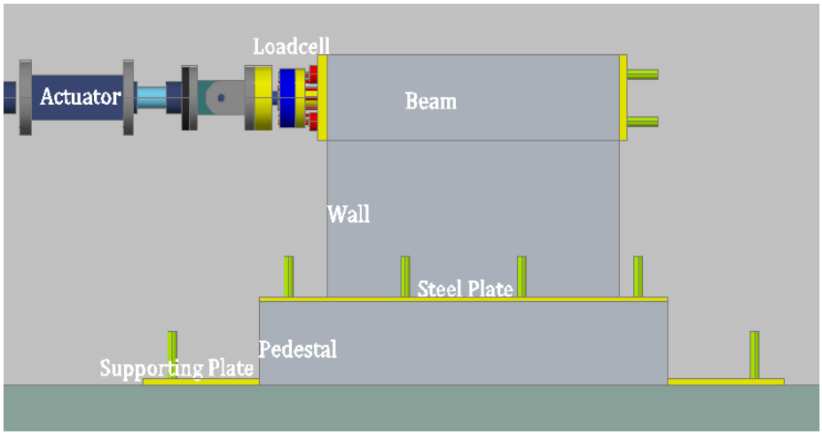

Figure 3.9. Test setup (Terzioglu, 2011).

At high lateral load, levels, it was almost inevitable to have out-of-plane movements caused by the asymmetry in specimen geometry or accidental eccentricity effects. Four out of plane frames made of triangular-shaped steel were used to prevent any possible out-of-plane movements. They supported the specimens' load transfer beams in the transverse direction, allowing in-plane motion. Greased steel plates were placed on the surface of the load transfer beam, contacting with the out of plane frames through roller supports, in order to minimize their resistance to applied lateral load.

The main components of the test equipment included the hydraulic loading system, data acquisition system, control software, linear variable differential transducers (LVDT) and strain gauges. An actuator with the capacity of 1000 kN generated the pressure for lateral loads during tests. The actuator was equipped with an externally calibrated CAS 100-TF tension-compression load cell to measure the lateral loads applied. Also, a servo valve was installed for controlling the actuator accurately. The top lateral displacement of the specimens was controlled during loading, by means of two externally-mounted LVDTs connected to the bottom of each load transfer beam . The stroke capacity of the actuator was 300 mm (150 mm in tension and 150 mm in compression).

For measuring the average concrete strains and steel strains, strain gauges and DC excited linear variable differential transducers (DC-LVDT or DCDT) were installed on the wall specimens. On each specimen, thirteen strain gauges were installed to collect steel strain data and monitor if there is yielding on the reinforcing bars. Three strain gauges

were mounted on the reinforcing bar at the exterior boundary on each side. Four gauges were mounted along the wall-pedestal interface. Finally, three gauges were placed to horizontal reinforcing bars, distributed along the wall height. Figure 3.10 shows typical strain gauge positions on the wall specimens. The gauges on the horizontal web bars served for measuring the strains on the horizontal web reinforcement. The ones along the wall-pedestal interface, placed on vertical bars, enabled to observe if there is yielding in the vertical reinforcement (web and boundary), due to flexural deformation. The strain gauges on the boundary reinforcement within the pedestal allowed monitoring of strain penetration effects.

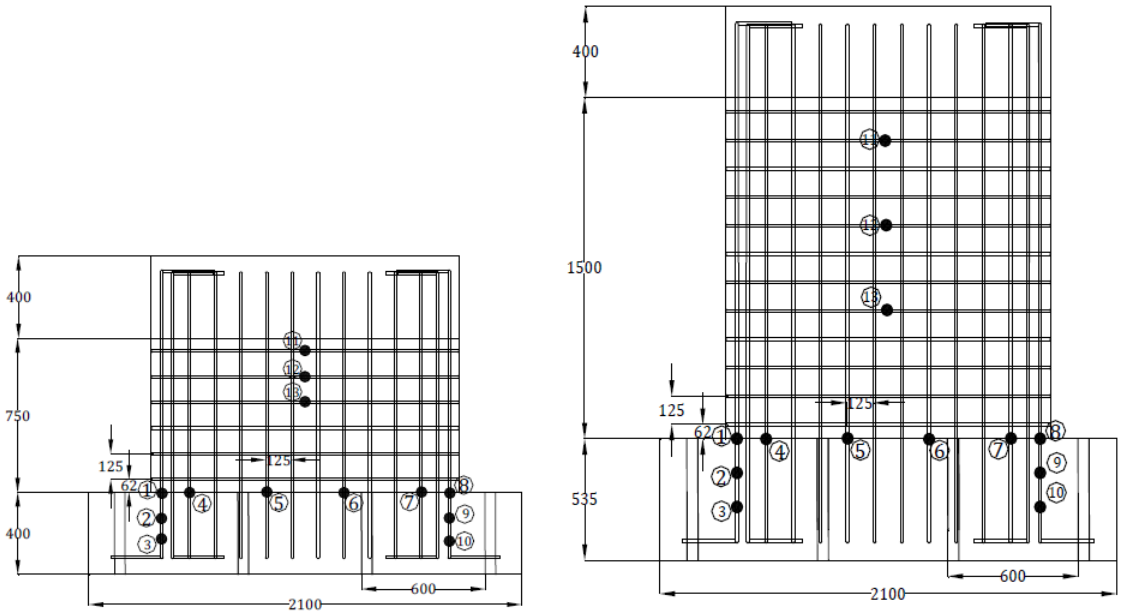

Figure 3.10. Strain gauge positions (Terzioglu, 2011).

The external instrumentation on specimens was performed by using LVDTs deployed in three groups. The first groud of LVDTs were used for measuring average shear deformations on specimens. Two spring-loaded and wire-mounted LVDTs were installed diagonally on the wall and two other were installed diagonally from pedestal to beam. The ones mounted on the wall were removed after typical crushing of the concrete at the base and corners. The second group consisted of vertical spring-loaded and wire-mounted LVDTs installed on the wall, from bottom pedestal to top beam, which were used for measuring flexural deformations. The third group of LVDTs was used for measuring horizontal strain distributions along the wall height. For walls with 0.5 and 0.33 aspect

ratios, five LVDTs and for walls with 1.0 aspect ratio, nine LVDTs were placed along the wall height. These LVDTs had stroke capacities of +/- 25, 50 and 75 mm. The capacity was chosen according to the expected level of deformation at any selected location. Two LVDTs were used to measure the top displacement of specimens relative to the bottom pedestal and in order to measure the correct displacement of the wall with respect to the pedestal, in case of an unexpected sliding at the pedestal – strong floor interface. Additional horizontal LVDTs were used for measuring sliding shear deformations at the wall-pedestal interface.



Figure 3.11. Vertical and horizontal LVDTs (Terzioglu, 2011).

Figure 3.11 shows horizontal and vertical LVDTs mounted on the wall specimen. The representative schemes in Figure 3.12 indicate LVDT locations on a specimen with 0.5 aspect ratio. A representative wire-mounted and spring-loaded assembly used on a diagonally-mounted LVDT is shown in Figure 3.16. All LVDTs were attached to mounting devices made of hard plastics, with holes at the corners for the spring connection.

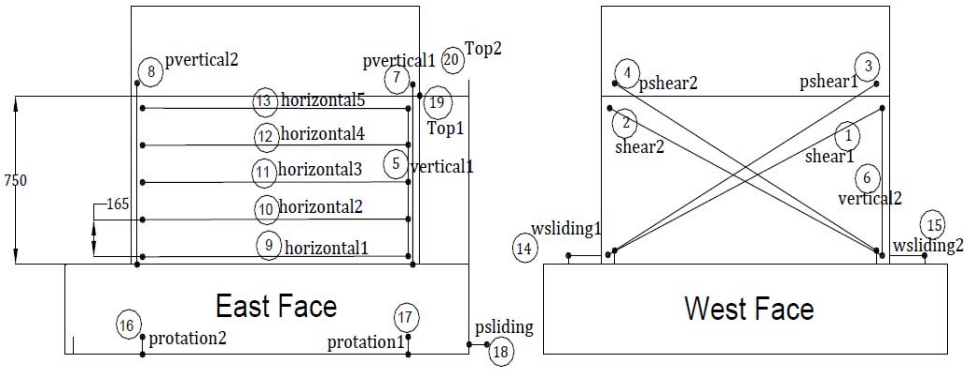

Figure 3.12. LVDT locations – 0.5 Aspect ratio walls (Terzioglu, 2011).



Figure 3.13. LVDT spring – loaded and mounting assembly (Terzioglu, 2011).

3.3. Loading Protocol and Observed Failure Modes

Reversed cyclic lateral loading was applied at the top of each specimen, resulting in a single curvature (cantilever) loading condition. Three full cycles were applied at each drift level of 0.05%, 0.1%, 0.15%, 0.2%, 0.3%, 0.4%, 0.6%, 0.8%, 1.0%, 1.2%, 1.4%, 1.6%, 1.8%, 2.0%, 2.4%, and 3.2%. Depending on their residual lateral load capacity, one or two more drift levels were imposed on selected specimens. The test specimens were investigated in terms of experimentally-observed behavior and damage characteristics. Experimental observations are discussed for three typical failure modes observed during testing of the specimens; including diagonal tension failure, diagonal compression failure,

and sliding shear failure. The failure modes observed for the individual wall specimens are listed in Table 3.11. A summary of the general behavior and failure modes of the wall specimens is provided in the following paragraphs, whereas detailed information on the test observations are available in the M.S. Thesis by Terzioglu (2011).

Type 1 (T1) specimens had 0.34% vertical and horizontal web reinforcement ratios and 4-ϕ16 boundary bars at each boundary. In all cases, the first major diagonal tension cracks form from corner to corner, during the first cycles of the 0.1% drift level, although initial cracking was observed earlier. Specimen T1-S1, presented crushing of the concrete at the bottom corners at 0.8% drift level. At 1% drift level, the maximum lateral load capacity was reached. Transverse (horizontal) reinforcing bars yielded at some point after reaching the ultimate load capacity. Longitudinal boundary reinforcement yielded at the 1.0% drift level, when the capacity was reached. At the 1.2% drift level, strength degradation started and concrete started to crush at the center section of the wall. After the ultimate load level was reached, crushing and spalling of the concrete concentrated at the center. This specimen failed under diagonal tension, similarly to what was observed for all Type 1 specimens. The main diagonal cracks opened and closed at every cycle, and eventually the crushing of concrete propagated along the diagonal tension and compression struts, indicating a general diagonal tension type of squat wall failure.

Type 2 (T2) specimens had 0.68% vertical and horizontal web reinforcement ratios and had 4-ϕ16 longitudinal reinforcement at each boundary. For these specimens, the first main diagonal cracks formed at the 0.1% drift level at both positive and negative loading directions. At higher drift levels, the crack formation concentrated on the previously uncracked regions. As well, the existing cracks continued to open and close at each cycle, and the main cracks extended from bottom pedestal to top pedestal. The lateral load capacity was reached close to 1% to 1.2% drift level. At this drift level, concrete started to crush at the bottom corners of the specimen. It was seen that at the ultimate load level, the main diagonal tension cracks close to the center of the specimen did not crush. For Type 2 specimens, although the diagonal tension cracks formed, they did not substantially widen, and the failure mode resembled a diagonal compression failure, under combined shear and flexure effects, since the large amount of transverse reinforcement prevented the widening of the main diagonal cracks and crushing along diagonal compression struts between the

cracks. Crushing was first observed at the bottom corners of the wall, where the first inclined cracks were formed. After the crushing of the corner regions, the effective shear area that resists shear sliding was reduced. The crushing of the concrete then propagated inwards, along the wall-pedestal interface, while the lateral capacity maintained an almost constant residual strength of about 10% of the peak capacity. Eventually, the entire base of the wall crushed, and the crushing extended upwards towards the center of the wall.

Other three types of specimens (T4, T5 and T6), for which the common parameter was the horizontal web reinforcement (0.68%), also experienced diagonal compression failure. The Type 4 (T4-S1) specimen had 1/3 aspect ratio, which differentiated it from the rest. The crack formation and alignment were similar to the Type 2 specimens. Type 5 and 6 specimens were the most slender (aspect ratio of 1.0) specimens tested in this experimental program. After initiation of cracking, at 0.4% drift, diagonal cracks at the corners extended towards the center and became horizontal, such that they continued as flexural joint cracks at the wall-pedestal interface. The diagonal tension cracks were prevented from widening, by the significant amount of horizontal web reinforcement (0.68%). Although at the ultimate load level, crushing of concrete had initiated at the wall center due to diagonal compression, the bottom corners of the specimen also crushed under flexural compressive stresses. These specimens are believed to fail under a combined shear and flexure failure mode.

Specimen T3-S1 was designed such that it has same web reinforcement amount as Type 2 specimens, but it had only 2–ϕ8 boundary reinforcement at each boundary, which was intentionally kept low in order to observe either flexural yielding or a sliding shear failure mode at the base of the wall. For this specimen, a few initial inclined cracks formed at 0.1% drift. The lateral load capacity was reached at the 0.6% drift level. At this point, the horizontal crack at the wall-pedestal interface had extended along the entire width of the wall, the crack had widened, and the wall started experiencing sliding shear failure along the interface crack. The concrete along the interface crack started to crush at this drift level. For this specimen, the main lateral displacement component was sliding along the wall-pedestal interface.

Table 3.5. Observed failure modes of the specimens.

Specimen	Failure Mode
SW-T2-S1-1	Diagonal Compression
SW-T1-S1-2	Diagonal Tension
SW-T2-S2-3	Diagonal Compression
SW-T2-S3-4	Diagonal Compression
SW-T3-S1-5	Sliding Shear
SW-T4-S1-6	Diagonal Compression
SW-T5-S1-7	Diagonal Compression
SW-T6-S1-8	Diagonal Compression
SW-T1-S2-9	Diagonal Tension
SW-T1-N5-S1-10	Diagonal Tension
SW-T1-N10-S1-11	Diagonal Tension

3.4. Calibration of the Model for the Wall Specimens

The finite element models used for conducting analysis of the wall specimens were calibrated to represent the geometric properties and reinforcement characteristics of the wall specimens. As well, parameters of the constitutive material models implemented in the model formulation were calibrated to represent the as-tested properties of the materials used in the construction of the specimens. Furthermore, necessary calibration studies were conducted to adjust the constitutive material parameters for representation of the shape of the stress-strain curve for concrete in compression, and the stress-strain behavior of concrete in tension and reinforcing steel were calibrated to incorporate tension stiffening effects. All calibration was done according to either as-tested material properties, or based on well-established empirical relationships presented in the literature. None of the constitutive material parameters were adjusted to fit model results with experimental results obtained for the wall specimens. Details on the calibration of the model parameters are presented in this section.

3.4.1. Calibration of Model Element Dimensions and Reinforcement Ratios

Finite element models generated for the wall specimens were divided into an appropriate number of constitutive panel elements (mesh sizes) in order to obtain square-shaped constitutive elements. The dimensions and number of the constitutive model elements (mesh dimension and mesh number) used in generation of the models as shown in Table 3.6. The horizontal dimensions of the model elements at wall boundary regions and wall web were different from each other, whereas the vertical dimensions of the elements were equal. The reinforcement ratios in the boundary and web regions of the walls were calibrated according to the values presented in Table 3.1.

Table 3.6. Model element number and element size used for modeling of the specimens.

Specimen	Model Element Dimension			Model Element Number		
	Horizontal		Vertical	Horizontal		Vertical
	Boundary Region	Web Region	-	Boundary Region	Web Region	-
SW-T2-S1-1	13.0	12.4	12.5	2	10	6
SW-T1-S1-2	13.0	12.4	12.5	2	10	6
SW-T2-S2-3	13.0	12.4	12.5	2	10	6
SW-T2-S3-4	13.0	12.4	12.5	2	10	6
SW-T3-S1-5	11.4	10.4	10.7	4	10	7
SW-T4-S1-6	13.0	12.4	12.5	2	10	4
SW-T5-S1-7	13.0	12.4	12.5	2	10	12
SW-T6-S1-8	13.0	12.4	12.5	2	10	12
SW-T1-S2-9	9.7	9.2	9.4	6	10	8
SW-T1-N5-S1-10	13.0	12.4	12.5	2	10	6
SW-T1-N10-S1-11	13.0	12.4	12.5	2	10	6

3.4.2. Calibration of Constitutive Material Parameters

Parameters of the constitutive material models implemented in the model formulation were calibrated to represent the as-tested properties of the materials used in the construction of the specimens, whenever available. Calibration studies were also conducted

on the concrete constitutive model for representation of the shape of the stress-strain curve for concrete in compression. As well, the stress-strain behavior of concrete in tension and reinforcing steel were calibrated to incorporate tension stiffening effects.

3.4.2.1. Calibration of the Constitutive Model for Reinforcing Steel for Tension Stiffening Effects: Belarbi and Hsu (1994) identified how the average stress-strain relationship of reinforcing steel bars surrounded by concrete differs from the stress-strain relationship of bare bars. The most significant influence is the reduction in the yield stress, due to tension stiffening effects. The behavior of the bare bar and bar in concrete are compared in Figure 3.14.

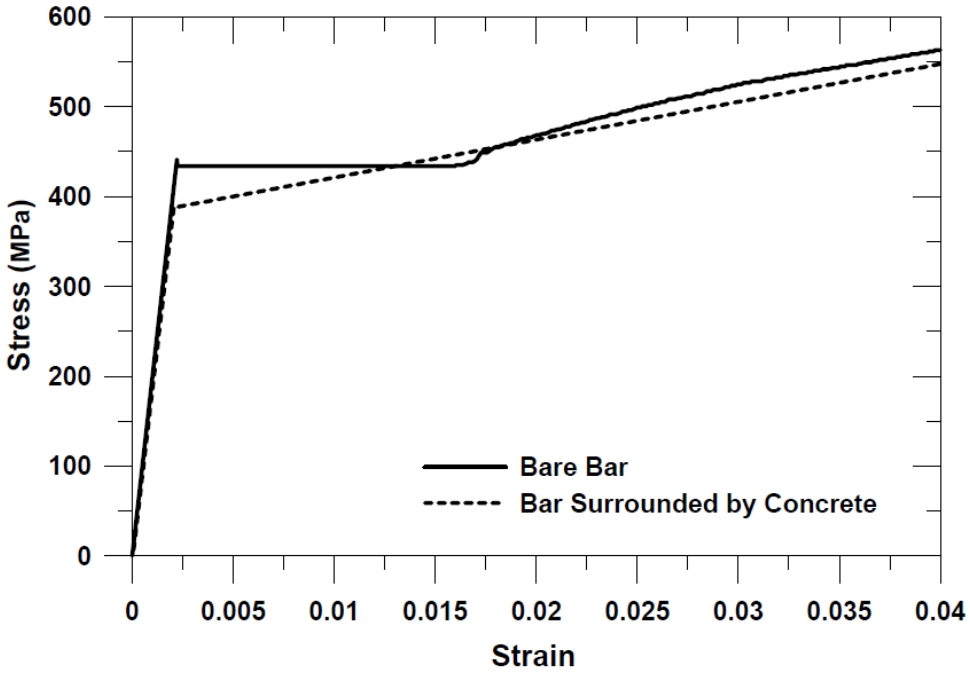

Figure 3.14. Stress-strain behavior of bare rebar and rebar embedded in concrete.

The empirical relationships between the behavior of bare bars and bars embedded in concrete is derived based on experimental results conducted by Belarbi and Hsu (1994) on uniaxially-loaded column specimens. The influence of tension stiffening on the average yield stress of reinforcing steel depends on the cross-sectional area ratio of the longitudinal steel (ρ), and the ratio of concrete tensile strength (f_{cr}) to the yield stress of the bare bar

(σ_y). The strain hardening ratio of the bar in concrete also differs from the strain hardening ratio of a bare bar.

The monotonic stress-strain envelope of bar embedded in concrete is represented by two regions, the first is the elastic region with a slope equal to the elastic modulus of reinforcing steel (E_s), and the second is the post-yield range with a slope E_p^*. (Figure 3.15)

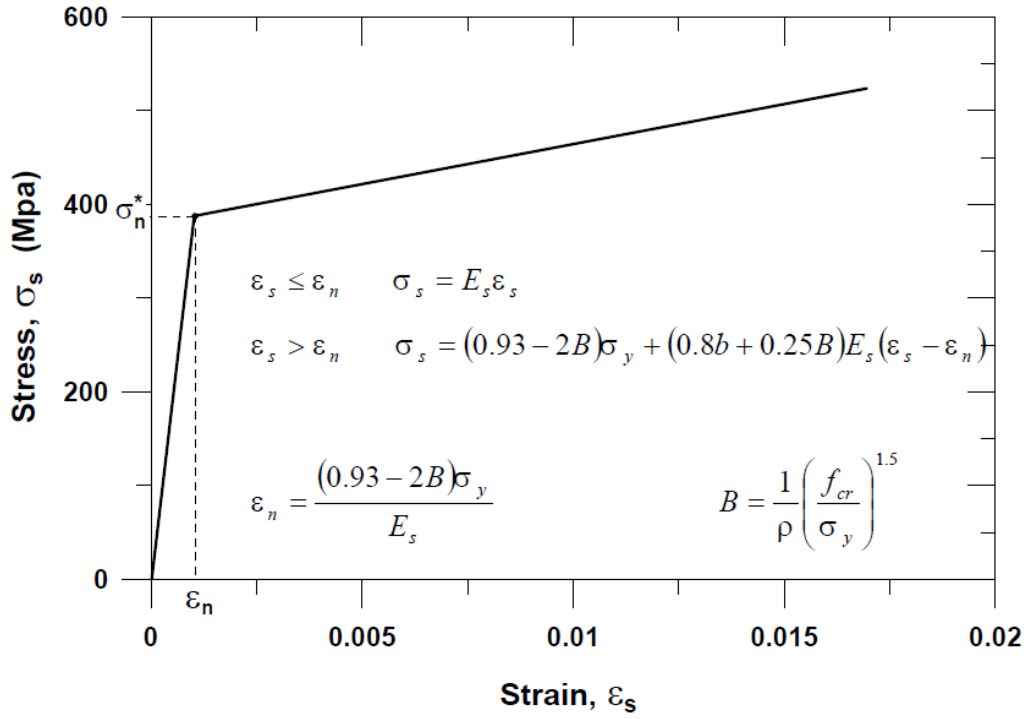

Figure 3.15. Stress-Strain relationship by Belarbi and Hsu (1994) for bar in concrete.

The effective yield stress at the intersection of the two regions (σ_n^*) and the plastic slope (E_p^*) are given by the following expressions:

$$\sigma_n^* = (0.93 - 2B)\sigma_y \tag{3.1}$$

$$E_p^* = (0.8b + 0.25B)E_s \tag{3.2}$$

where *B* is defined as:

$$B = \frac{1}{\rho}\left(\frac{f_{cr}}{\sigma_y}\right)^{1.5} \tag{3.3}$$

and *b* is the strain hardening ratio (E_p / E_s) defined for the bare bar.

Accordingly, the model of Belarbi and Hsu (1994) for modeling the average stress-strain behavior of bars in concrete (Figure 3.15) is defined as:

$$\text{If} \quad \varepsilon_s \le \varepsilon_n, \quad \sigma_s = E_s\varepsilon_s \tag{3.4}$$

$$\text{If} \ \varepsilon_s > \varepsilon_n, \quad \sigma_s = \left(0.93 - 2B\right) + \left(0.8\text{b} + 0.25B\right)E_s(\varepsilon_s - \varepsilon_n) \tag{3.5}$$

where σ_s is the average stress, ε_s the average strain and ε_n the average strain defined at the intersection of the two lines as defined in equation below:

$$\varepsilon_n = \frac{\sigma_n^*}{E_s} = \frac{\left(0.93 - 2B\right)\sigma_y}{E_s} \tag{3.6}$$

E_s , σ_y and *b* are the modulus of elasticity, yield stress, and strain hardening ratio experimentally-measured for bare bars. Accordingly, the calibrated parameters for the reinforcing steel bars in the wall specimens are presented in the following section.

Calibrated Constitutive Parameters for Reinforcing Steel Bars: The calibrated parameters for the reinforcing steel bars in the wall specimens are presented in the following tables,

which include the reinforcement ratios (ρ), the strain hardening slopes (E_p^*), and the stress (σ_n) and strain (ε_n) values at the intersection of the elastic and post-yield regions.

For the first set of specimens, the calibrated values are listed in Table 3.7. There were two different bar diameters, ϕ8 and ϕ16 for these specimens. It must be mentioned that tension stiffening effects influence the constitutive parameters for reinforcing bars in tension only, whereas the parameters for bars in tension are identical to those obtained for bare bar tests.

Table 3.7. Calibrated values of the constitutive parameters of reinforcing steel bars for specimens SW-T2-S1-1, SW-T1-S1-2, and SW-T2-S2-3.

Specimen	Mesh Location	ϕ	ρ	Compression		Tension	
				f_y	b	σ_n*	b'
SW-T2-S1-1	**Boundary Mesh**						
	Horizontal	ϕ8	0.68	500	0.00323	464.89	0.00261
	Vertical	ϕ16	5.15	440	0.00430	409.18	0.00345
	Web Mesh						
	Horizontal	ϕ8	0.68	500	0.00323	464.89	0.00261
	Vertical	ϕ8	0.68	500	0.00323	464.89	0.00261
SW-T1-S1-2	**Boundary Mesh**						
	Horizontal	ϕ8	0.34	500	0.00323	464.70	0.00266
	Vertical	ϕ16	5.15	440	0.00430	409.18	0.00345
	Inner Mesh						
	Horizontal	ϕ8	0.34	500	0.00323	464.70	0.00266
	Vertical	ϕ8	0.34	500	0.00323	464.70	0.00266
SW-T2-S2-3	**Boundary Mesh**						
	Horizontal	ϕ8	0.68	500	0.00323	464.83	0.00262
	Vertical	ϕ16	5.15	440	0.00430	409.18	0.00345
	Inner Mesh						
	Horizontal	ϕ8	0.68	500	0.00323	464.83	0.00262
	Vertical	ϕ8	0.68	500	0.00323	464.83	0.00262

For the second set of specimens, the calibrated values are presented in Table 3.8. Four different bar diameter values, ϕ8, ϕ14, ϕ16 and ϕ22, were used in the construction of these specimens.

Table 3.8. Calibrated values of the constitutive parameters of reinforcing steel bars for specimens SW-T2-S3-4, SW-T3-S1-5, SW-T4-S1-6, and SW-T5-S1-7.

Specimen	Mesh Location	ϕ	ρ	Compression		Tension	
				f_y	b	σ_n*	b'
SW-T2-S3-4	**Boundary Mesh**						
	Horizontal	ϕ8	0.68	575	0.00815	534.56	0.00656
	Vertical	ϕ16	5.15	525	0.00282	488.22	0.00227
	Inner Mesh						
	Horizontal	ϕ8	0.68	575	0.00815	534.56	0.00656
	Vertical	ϕ8	0.68	575	0.00815	534.56	0.00656
SW-T3-S1-5	**Boundary Mesh**						
	Horizontal	ϕ8	0.68	575	0.00815	534.53	0.00657
	Vertical	ϕ8	0.65	575	0.00815	534.52	0.00657
	Inner Mesh						
	Horizontal	ϕ8	0.68	575	0.00815	534.53	0.00657
	Vertical	ϕ8	0.68	575	0.00815	534.53	0.00657
SW-T4-S1-6	**Boundary Mesh**						
	Horizontal	ϕ8	0.68	575	0.00815	534.50	0.00658
	Vertical	ϕ14	3.95	535	0.00395	497.51	0.00317
	Inner Mesh						
	Horizontal	ϕ8	0.68	575	0.00815	534.50	0.00658
	Vertical	ϕ8	0.68	575	0.00815	534.50	0.00658
SW-T5-S1-7	**Boundary Mesh**						
	Horizontal	ϕ8	0.68	575	0.00815	534.50	0.00658
	Vertical	ϕ22	9.75	550	0.00647	511.48	0.00518
	Inner Mesh						
	Horizontal	ϕ8	0.68	575	0.00815	534.50	0.00658
	Vertical	ϕ8	0.34	575	0.00815	534.24	0.00663

For the third and the last set of specimens, the calibrated parameters are listed in Table 3.9. Four different bar diameters were used in these specimens also. The bare bar parameters were identical for the second and the third sets of specimens.

Table 3.9. Calibrated values of the constitutive parameters of reinforcing steel bars for specimens SW-T6-S1-8, SW-T1-S2-9, SW-T1-N5-S1-10, and SW-T1-N10-S1-11.

Specimen	Mesh Location	ϕ	ρ	Compression		Tension	
				f_y	b	σ_n*	b'
SW-T6-S1-8	**Boundary Mesh**						
	Horizontal	ϕ8	0.68	575	0.00815	534.62	0.00655
	Vertical	ϕ22	9.75	550	0.00647	511.49	0.00518
	Inner Mesh						
	Horizontal	ϕ8	0.68	575	0.00815	534.62	0.00655
	Vertical	ϕ8	0.68	575	0.00815	534.62	0.00655
SW-T1-S2-9	**Boundary Mesh**						
	Horizontal	ϕ8	0.34	575	0.00815	534.46	0.00659
	Vertical	ϕ16	5.15	525	0.00282	488.23	0.00226
	Inner Mesh						
	Horizontal	ϕ8	0.34	575	0.00815	534.46	0.00659
	Vertical	ϕ8	0.34	575	0.00815	534.46	0.00659
SW-T1-N5-S1-10	**Boundary Mesh**						
	Horizontal	ϕ8	0.34	575	0.00815	534.42	0.00659
	Vertical	ϕ16	5.15	525	0.00282	488.23	0.00226
	Inner Mesh						
	Horizontal	ϕ8	0.34	575	0.00815	534.42	0.00659
	Vertical	ϕ8	0.34	575	0.00815	534.42	0.00659
SW-T1-N10-S1-11	**Boundary Mesh**						
	Horizontal	ϕ8	0.34	575	0.00815	534.41	0.00660
	Vertical	ϕ16	5.15	525	0.00282	488.23	0.00226
	Inner Mesh						
	Horizontal	ϕ8	0.34	575	0.00815	534.41	0.00660
	Vertical	ϕ8	0.34	575	0.00815	534.41	0.00660

3.4.2.2. Calibration of the Constitutive Model for Concrete: Calibration studies were conducted to adjust the constitutive material parameters for representation of the stress-strain curve for concrete in compression and in tension. The compression envelope curve of the model by Chang and Mander (1994) is defined by the initial slope E_c (elastic modulus of concrete), the peak coordinate ($\varepsilon_c^{'}$, $f_c^{'}$), a parameter r from Tsai's (1988) equation defining the shape of the envelope curve, and the parameter $x_{cr}^{'} > 1$ to define the normalized strain at which the stress-strain curve transforms into a straight line (Figure 3.16).

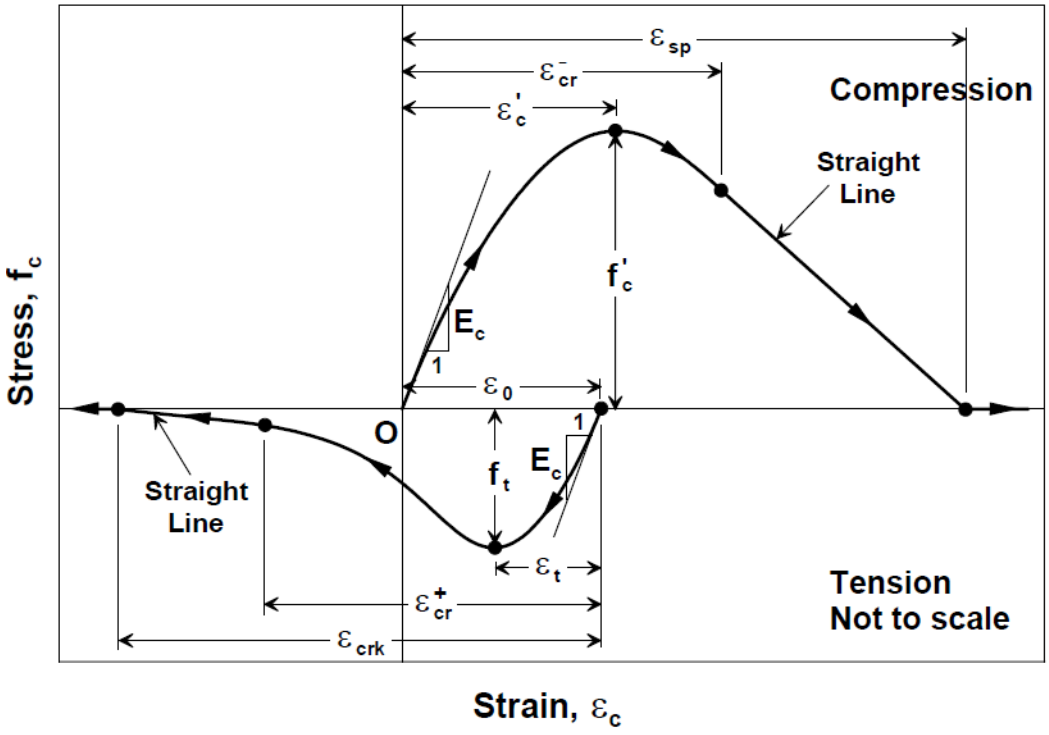

Figure 3.16. Compression and tension envelope curves of the Model by Chang and Mander.

The calibration of the material properties of concrete in compression and in tension was conducted using different criteria. For concrete in compression, the constitutive parameters other than the as-tested compressive strength value were mostly calibrated using the empirical relationships recommended by Chang and Mander. However, in order to calibrate the critical strain parameter which defines the strain value at which the envelope curve becomes a straight line, the Saatcioglu-Razvi Model (1992) for concrete in

compression was used for comparison. For concrete in tension, the constitutive parameters of the model were calibrated to represent the empirical relationships suggested by Belarbi and Hsu (1994), represent tension stiffening effects on the tensile stress-strain behavior of concrete.

Concrete in Compression: The parameters that are related to compression envelope curve of the model are the compressive strength of concrete ($f_c^{'}$), the strain at compressive strength ($\varepsilon_c^{'}$), the initial Young's Modulus (E_c), the parameter r defining the shape of the envelope and the normalized critical strain x_{cr}^{-} (also named x_{cm}) where the curve becomes a straight line. Chang and Mander (1994) recommend empirical relationships for the parameters E_c, $\varepsilon_c^{'}$ and r as:

Initial modulus of elasticity : $$E_c = 185000(f_c^{'})^{(3/8)} \quad (3.7)$$

Strain at compressive strength: $$\varepsilon_c^{'} = \frac{\left(f_c^{'}\right)^{0.25}}{4000} \quad (3.8)$$

Shape parameter : $$r = \frac{f_c^{'}}{750} - 1.9 \quad (3.9)$$

The unit of $f_c^{'}$ in the empirical formulas above is MPa.

Since an empirical relationship is not suggested for the normalized critical strain parameter x_{crn}, this parameter value was calibrated graphically by comparing the shape of the stress-strain envelope of the Chang and Mander (1994) model with the Saatcioglu and Razvi (1992) model for unconfined concrete. The calibration criterion was to attain parallel straight lines in the descending region of the two stress-strain relationships, as shown in Figure 3.17. In order to obtain the calibrated x_{crn} values, many trials were conducted for each individual specimen. Calibrated constitutive parameters for concrete in compression are presented in Table 3.10 for all wall specimens.

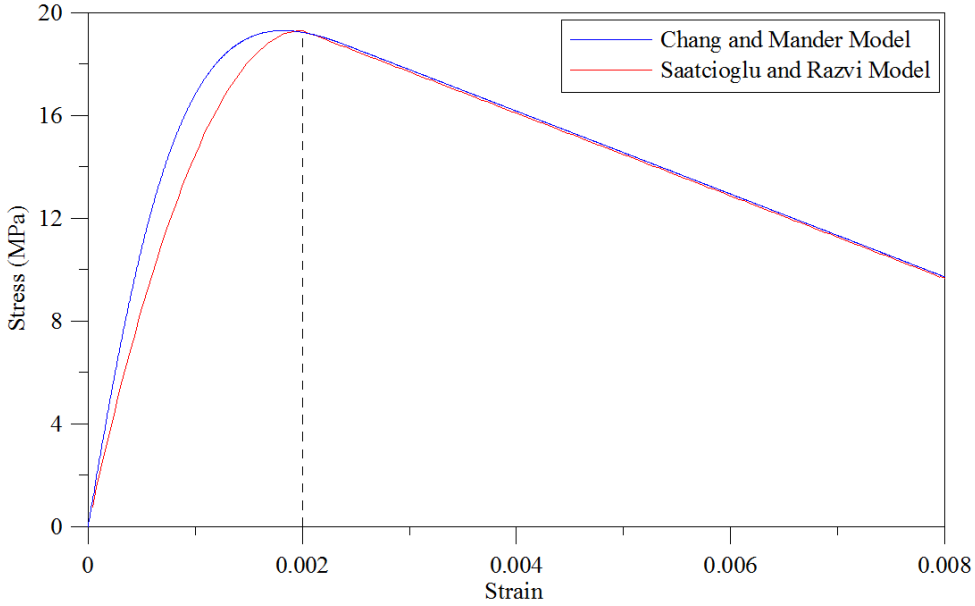

Figure 3.17. Stress-strain diagrams for concrete in compression for specimen SW-T2-S1-1.

Table 3.10. Calibrated values of the constitutive parameters for concrete in compression.

Specimen	**f_c' (Mpa)**	**E_c (Mpa)**	**ε_c'**	**r**	**X_{crn}**
SW-T2-S1-1	19.3	25022	0.00182	1.832	1.320
SW-T1-S1-2	23.7	27026	0.00191	2.683	1.155
SW-T2-S2-3	25.8	27900	0.00196	3.089	1.127
SW-T2-S3-4	29.0	29150	0.00201	3.708	1.098
SW-T3-S1-5	32.1	30282	0.00207	4.308	1.081
SW-T4-S1-6	34.8	31213	0.00211	4.830	1.070
SW-T5-S1-7	35.0	31280	0.00211	4.868	1.069
SW-T6-S1-8	22.6	26548	0.00189	2.470	1.178
SW-T1-S2-9	24.0	27153	0.00192	2.741	1.152
SW-T1-N5-S1-10	26.3	28101	0.00196	3.186	1.121
SW-T1-N10-S1-11	27.0	28380	0.00198	3.321	1.115

Concrete in Tension: The constitutive parameters that are to be calibrated for concrete in tension include the initial Young's modulus of the average stress-strain relationship (E_c), the tensile (cracking) strength of concrete (f_{cr}), and the strain at cracking (ε_{cr}), the parameter *r* representing the shape of the curve, and the normalized critical strain at which the stress-strain curve becomes a straight line (x_{crp}). Since material test results were available for none of these parameters, and also to incorporate the effects of tension stiffening on concrete in tension, these parameters were calibrated so that the tensile stress-strain relationship for concrete in tension is compatible with the empirical relationships suggested by Belarbi and Hsu (1994) for concrete in tension. The average stress-strain relationship proposed by Belarbi and Hsu (1994) for concrete in tension (Figure 3.18) is defined by the following equations:

$$\text{If} \quad \varepsilon_c > \varepsilon_{cr} \quad \text{then} \quad \sigma_c = E_c \, \varepsilon_c \tag{3.10}$$

$$\text{If} \quad \varepsilon_c > \varepsilon_{cr} \quad \text{then} \quad \sigma_c = f_{cr} \left(\frac{\varepsilon_{cr}}{\varepsilon_c} \right)^{0.4} \tag{3.11}$$

where:

$$E_c = 3875 \sqrt{f_c'(MPa)} \tag{3.12}$$

$$f_{cr} = 0.31 \sqrt{f_c'(MPa)} \tag{3.13}$$

$$\varepsilon_{cr} = 0.00008 \tag{3.14}$$

The stress-strain relationship of Belarbi and Hsu (1994) consists of two regions, the first of which is the linear region, and the second of which is the exponentially-descending region, as illustrated in Figure 3.18.

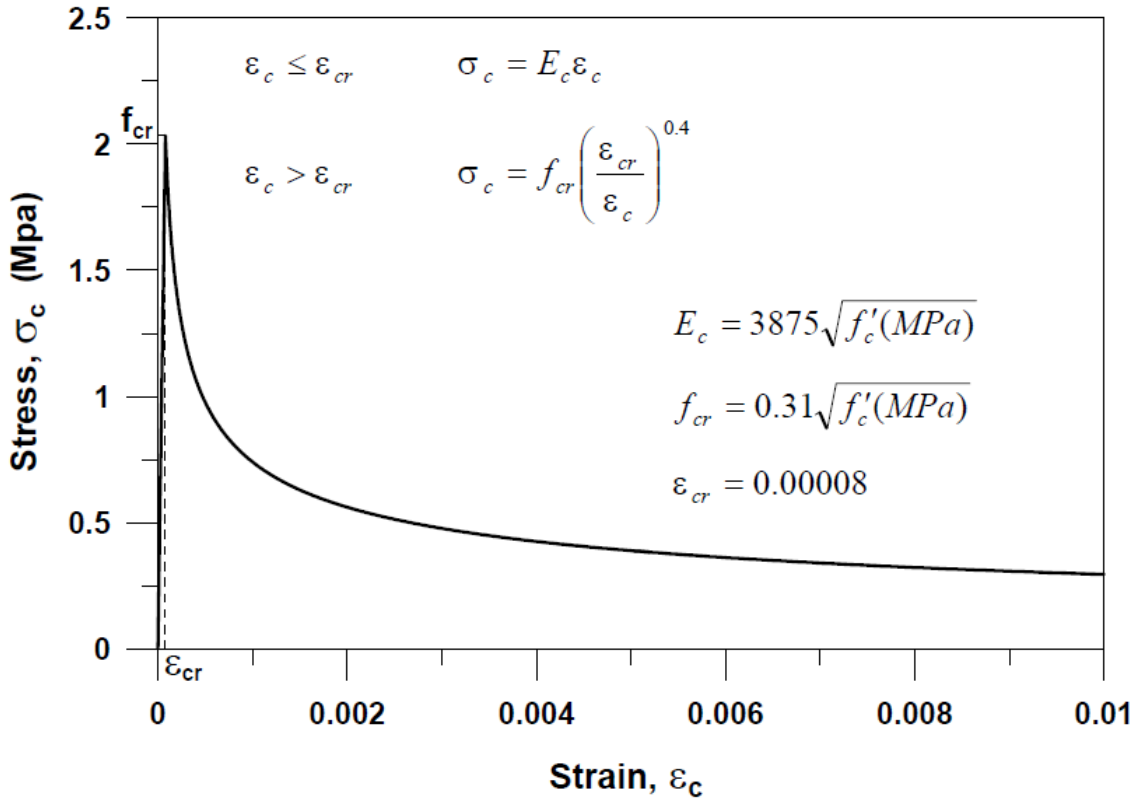

Figure 3.18. Stress-strain relationship by Belarbi and Hsu (1994) for concrete in tension.

The normalized critical strain value for concrete in tension, at which the stress-strain curve becomes a straight line (x_{crp}), was calibrated for a very large value (e.g., 10000), so that the curve does not transform into a straight line and continues as a curve, the shape of which resembles the descending region of the relationship by Belarbi and Hsu (1994). The parameter r_t (controlling the shape of the tension envelope) was calibrated graphically by comparing the shape of the stress-strain diagram obtained by the Chang and Mander (1994) model with the Belarbi and Hsu (1994) relationship, so that similar shapes are obtained for the stress-strain curves, as depicted in Figure 3.19. The calibrated parameters of concrete in tension are presented in Table 3.11 for all wall specimens.

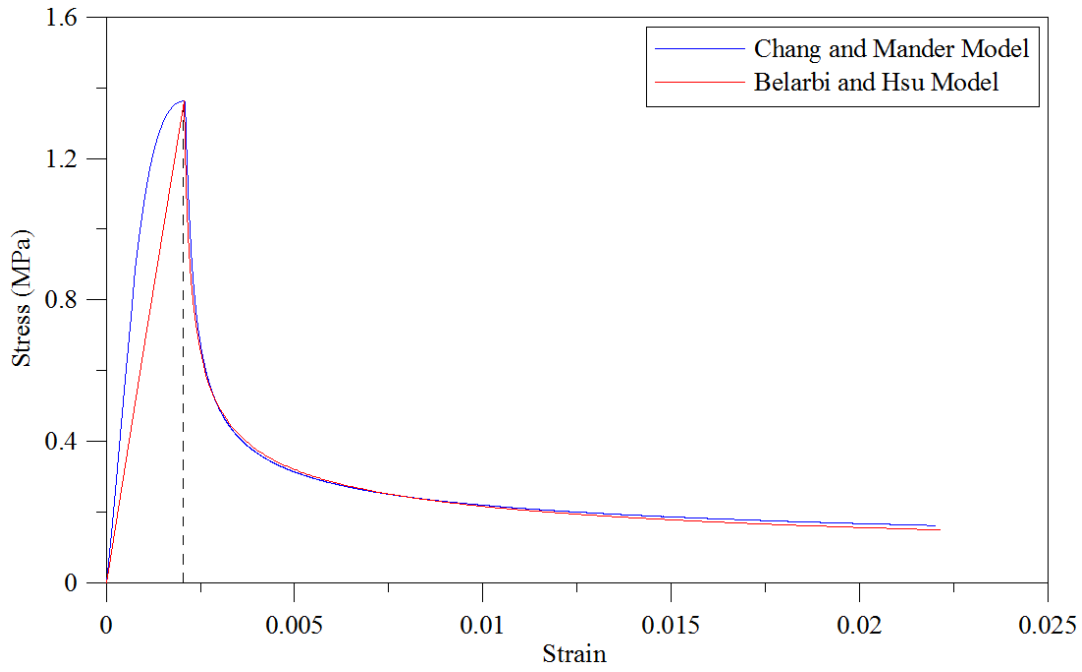

Figure 3.19. Stress-strain diagrams for concrete in tension for specimen SW-T2-S1-1.

Table 3.11. Calibrated values of the constitutive parameters for concrete in tension.

Specimen	**E_c (Mpa)**	**f_{cr} (Mpa)**	**ε_{cr}**	**r_t**	**X_{crp}**
SW-T2-S1-1	25022	1.362	0.00008	1.25	10000
SW-T1-S1-2	27026	1.509	0.00008	1.25	10000
SW-T2-S2-3	27900	1.575	0.00008	1.25	10000
SW-T2-S3-4	29150	1.669	0.00008	1.24	10000
SW-T3-S1-5	30282	1.756	0.00008	1.24	10000
SW-T4-S1-6	31213	1.829	0.00008	1.23	10000
SW-T5-S1-7	31280	1.834	0.00008	1.23	10000
SW-T6-S1-8	26548	1.474	0.00008	1.25	10000
SW-T1-S2-9	27153	1.519	0.00008	1.25	10000
SW-T1-N5-S1-10	28101	1.590	0.00008	1.24	10000
SW-T1-N10-S1-11	28380	1.611	0.00008	1.24	10000

4. ANALYSIS RESULTS AND COMPARISONS WITH EXPERIMENTAL DATA

This Chapter presents analytical results obtained using the finite element wall model that was calibrated as described in the previous Chapter. Model predictions are compared with the experimentally-observed lateral load vs. displacement responses obtained for the eleven squat wall specimens tested by Terzioglu (2011). Results of parametric sensitivity studies conducted to investigate the influence of the parameters associated with the constitutive shear aggregate interlock and dowel relationships on the model results, are also provided.

The constitutive parameters of the behavioral models associated with shear aggregate interlock effects in concrete and dowel action on reinforcing bars were first investigated. In order to obtain reasonable values for the parameters, specimen SW-T3-S1-5, which experienced a sliding shear failure at the wall-pedestal interface, was analyzed several times, since its response was expected to be governed by interlock and dowel mechanisms developing along the interface crack. The sensitivity of the model results to the friction coefficient in the shear aggregate interlock model for concrete and the shear stress capacity coefficient in the dowel action model for reinforcing steel were investigated parametrically. As well, sensitivity of the model results to the exponential degradation coefficient associated with the descending region of the dowel shear stress vs. shear strain relationship was studied. Based on the results of the sensitivity studies, values were recommended for these behavioral parameters, and analyses were conducted for all remaining wall specimens using the recommended values. In order to evaluate the effectiveness of the nonlinear constitutive dowel action model implemented in the model formulation, analysis results were first obtained using a hypothetical linear elastic relationship for dowel action. The analysis results are presented in the following sections.

4.1. Model Sensitivity to the Constitutive Parameters of the Shear Transfer Mechanisms across Cracks

In order to parametrically investigate the influence of the constitutive parameters of the behavioral models associated with shear aggregate interlock effects in concrete and dowel action on reinforcing bars, a total of twelve analyses were conducted for specimen SW-T3-S1-5. Since the experimentally-observed failure mode of this specimen was sliding shear at the base of the wall, it was deemed as the most suitable specimen for the sensitivity analysis. During testing, this specimen reached a lateral load capacity 440 kN in the positive loading direction and a capacity of 320 kN capacity in the negative loading direction. The experimentally-obtained lateral load vs. top displacement response of this specimen is shown in Figure 4.1. Analytical response predictions were obtained for this specimen, for different combinations of the friction coefficient in the constitutive shear aggregate interlock model for concrete (depicted as CC in later discussion), the shear stress capacity coefficient in the dowel action model for reinforcement (depicted as CS), and the exponential degradation coefficient associated with the descending region of the dowel action model (depicted as S). The coefficients used in the analyses are listed in Table 4.1.

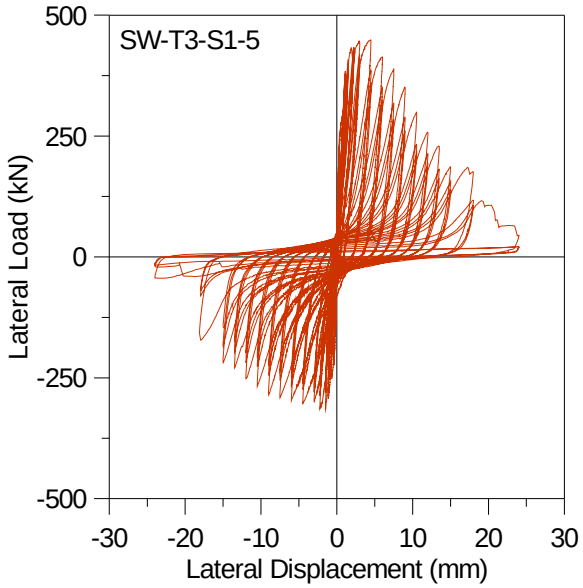

Figure 4.1. Test results obtained for specimen SW-T3-S1-5.

The shear stress capacity coefficients for concrete and reinforcing steel (CC and CS) are assigned equal values of 1.0, 0.5, and 0.1 for first three analyses. The exponential degradation coefficient for reinforcing steel (S) is taken as 0.4 for these analyses. Corresponding analysis results are provided in Figure 4.2. In the cases where the concrete and steel capacity coefficients were assigned as 1.0 and 0.5, it appears that that the lateral load capacity of the wall is overestimated. On the contrary, the lateral load capacity of the wall specimen is underestimated when these coefficients were assigned a value of 0.1. It was concluded that the shear stress capacity coefficients for concrete and reinforcing steel lay in the range of 0.1 and 1.0, based on the results of the first three analyses. As well, in order to better investigate the influence of the exponential degradation coefficient for reinforcing steel on the analytical response, further analyses were conducted by modifying this coefficient.

Table 4.1. Varying parameters associated with shear transfer across cracks.

Coefficient for Aggregate Interlock Capacity in Concrete (CC)	**Coefficient for Dowel Capacity in Steel (CS)**	**Exponential Degradation Coefficient in Steel (S)**
1.0	1.0	0.4
0.5	0.5	0.4
0.1	0.1	0.4
0.1	0.1	0.8
0.3	0.1	0.2
0.3	0.1	2.0
0.5	0.1	2.0
0.5	0.1	5.0
0.5	0.25	2.0
1.0	0.1	5.0
1.0	0.2	5.0
1.0	0.3	5.0

Since the experimentally-measured lateral load capacity of the specimen could not be obtained during the first three analyses, a fourth analysis was conducted for which the concrete and reinforcing steel shear stress capacity coefficients were taken as 0.1, and the exponential degradation coefficient for reinforcing steel was assigned a value of 0.8. It was observed that the degradation coefficient has no remarkable effect on the lateral load capacity of the wall. The influence of the exponential degradation coefficient on the constitutive shear stress vs. shear strain model implemented for dowel action on reinforcing bars is illustrated in Figure 4.3. As can be observed in the figure, the coefficient only influences the rate of degradation in dowel-action-induced shear stresses, and not the shear stress capacity. Therefore, the lateral load capacity of the wall is also not significantly sensitive to the exponential degradation coefficient selected for reinforcing steel.

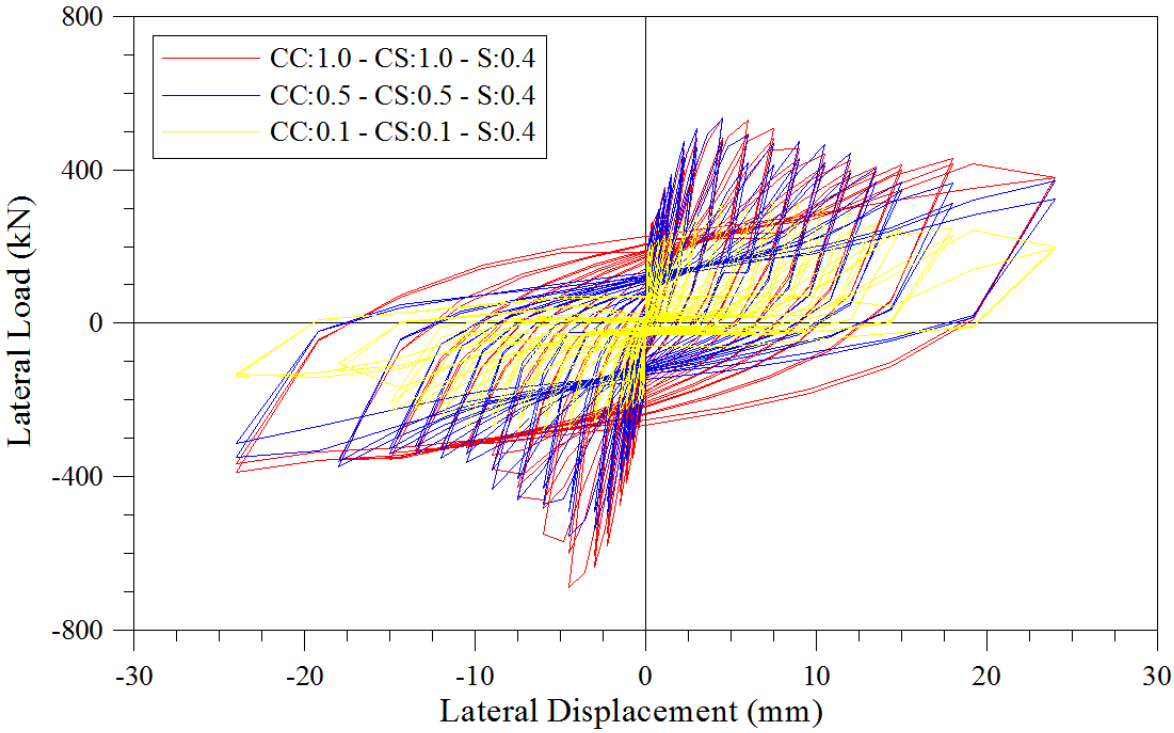

Figure 4.2. Results of the first three sensitivity analyses.

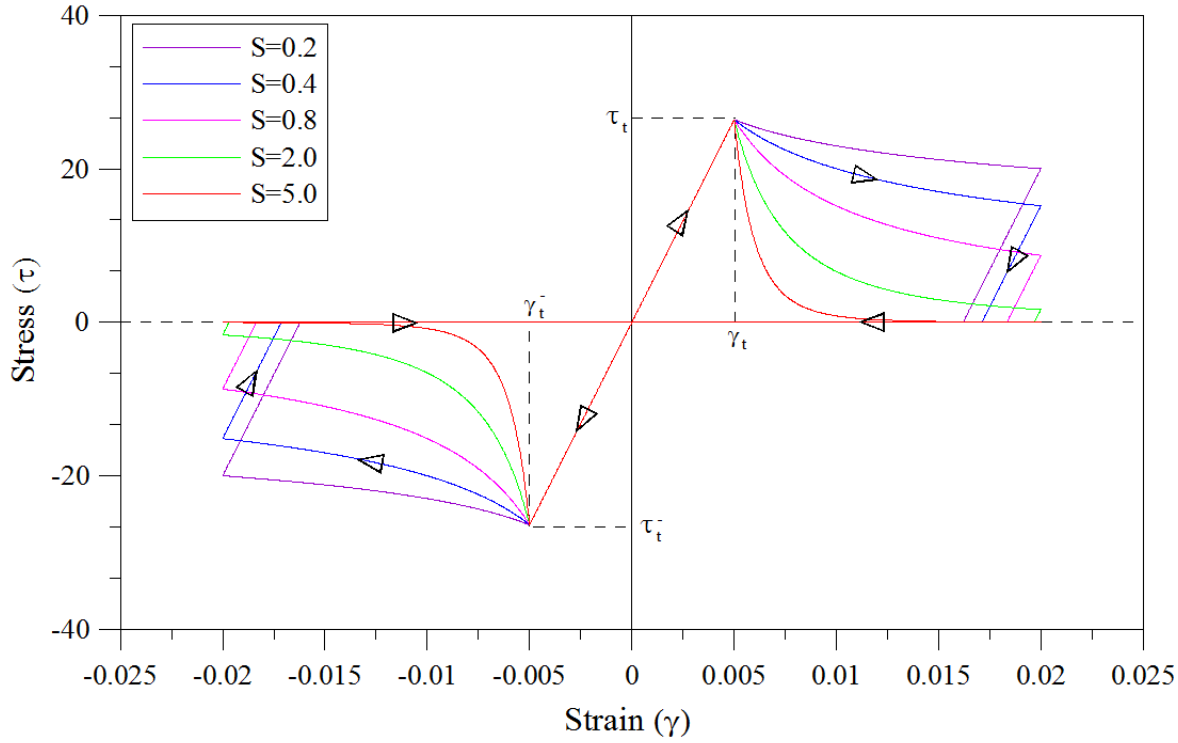

Figure 4.3. The influence of the exponential degradation coefficient on the constitutive shear stress vs. strain model for dowel action on reinforcement.

Results of first sensitivity analyses showed that the lateral load capacity of the specimen is influenced by the shear stress capacity coefficients selected for concrete and reinforcing steel, whereas the rate of decrease in the lateral load is modestly influenced by the exponential degradation coefficient for reinforcing steel. Further analyses were conducted for calibrating the coefficients so that the test results obtained for specimen SW-T3-S1-5 are reasonably captured by the wall model. For the next set of analyses, the reinforcing steel shear stress capacity coefficient was kept at a constant value of 0.1, and the concrete shear stress capacity coefficient was assigned a constant value of 0.3, while the exponential degradation coefficient for reinforcing steel was assigned two different values: 0.2 and 2,0. Results of these analyses are depicted in Figure 4.4.

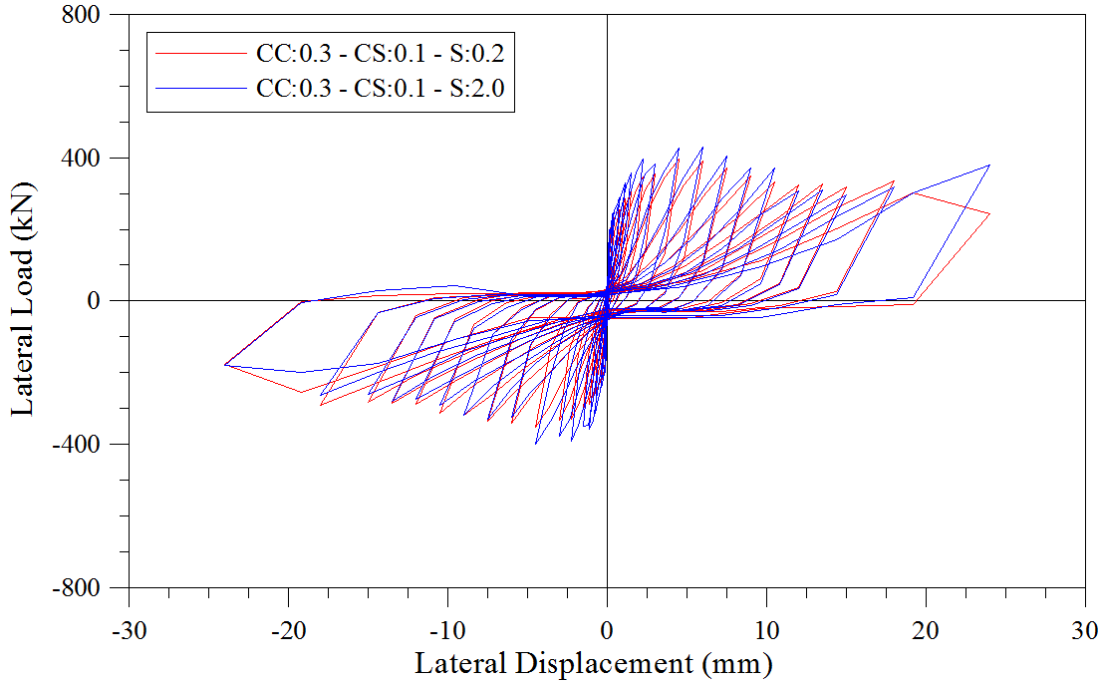

Figure 4.4. Sensitivity of the response to the exponential degradation coefficient for reinforcing steel.

The analysis results shown in the figure showed that a reasonable prediction is obtained for the pinched shape of the hysteretic response, when a relatively small value is used for the shear stress capacity coefficient for reinforcing steel. As well, degradation in lateral load is not notably sensitive to the exponential degradation coefficient for reinforcing steel, when the steel shear stress capacity coefficient is relatively small. In order to increase the lateral load capacity prediction of the model, during further analyses, larger values were selected for the shear stress capacity coefficient for concrete, For three additional analyses, the concrete shear stress capacity coefficient was kept at a constant value of 0.5, whereas the shear stress capacity coefficient for steel was taken as 0.1 and 0.25, and the exponential degradation coefficient for steel was as assigned values of 2.0 and 5.0. Results of these analyses are illustrated in Figure 4.5.

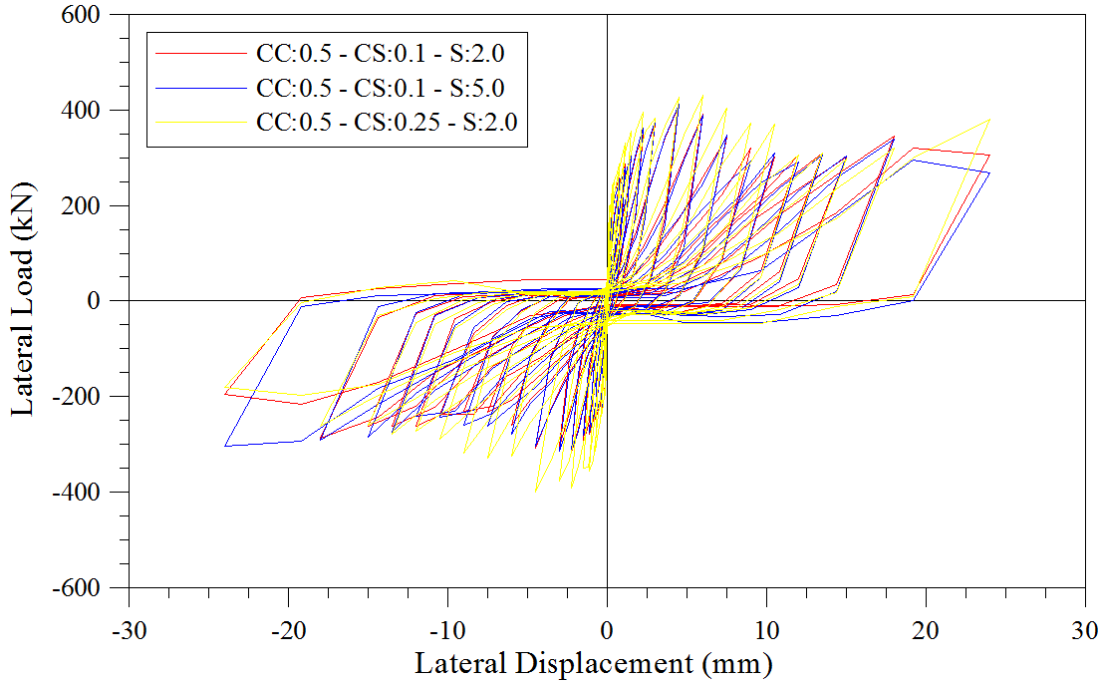

Figure 4.5. Sensitivity of the response to the shear stress capacity coefficient and the exponential degradation coefficient for reinforcing steel.

A final set of analyses were conducted, for which the shear stress coefficient for concrete was kept at a constant value of 1.0 (as suggested previously by Gullu, 2013), the exponential degradation coefficient for reinforcing steel was kept at a constant value of 5.0, whereas the shear stress capacity for reinforcing steel was assigned values of 0.1, 0.2, and 0.3. It was observed that the correlation between analytical results (Figure 4.6) and experimental results for the lateral load vs. top displacement response of specimen SW-T3-S1-5 were in reasonable agreement when the shear stress capacity coefficient for concrete is equal to 1.0, the shear stress capacity coefficient for reinforcing steel is equal to 0.1, and the exponential degradation coefficient for reinforcing steel is equal to 5.0.

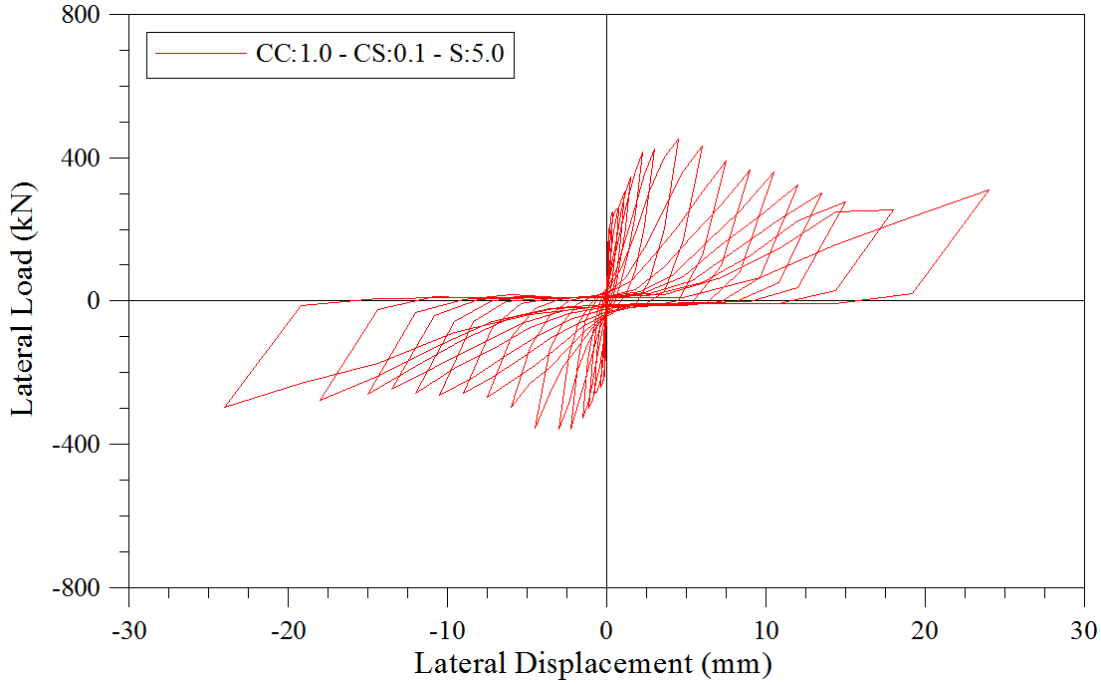

Figure 4.6. Analysis results obtained for optimal values for the shear stress transfer coefficients.

4.2. Comparison of Analysis and Test Results

Using the optimal values obtained for the shear stress capacity coefficient for concrete (1.0), shear stress capacity coefficient for reinforcing steel (0.1), and the exponential degradation coefficient for reinforcing steel (5.0), analyses were conducted for all wall specimens.

However, in order to evaluate the effectiveness of the nonlinear constitutive dowel action model implemented in the model formulation, analysis results were first obtained using a hypothetical linear elastic relationship for dowel action, which consists only of the linear elastic region of the constitutive dowel action model. The analysis results obtained with both constitutive dowel action formulations (linear elastic and nonlinear) are compared with the experimental results in the following subsections.

4.2.1. Analysis Results Obtained Using a Linear Elastic Dowel Action Model

The first set of analyses were conducted using the linear elastic region of the shear stress vs. shear strain relationship adopted for dowel action, with no bound imposed on the shear stress capacity. The analytical results obtained for the lateral load vs. top displacement responses are compared with the experimentally measured responses in Figure 4.7 to Figure 4.17. In the analyses, two loading cycles were applied to each target drift level, as opposed to the three loading cycles applied during testing. This was done to expedite the analysis, since the second and third loading cycles in the test results are almost identical.

Overall, the model provides reasonable predictions for the lateral stiffness, lateral load capacity, and ductility (lateral load degradation) characteristics of the wall specimens, except for specimen SW-T3-S1-5, which experienced sliding shear failure at the base of the wall. However, lateral load values at large displacements, the shape of the unloading/reloading loops, as well as pinching characteristics of the response, differ among the analysis and test results. The analysis results typically show higher lateral load levels and wider unloading/reloading loops at large displacements, and less pronounced pinching effects, compared to the experimentally-observed responses.

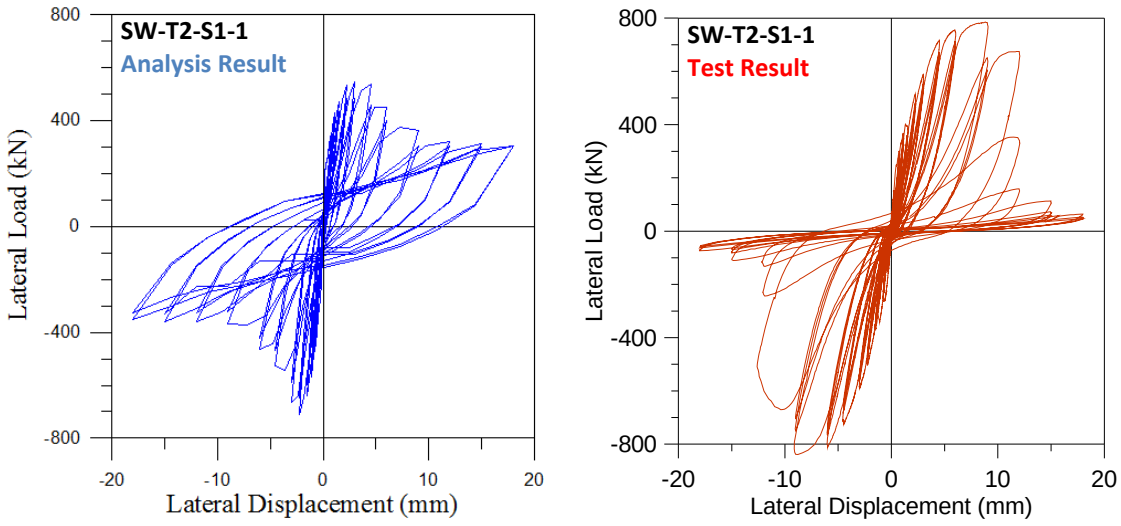

Figure 4.7. Comparison of analysis result with linear elastic dowel action vs. test result for specimen SW-T2-S1-1.

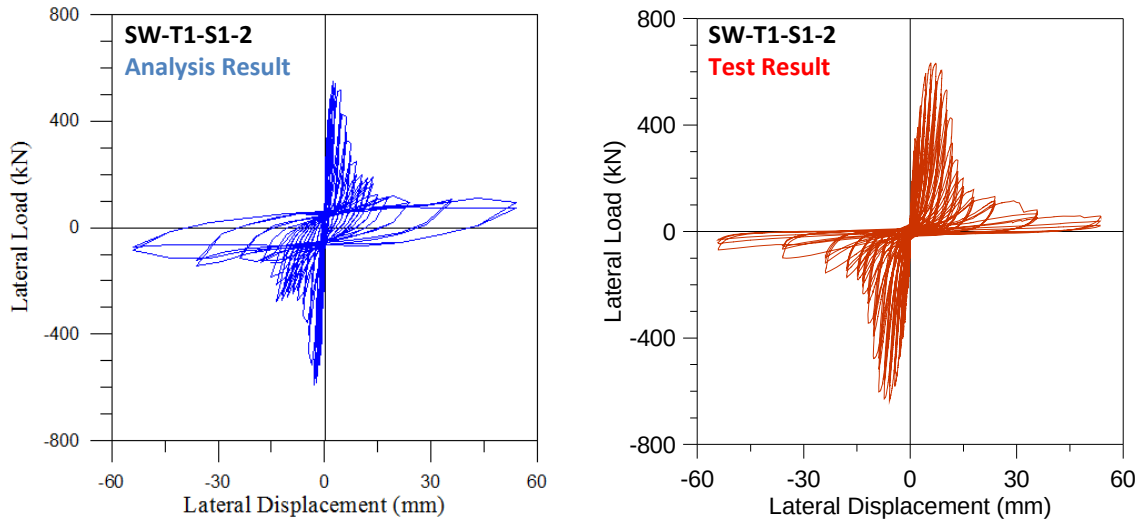

Figure 4.8. Comparison of analysis result with linear elastic dowel action vs. test result for specimen SW-T1-S1-2.

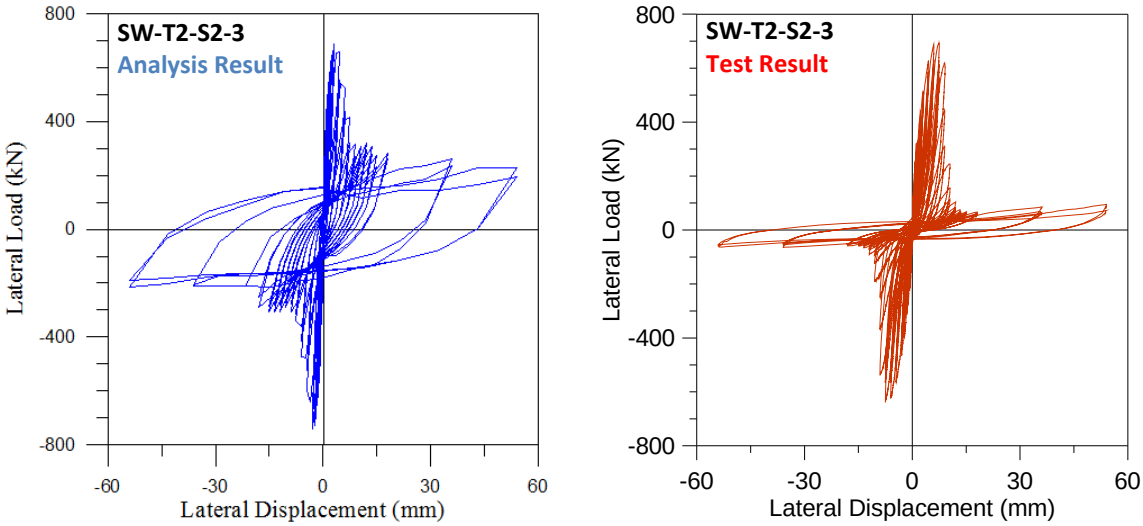

Figure 4.9. Comparison of analysis result with linear elastic dowel action vs. test result for specimen SW-T2-S2-3.

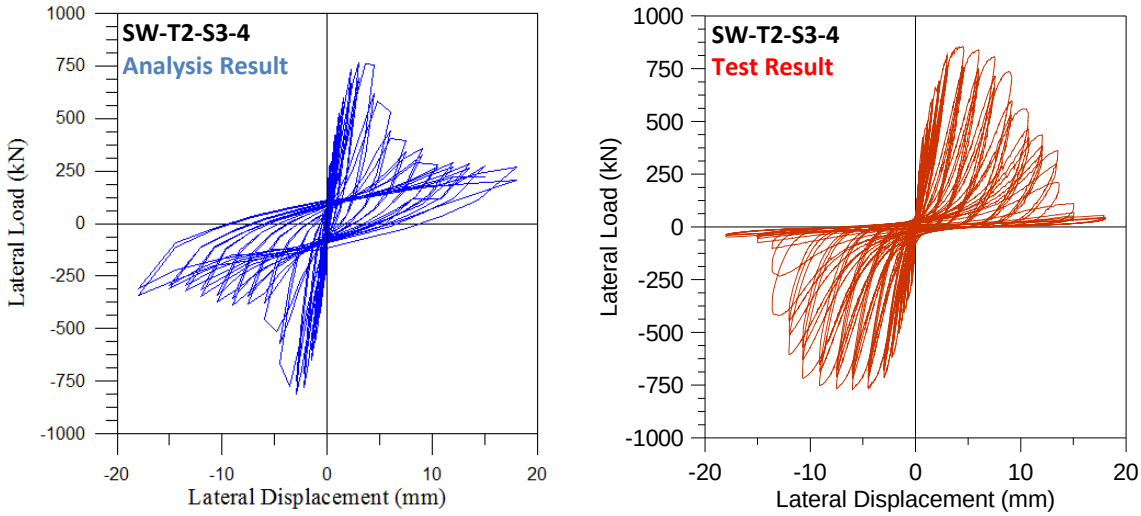

Figure 4.10. Comparison of analysis result with linear elastic dowel action vs. test result for specimen SW-T2-S3-4.

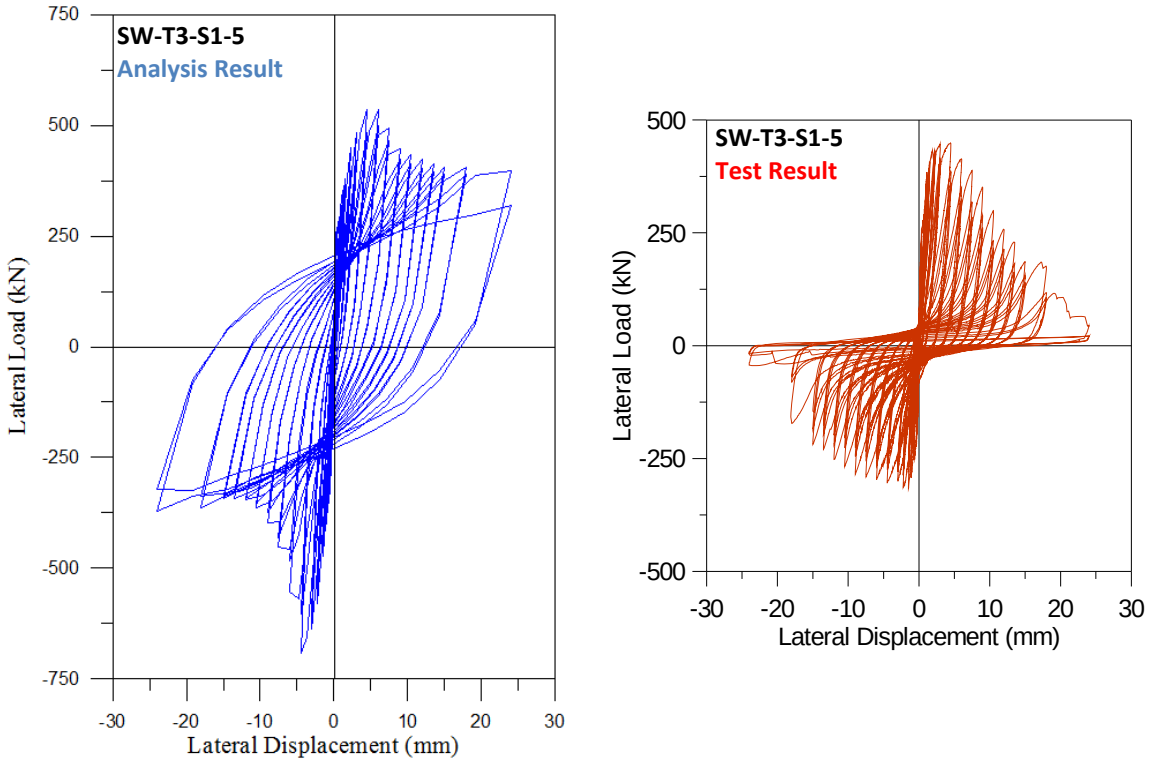

Figure 4.11. Comparison of analysis result with linear elastic dowel action vs. test result for specimen SW-T3-S1-5.

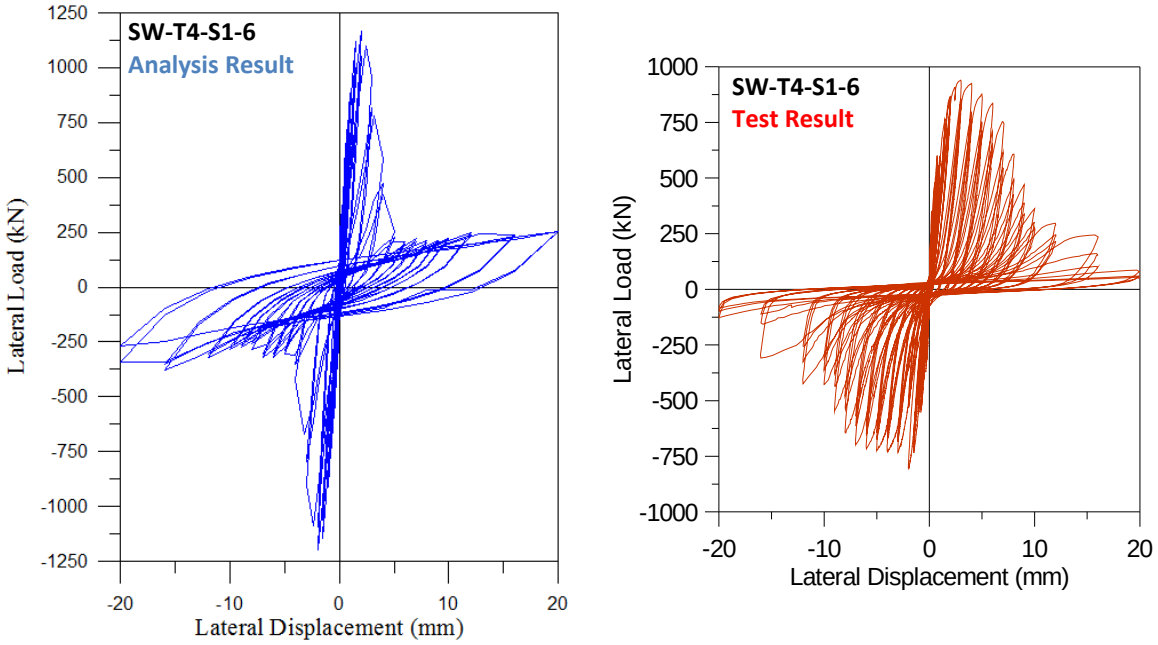

Figure 4.12. Comparison of analysis result with linear elastic dowel action vs. test result for specimen SW-T4-S1-6.

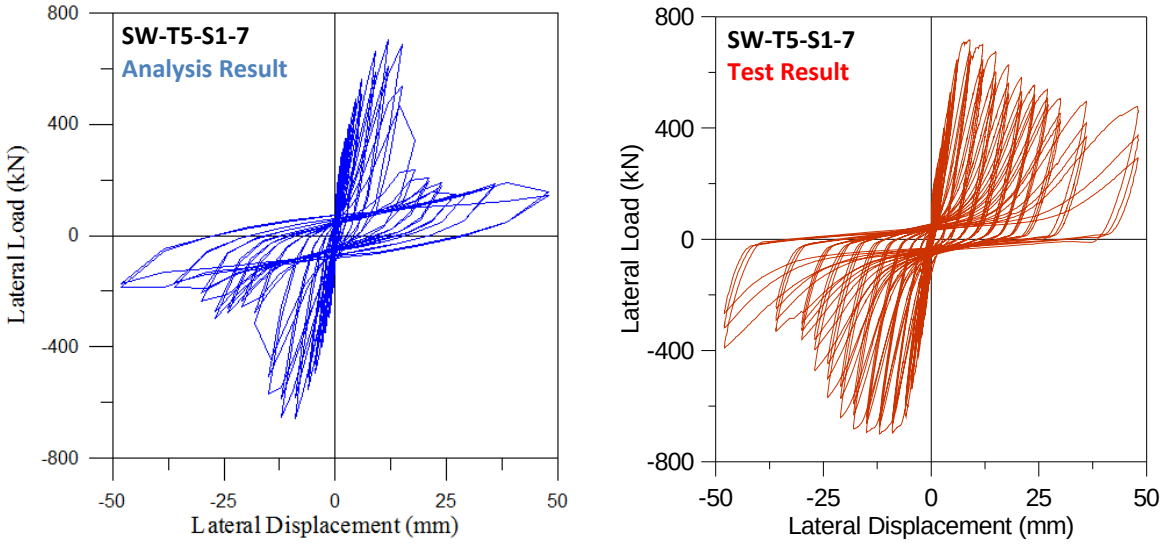

Figure 4.13. Comparison of analysis result with linear elastic dowel action vs. test result for specimen SW-T5-S1-7.

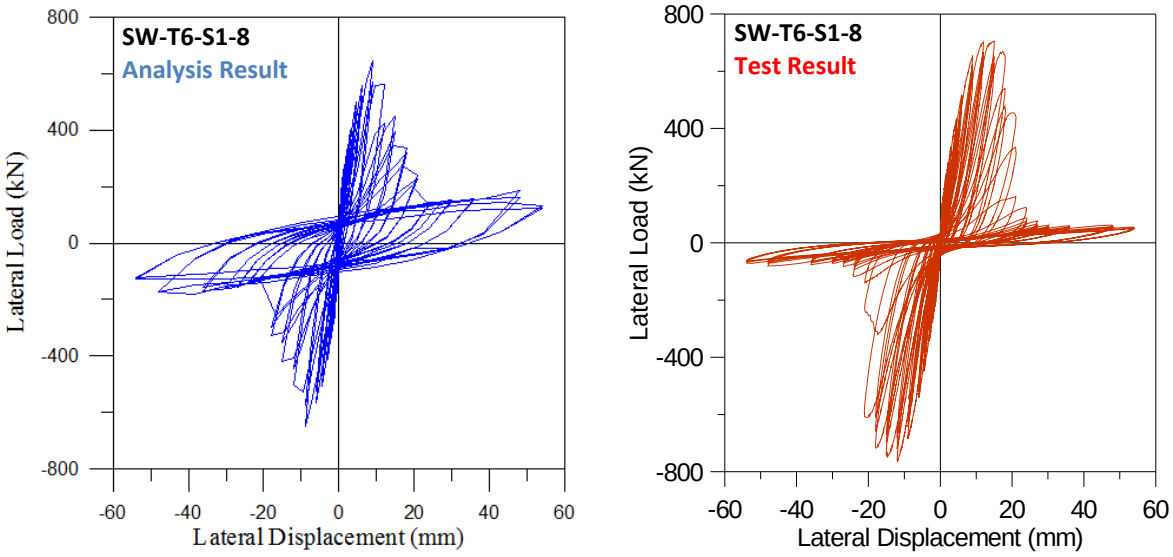

Figure 4.14. Comparison of analysis result with linear elastic dowel action vs. test result for specimen SW-T6-S1-8.

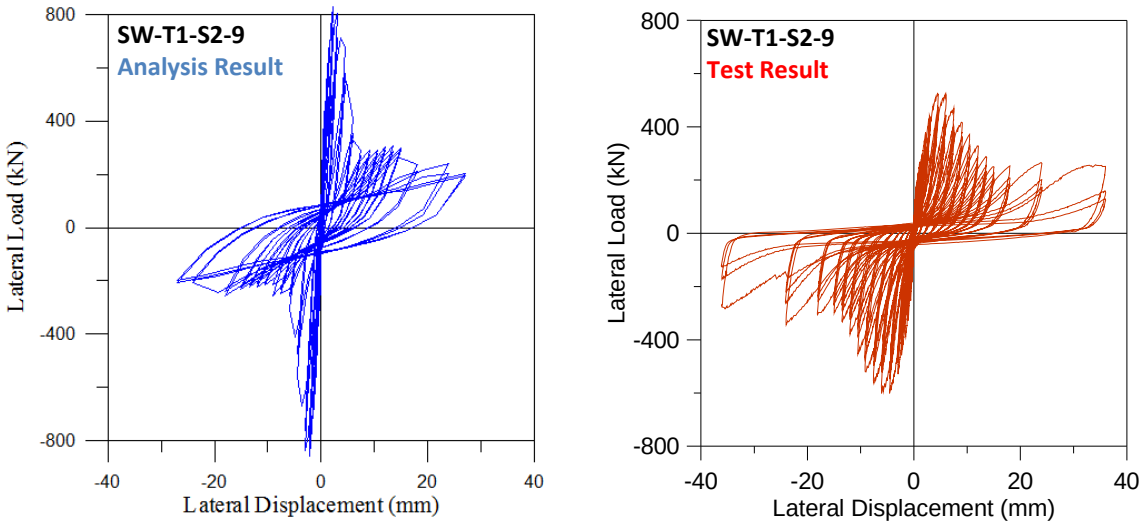

Figure 4.15. Comparison of analysis result with linear elastic dowel action vs. test result for specimen SW-T1-S2-9.

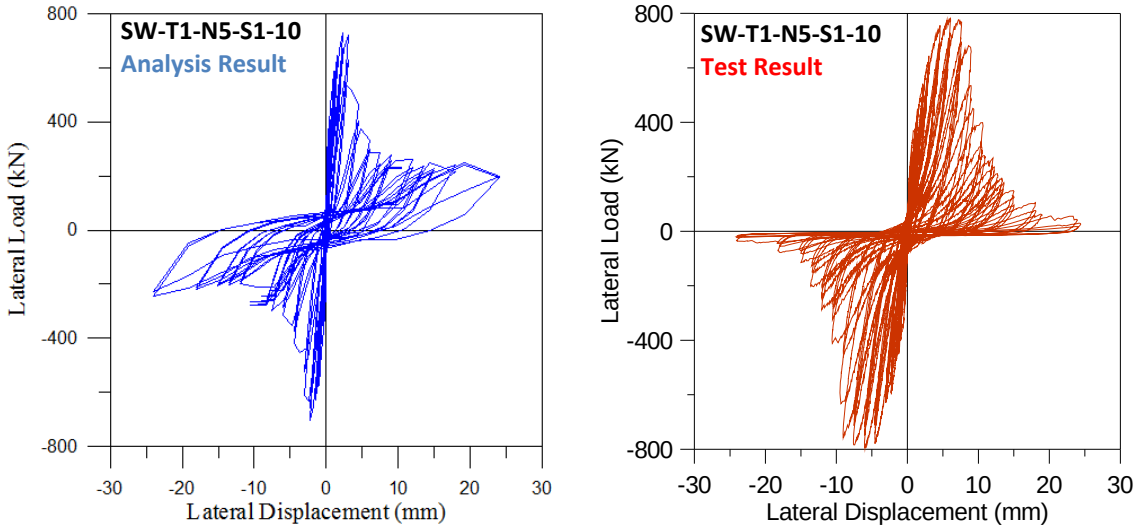

Figure 4.16. Comparison of analysis result with linear elastic dowel action vs. test result for specimen SW-T1-N5-S1-10.

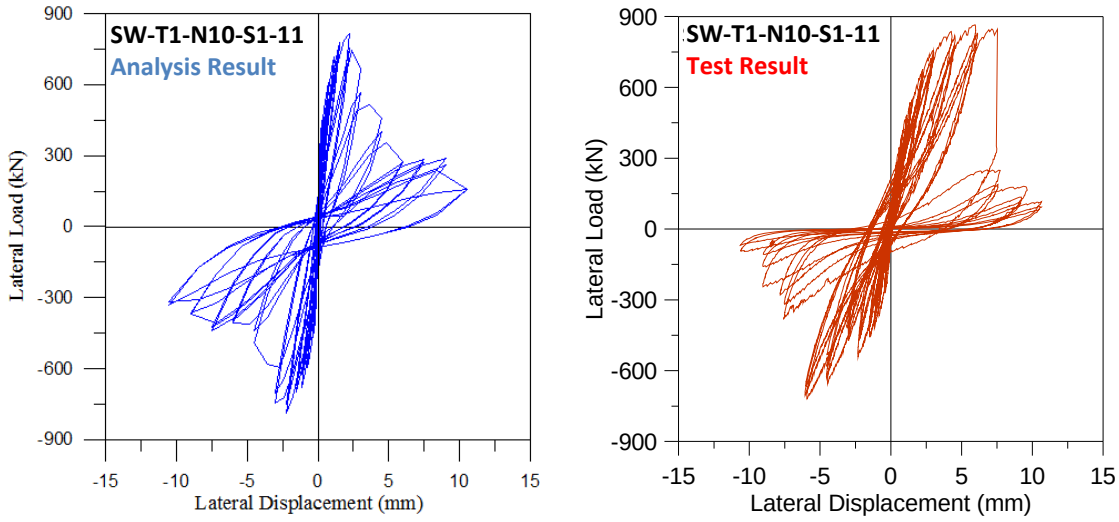

Figure 4.17. Comparison of analysis result with linear elastic dowel action vs. test result for specimen SW-T1-N10-S1-11.

4.2.2. Analyses Results Obtained Using the Proposed Nonlinear Constitutive Model for Dowel Action

The second set of analyses was conducted using the proposed nonlinear constitutive model for dowel action on reinforcing bars. The analytical results obtained for the lateral

load vs. top displacement responses are compared with the experimentally measured responses in Figure 4.18 to Figure 4.28. For also this set of analyses, two loading cycles were applied to each target drift level.

Overall, the model again provides reasonable predictions for the lateral stiffness, lateral load capacity, and ductility (lateral load degradation) characteristics of the wall specimens, including specimen SW-T3-S1-5, which experienced sliding shear failure at the base. Significantly improved predictions were obtained for lateral load values at large displacements, the shape of the unloading/reloading loops, and pinching characteristics of the response, signifying the effectiveness of the proposed nonlinear constitutive model for dowel action in improving the model predictions. Response comparisons for individual wall specimens are discussed in the following paragraphs. Comparison of analysis and test results for specimen SW-T2-S1-1 is presented in Figure 4.18. The lateral load capacity of this specimen was significantly underestimated by the model, indicating that the shear aggregate interlock and dowel action parameters that were calibrated for the specimen SW-T3-S1-5 may not be optimal for this specimen.

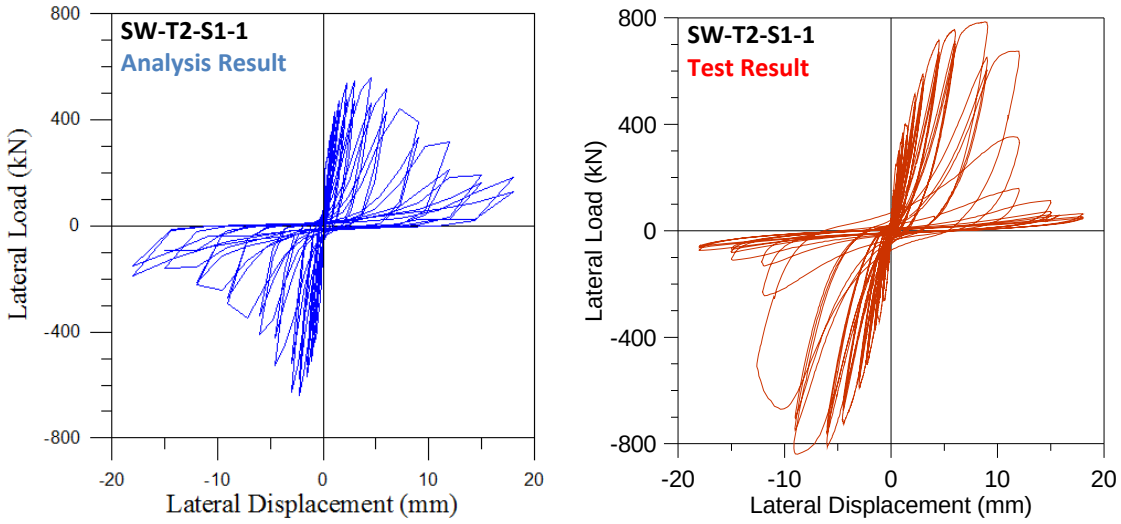

Figure 4.18. Comparison of analysis result with nonlinear dowel action vs. test result for specimen SW-T2-S1-1.

Comparison of analysis and test results for specimens SW-T1-S1-2 and SW-T2-S2-3 are presented in Figure 4.19 and Figure 4.20, respectively. Although the lateral load

capacity of specimen SW-T1-S1-2 is not accurately predicted, the analysis results are in compliance with test results in terms of ductility (degradation in lateral load), and pinching characteristics of the response. For specimen SW-T2-S2-3, although the lateral load capacity prediction is reasonably accurate, degredation in lateral load with increasing displacement is not well represented in the analysis results.

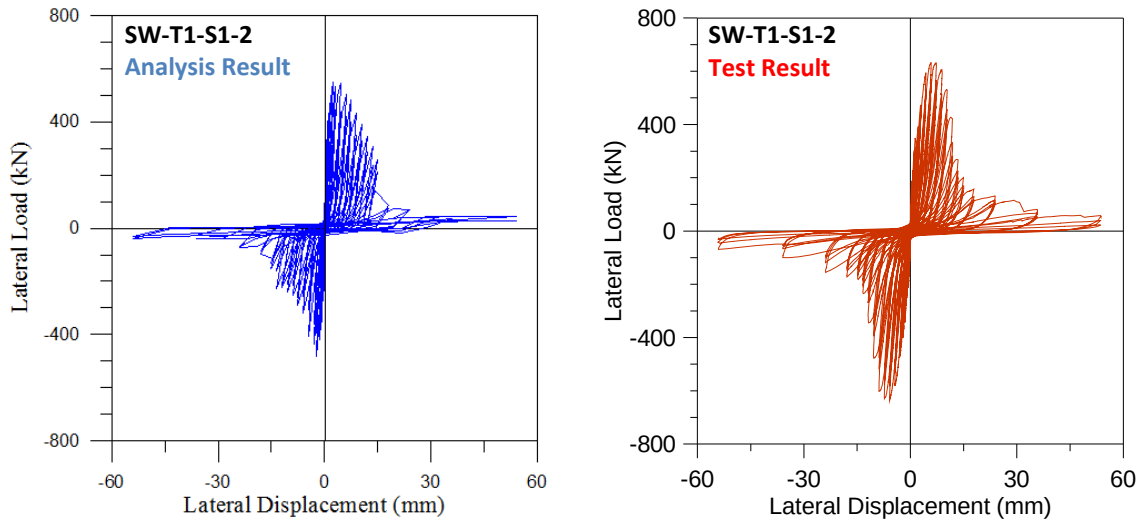

Figure 4.19. Comparison of analysis result with nonlinear dowel action vs. test result for specimen SW-T1-S1-2.

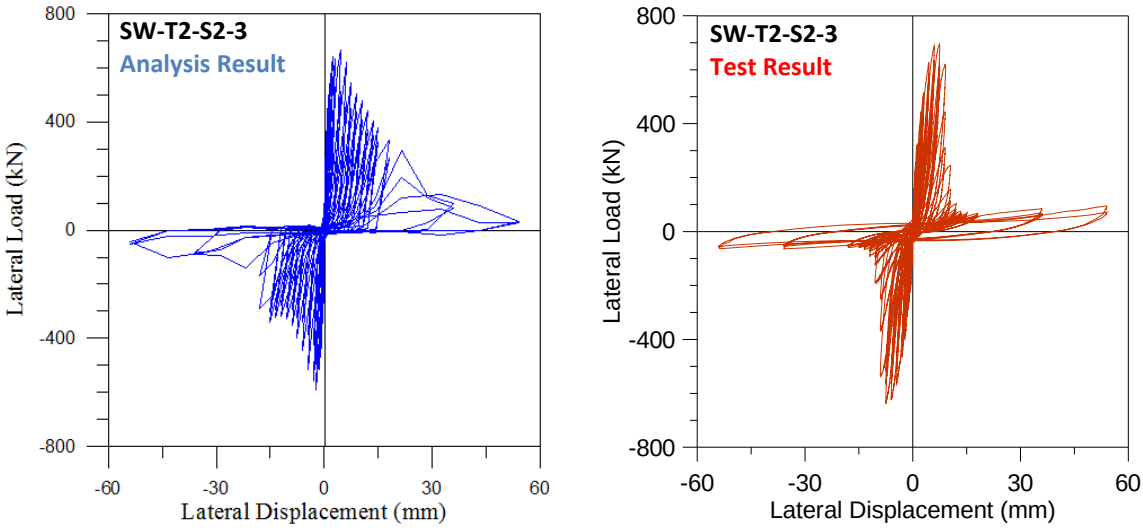

Figure 4.20. Comparison of analysis result with nonlinear dowel action vs. test result for specimen SW-T2-S2-3.

Comparison of analysis and test results for specimens SW-T2-S3-4 and SW-T3-S1-5 are presented in Figure 4.21 and Figure 4.22, respectively. The model prediction is reasonable for specimen SW-T2-S3-4; lateral load capacity, ductility, and pinching characteristics are all represented reasonably well. The lateral load capacity of specimen SW-T3-S1-5, which experienced sliding shear failure at the base, is also well estimated by the model. However, degradation of lateral load in the analysis results are not representative of test results obtained for this specimen. It is interesting to note that although the shear aggregate interlock and dowel action parameters of the model were calibrated for this particular specimen, lateral load degradation characteristics were not captured in the analysis results, implying that loading history may also have a significant effect on the influence of the parameters on the analytical response.

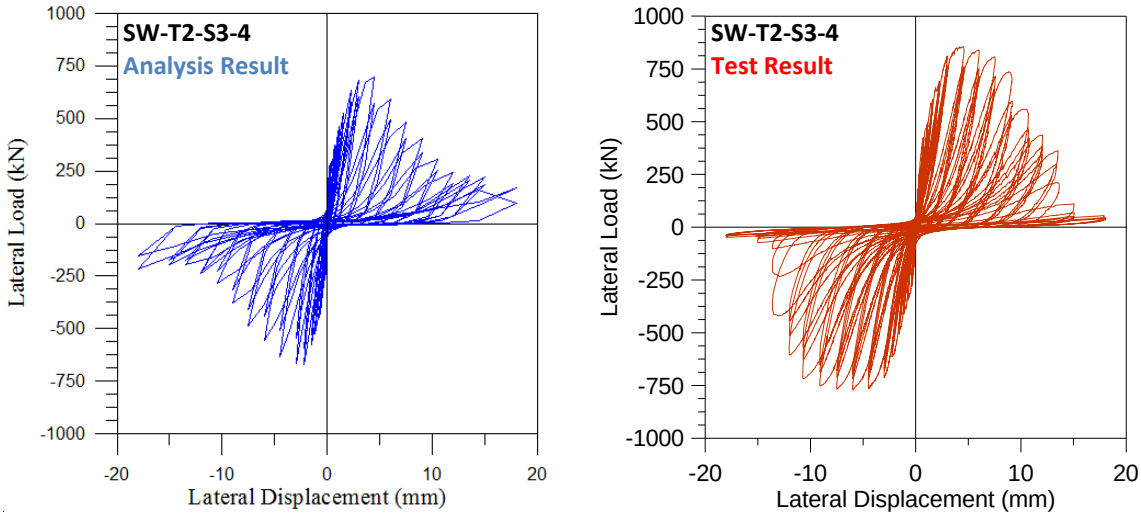

Figure 4.21. Comparison of analysis result with nonlinear dowel action vs. test result for specimen SW-T2-S3-4.

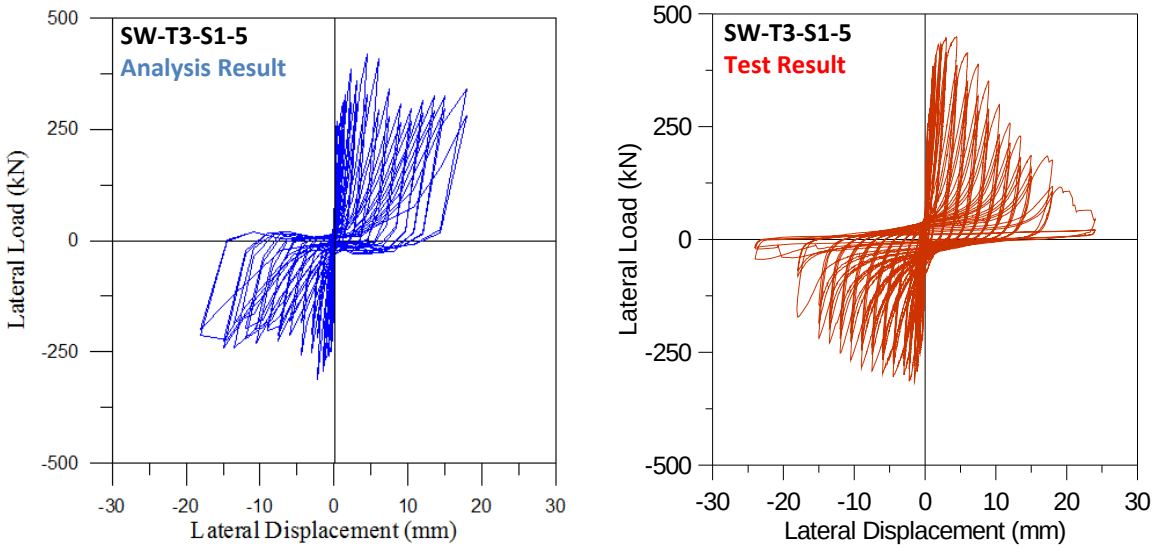

Figure 4.22. Comparison of analysis result with nonlinear dowel action vs. test result for specimen SW-T3-S1-5.

Figure 4.23 and Figure 4.24, present comparison of analysis and test results for specimens SW-T4-S1-6 and SW-T5-S1-7, respectively. The model significantly overestimates the lateral load capacity of specimen SW-T4-S1-6, while it moderately underestimates the lateral load capacity of specimen SW-T5-S1-7. Pinching characteristics are well represented for both specimens. While ductility characteristics of specimen SW-T5-S1-7 are reasonably represented in the analysis results, for specimen SW-T4-S1-6, the model predicts a more brittle response (rapid degradation in lateral load) compared to test results.

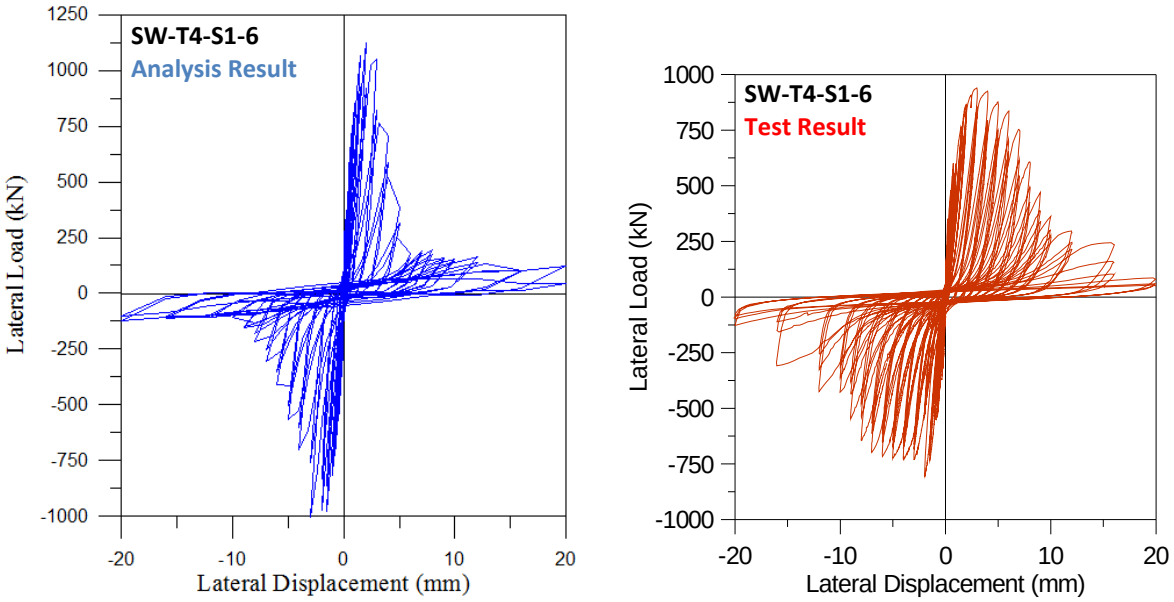

Figure 4.23. Comparison of analysis result with nonlinear dowel action vs. test result for specimen SW-T4-S1-6.

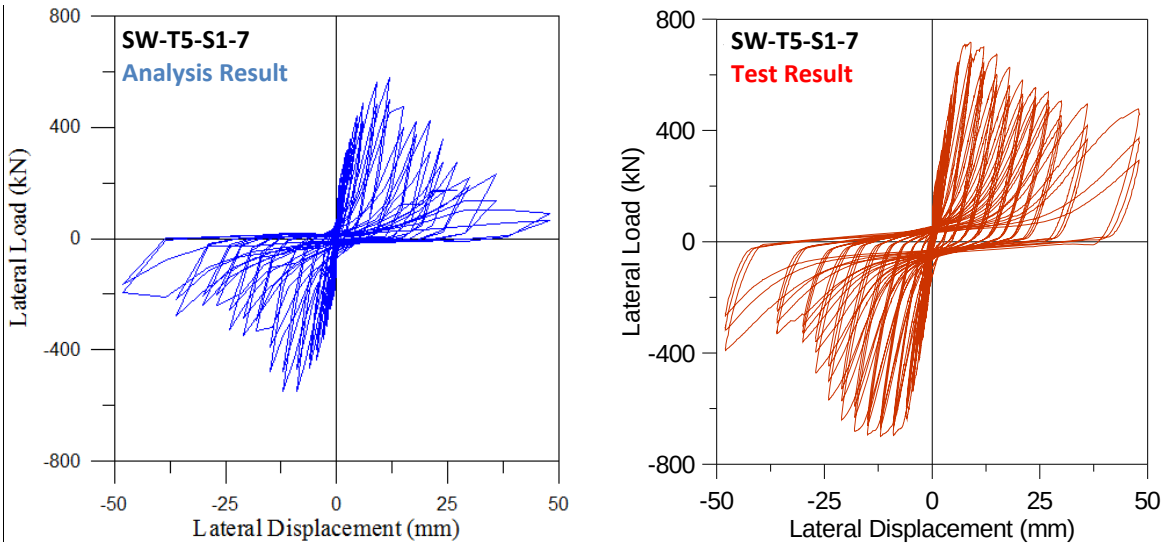

Figure 4.24. Comparison of analysis result with nonlinear dowel action vs. test result for specimen SW-T5-S1-7.

Comparison of analysis and test results for specimens SW-T6-S1-8 and SW-T1-S2-9 are presented in Figure 4.25 and Figure 4.26, respectively. The lateral load capacity of specimen SW-T6-S1-8 is underestimated by the model, whereas for specimen SW-T1-S2-

9, the model yields a reasonable lateral load capacity prediction, although a relatively brittle response is predicted by the model.

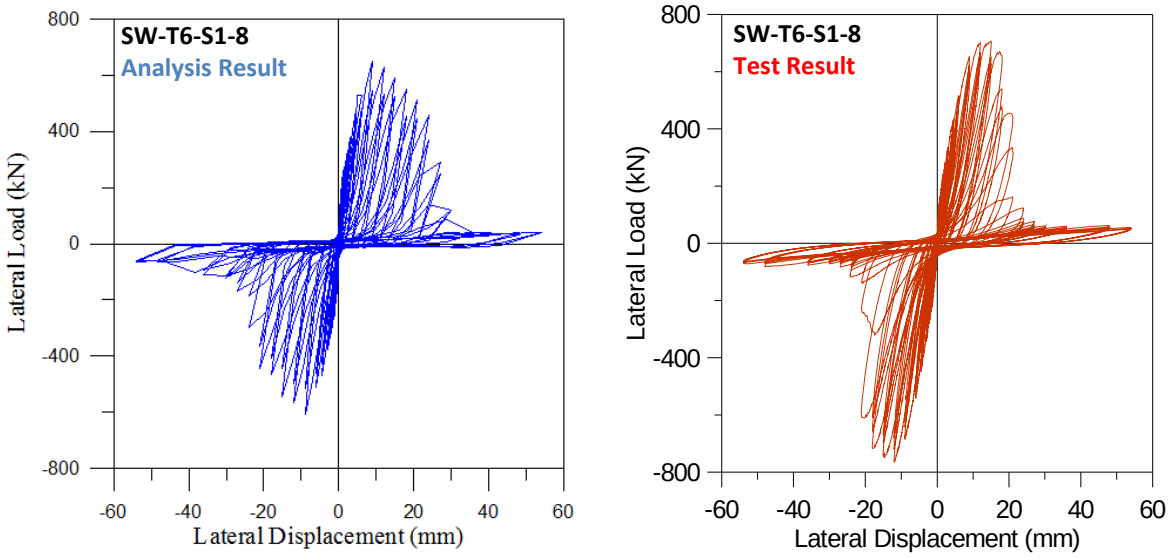

Figure 4.25. Comparison of analysis result with nonlinear dowel action vs. test result for specimen SW-T6-S1-8.

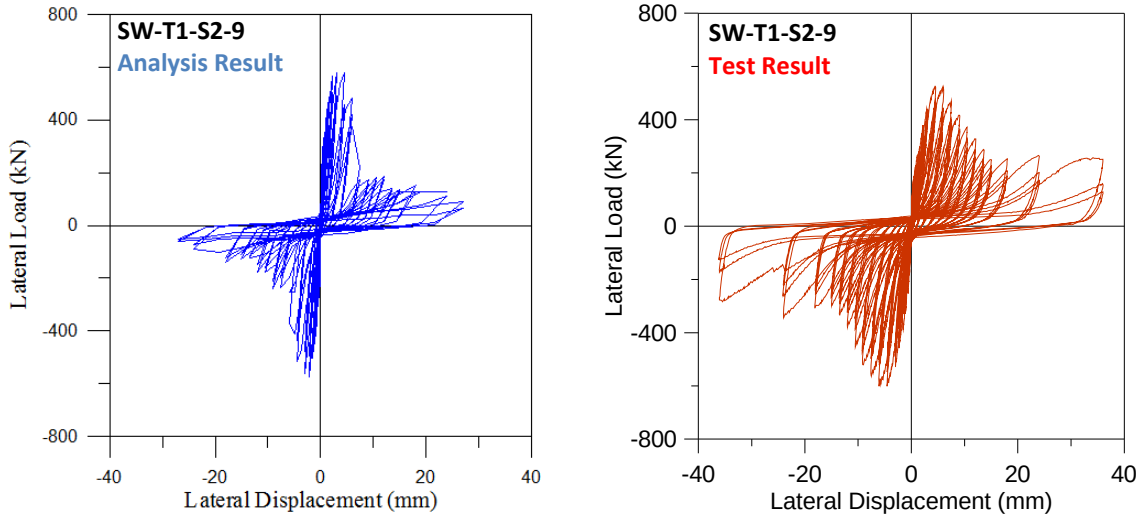

Figure 4.26. Comparison of analysis result with nonlinear dowel action vs. test result for specimen SW-T1-S2-9.

Figure 4.27 and Figure 4.28present comparison of analysis and test results obtained for specimens SW-T1-N5-S1-10 and SW-T1-N10-S1-11, respectively. Reasonably

accurate lateral load capacity predictions were predicted by the model for both specimens that were subjected to axial load during testing, which demonstrates that the model successfully represents the influence of axial load on the lateral load capacity of these walls.

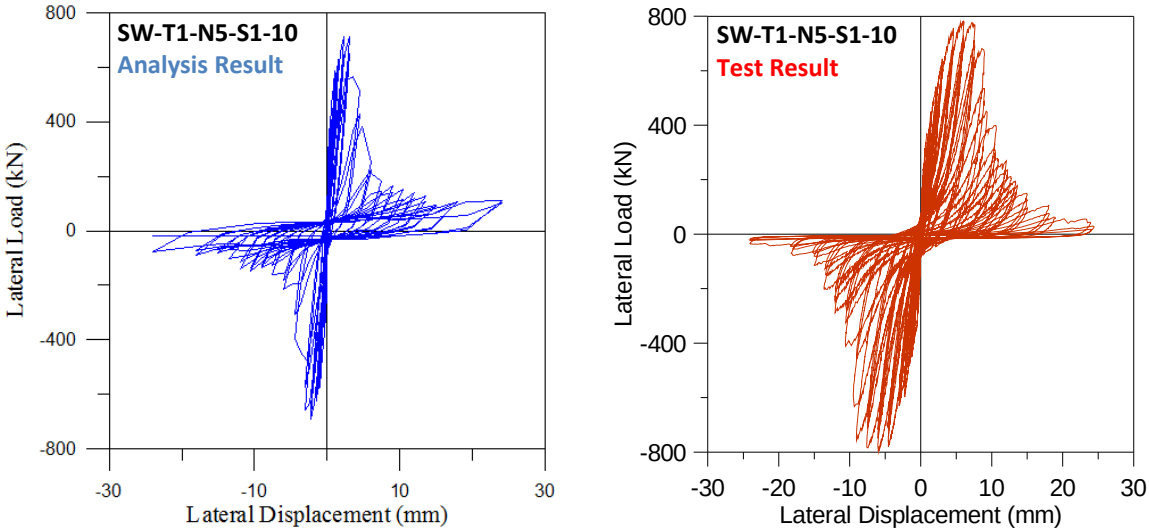

Figure 4.27. Comparison of analysis result with nonlinear dowel action vs. test result for specimen SW-T1-N5-S1-10.

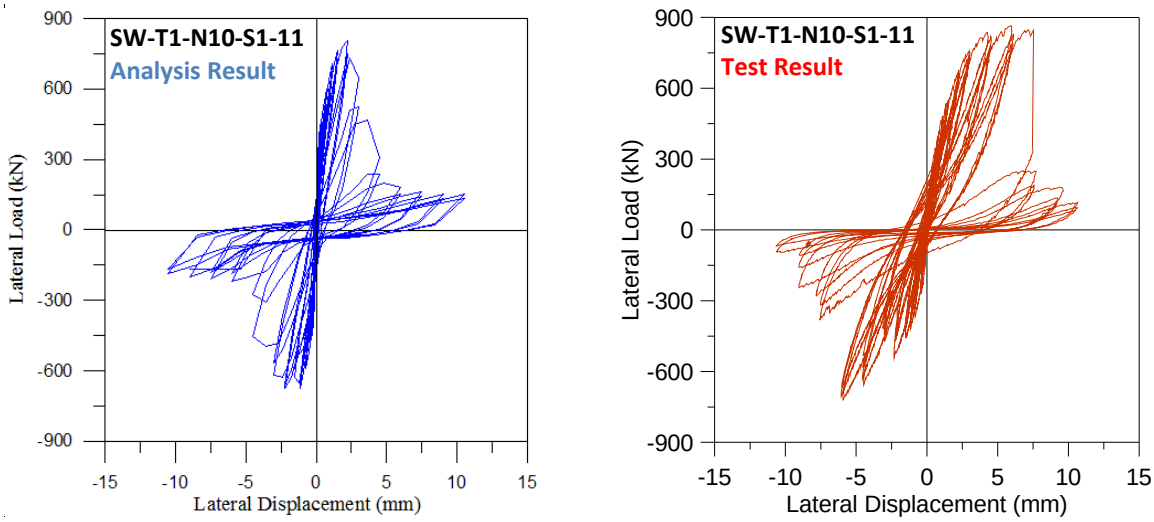

Figure 4.28. Comparison of analysis result with nonlinear dowel action vs. test result for specimen SW-T1-N10-S1-11.

5. SUMMARY AND CONCLUSIONS

5.1. Overview

In this study, a new finite element modeling methodology was implemented for simulating the in-plane hysteretic lateral load behavior of squat walls with aspect ratios not larger than 1.0, the behavior of which is governed by nonlinear shear deformations. The behavioral characteristics of the constitutive panel elements implemented in the finite element model were based on the Fixed-Strut-Angle modeling approach. Improvements were made on the constitutive panel model formulation, for better representation of the shear-aggregate-interlock effects in concrete and dowel action on reinforcing bars, constituting the shear stress transfer mechanisms across the cracks. Sensitivity studies were conducted on the influence of parameters of the constitutive shear-aggregate-interlock and dowel models on the model results. The model was extensively calibrated for eleven squat wall specimens and model predictions were compared with experimentally-measured lateral load vs. displacement responses.

5.2. Conclusions

The following conclusions can be drawn on the basis of the results obtained using the analytical modeling approach implemented in this study:

- The modeling approach implemented in this study is believed to be a significant improvement towards reliable prediction of the response of squat walls under reversed-cyclic loading conditions. Numerical stability of the model, as well as the capability of the model to effectively simulate degrading (softening) lateral load responses with pronounced pinching, makes it a feasible candidate for simulation of shear-controlled wall responses, as well as general responses under combined shear and flexural actions.

- The model was shown to provide reasonable predictions of the lateral stiffness, lateral load capacity, and ductility (lateral load degradation) characteristics of the wall specimens investigated in this study, although moderate-level discrepancies between test results and model predictions were frequently observed. It is believed that the primary reason of these discrepancies is uncertainty in calibration of the constitutive parameters incorporated in the model for shear aggregate interlock effects in concrete and dowel action on reinforcing bars.

- Implementation of the proposed nonlinear constitutive model for dowel action resulted in improved response predictions for the squat walls investigated, compared to a linear elastic modeling approach to represent the dowel action. Model predictions for lateral load values at large displacements, the shape of the unloading/reloading loops, and pinching characteristics of the response, were consistently improved for all wall specimens, demonstrating the effectiveness of the proposed constitutive dowel action model in enhancing the model accuracy.

5.3. Recommendations for Future Studies

The following recommendations can be made for future studies related with the scope of this thesis:

- Parameters of the constitutive models representing shear aggregate interlock effects in concrete and dowel action on reinforcing bars can be further calibrated via additional parametric sensitivity studies conducted on a wider range of experimental data on wall specimens with various geometries and reinforcement characteristics.

- More robust constitutive models to represent shear aggregate interlock and dowel effects can be implemented in the model formulation.

- Accuracy of the model can also be investigated at local response levels, considering deformations and average strains in concrete and reinforcing steel.

- The finite element model formulation can be improved. Improved shape functions and Gauss integration points can be implemented into the formulation, for a more refined description of the strain and stress fields acting on the model elements.

- The influence of strain localization effects (size effects) on the model response can be investigated. Methodologies can be proposed to relate the dimensions of the model elements to appropriate constitutive material parameters to consider size effects in modeling.

REFERENCES

Belarbi, A. and T. C. Hsu, 1994, "Constitutive Laws of Concrete in Tension and Reinforcing Bars Stiffened By Concrete", *ACI Structural Journal*, Vol. 91, No. 4, pp. 465-474.

Chang, G. A. and J. B. Mander, 1994, *Seismic Energy Based Fatigue Damage Analysis of Bridge Columns: Part I-Evaluation of Seismic Capacity*, NCEER Report No. 94-0006, National Center for Earthquake Engineering Research.

Clarke, M. J. and G. J. Hancock, 1990, "A Study of Incremental-Iterative Strategies for Non-Linear Analyses", *International Journal for Numerical Methods in Engineering*, Vol. 29, pp. 1365-1391.

Gérin, M. and P. Adebar, 2009, "Simple Rational Model for Reinforced Concrete Subjected to Seismic Shear", *ASCE Journal of Structural Engineering*, Vol. 135, No. 7, pp. 753-761.

Gopalaratnman, V. S. and S. P. Shah, 1985, "Softening Response of Plain Concrete under Direct Tension", *Journal of the American Concrete Institute*, Vol. 82, No. 3, pp. 310-323.

Gullu, M. F., 2013, *Finite Element Modeling Of Reinforced Concrete Structural Walls*, MS. Thesis, Boğaziçi University.

Hidalgo, P. A., C. A. Ledezma, and R. M. Jordan, 2002, "Seismic Behavior of Squat Reinforced Concrete Shear Walls", *Earthquake Spectra,* Vol. 18, pp. 287-308.

Hsu, T. C., 1988, "Softened Truss Model Theory for Shear and Torsion", *ACI Structural Journal*, Vol. 85, No. 6, pp. 624-635.

Kabeyasawa, T., 1997, "Design of RC Shear Walls in Hybrid Wall System", *Proceedings, The Fourth Joint Technical Coordinating Committee*, U.S.-Japan Cooperative Seismic Research on Composite and Hybrid Structures, Monterey.

Kabeyasawa, T., H. Shiohara, S. Otani and H. Aoyama, 1983, "Analysis of the Full-Scale Seven-Story Reinforced Concrete Test Structure", *Journal of the Faculty of Engineering*, The University of Tokyo (B), Vol. 37, No. 2, pp. 431-478.

Kolozvari, K., T. Tran, J. W. Wallace and K. Orakcal, 2012, "Modeling of Cyclic Shear-Flexure Interaction in Reinforced Concrete Structural Walls", *Proceedings, 15th World Conference on Earthquake Engineering,* Lisbon, Portugal, No. 2471.

Mander, J. B., M. J. N Priestley and R. Park, 1988, "Theoretical Stress-Strain Model for Confined Concrete", *ASCE Journal of Structural Engineering*, Vol. 114, No. 8, pp. 1804-1826.

Mansour, M. Y., T. C. Hsu and J.Y. Lee, 2002, "Pinching Effect in Hysteretic Loops of R/C Shear Elements", *ACI Special Publications*, Vol. 205, pp. 293-321.

Mansour, M. Y. and T. C. Hsu, 2005, "Behavior of Reinforced Concrete Elements under Cyclic Shear", *ASCE Journal of Structural Engineering*, Vol. 131, No. 1, pp. 44-53.

Massone, L. M., 2006, *Analytical and Experimental with Shear - Flexure Interaction in RC Walls*, Ph.D. Thesis, University of California.

Massone, L. M., and J. W. Wallace, 2009, *RC Wall Shear-Flexure Interaction: Analytical and Experimental Responses*, UCLA-SGEL-2009/2, Structural & Geotechnical Engineering Laboratory, Department of Civil & Environmental Engineering, University of California-Los Angeles, Los Angeles, CA.

Mau, S. T. and T. C. Hsu, 1986, "Shear Design and Analysis of Low-Rise Structural Walls", *ACI Structural Journal*, Vol. 83, No. 2, pp. 306-315.

Menegotto, M. and E. Pinto, 1973, "Method of Analysis for Cyclically Loaded Reinforced Concrete Plane Frames Including Changes in Geometry and Non-Elastic Behavior of Elements under Combined Normal Force and Bending", *Proceedings, IABSE Symposium on Resistance and Ultimate Deformability of Structures Acted on by Well-Defined Repeated Loads*, Lisbon, Portugal.

Orakcal, K., 2004, *Nonlinear Modeling and Analysis of Slender Reinforced Concrete Walls*, Ph.D. Thesis, University of California.

Orakcal, K., D. Ulugtekin and L. M. Massone, 2012, "Constitutive Modeling of Reinforced Concrete Panel Behavior under Cyclic Loading" *Proceedings*, *15th World Conference on Earthquake Engineering*, Lisbon, Portugal, No. 3573.

Orakcal, K., J. W. Wallace and J. P. Conte, 2004, "Flexural Modeling of Reinforced Concrete Walls – Model Attributes", *ACI Structural Journal*, Vol. 101, No. 5, pp. 688-699.

Orakcal, K. and J. W. Wallace, 2006, "Flexural Modeling of Reinforced Concrete Walls – Model Calibration", *ACI Structural Journal*, Vol. 103, No. 2, pp. 196-206.

Orakcal, K., L. M. Massone, and J. W. Wallace, 2006, *Analytical Modeling of Reinforced Concrete Walls for Predicting Flexural and Coupled - Shear - Flexural Responses*, PEER Report No. EEC-9701568, Pacific Earthquake Engineering Research, Berkeley.

Palermo, D. and F. J. Vecchio, 2003, "Compression Field Modeling of Reinforced Concrete Subjected to Reversed Loading: Formulation", *ACI Structural Journal*, Vol. 100, No. 5, pp. 616-625.

Pang, D. and T. C. Hsu, 1995, "Behavior of Reinforced Concrete Membrane Elements in Shear", *ACI Structural Journal*, Vol. 92, No. 6, pp. 665-677.

Pang, D. and T. C. Hsu, 1996, "Fixed Angle Softened Truss Model for Reinforced Concrete", *ACI Structural Journal*, Vol. 93, No. 2, pp. 197-207.

Petrangeli, M., P. E. Pinto and V. Ciampi, 1999, "Fiber Element for Cyclic Bending and Shear of RC Structures. I: Theory", *Journal of Engineering Mechanics*, ASCE, Vol. 125, No. 9, pp. 994-1001.

Saatçioğlu, M. and S. Razvi, 1992, "Strength and Ductility of Confined Concrete", *ASCE Journal of Structural Engineering*, Vol. 118, No. 6, pp. 1590-1607.

Tran, T. A. and J. W. Wallace, 2012, "Experimental Study of Nonlinear Flexural and Shear Deformations of Reinforced Concrete Structural Walls", *Proceedings*, *15th World Conference on Earthquake Engineering*, Lisbon, Portugal, No. 3913.

Terzioglu, T., 2011, *Experimental Evaluation Of The Lateral Load Behavior Of Squat Structural Walls*, MS. Thesis, Boğaziçi University.

Ulugtekin, D., 2010, *Analytical Modeling of Reinforced Concrete Panel Elements under Reversed Cyclic Loadings*, MS. Thesis, Boğaziçi University.

Vecchio, F. J. and M. P. Collins, 1986, "The Modified Compression-Field Theory for Reinforced Concrete Elements Subjected to Shear", *ACI Structural Journal*, Vol. 83, No. 2, pp. 219-231.

Vecchio, F. J. and M. P. Collins, 1993, "Compression Response of Cracked Reinforced Concrete", *ASCE Journal of Structural Engineering*, Vol. 83, No. 2, pp. 219-231.

Vulcano, A., V. V. Bertero and V. Colotti, 1988, "Analytical Modeling of RC Structural Walls", *Proceedings*, *9th World Conference on Earthquake Engineering,* Vol. 6, Tokyo-Kyoto, Japan, pp. 41-46.

Yankelevsky, D. Z. and H. W. Reinhardt, 1987, "Response of Plain Concrete to Cyclic Tension", *ACI Materials Journal*, Vol. 84, No. 5, pp. 365-373.